Theory, Design and Development of Resonance Based Biosensors in Terahertz and Millimeter-wave

by

Mohammad Neshat

A thesis
presented to the University of Waterloo
in fulfillment of the
thesis requirement for the degree of
Doctor of Philosophy
in
Electrical and Computer Engineering

Waterloo, Ontario, Canada, 2009

I hereby declare that I am the sole author of this thesis. This is a true copy of the thesis, including any required final revisions, as accepted by my examiners.

I understand that my thesis may be made electronically available to the public.

Abstract

Recent advances in molecular biology and nanotechnology have enabled scientists to study biological systems at molecular and atomic scales. This level of sophistication demands for new technologies to emerge for providing the necessary sensing tools and equipment. Recent studies have shown that terahertz technology can provide revolutionary sensing techniques for organic and non-organic materials with unprecedented accuracy and sensitivity. This is due to the fact that most of the macromolecules have vibrational and/or rotational resonance signatures in terahertz range. To further increase the sensitivity, terahertz radiation is generated and interacted with the bio-sample on a miniaturized test site or the so-called biochip. From the view point of generation and manipulation of terahertz radiation, the biochip is designed based on the same rules as in high frequency electronic chips or integrated circuits (IC). By increasing the frequency toward terahertz range, the conventional IC design methodologies and analysis tools fail to perform accurately. Therefore, development of new design methodologies and analysis tools is of paramount importance for future terahertz integrated circuits (TIC) in general and terahertz biochips in particular.

In this thesis, several advancements are made in design methodology, analysis tool and architecture of terahertz and millimeter-wave integrated circuits when used as a biochip. A global and geometry independent approach for design and analysis of the travelling-wave terahertz photomixer sources, as the core component in a TIC, is discussed in details. Three solvers based on photonic, semiconductor and electromagnetic theories are developed and combined as a unified analysis tool.

Using the developed terahertz photomixer source, a resonance-based biochip structure is proposed, and its operation principle, based on resonance perturbation method, is explained. A planar metallic resonator acting as a sample holder and transducer is designed, and its performance in terms of sensitivity and selectivity is studied through simulations. The concept of surface impedance for electromagnetic modeling of DNA self-assembled monolayer on a metal surface is proposed, and its effectiveness is discussed based on the available data in the literature.

To overcome the loss challenge, Whispering Gallery Mode (WGM) dielectric resonators with high Q factor are studied as an alternative for metallic resonator. The metallic loss becomes very high at terahertz frequencies, and as a result of that planar metallic resonators do not exhibit high Q factor. Reduced Q factor results in a low sensitivity for any sensor using such resonators. Theoretical models for axially and radially layered dielectric resonators acting on WGM are presented,

and the analytical results are compared with the measured data. Excitation of WGM through dielectric waveguide is proposed, and the critical coupling condition is explained through analytical formulation. The possibility of selecting one resonance among many for sensing application is also studied both theoretically and experimentally.

A high sensitivity sensor based on WGM resonance in mm-wave and terahertz is proposed, and its sensitivity is studied in details. The performance of the proposed sensor is tested for sensing drug tablets and also liquid droplets through various measurements in mm-wave range. The comprehensive sensitivity analysis shows the ability of the proposed sensor to detect small changes in the order of 10^{-4} in the sample dielectric constant. The results of various experiments carried out on drug tablets are reported to demonstrate the potential multifunctional capabilities of the sensor in moisture sensing, counterfeit drug detection, and contamination screening. The measurement and simulation results obtained in mm-wave hold promise for WGM to be used for sensing biological solutions in terahertz range with very high sensitivity.

Acknowledgements

I would like to express my deepest gratitude to Professor Safieddin Safavi-Naeini for his supervision and support during my Ph.D. program. During the course of this research, he supported me in many ways and provided me with great opportunities.

I am thankful to my Examining Committee members, Dr. Michael Nagel from Institute of Semiconductor Electronics, RWTH Aachen University, Germany, Dr. Mungo Marsden from Department of Biology, University of Waterloo, Dr. Sujeet Chaudhuri from Department of Electrical and Computer Engineering, University of Waterloo, and Dr. Omar Ramahi from Department of Electrical and Computer Engineering, University of Waterloo, for reviewing my thesis and giving their invaluable comments and suggestions.

My special thanks to Dr. Daryoosh Saeedkia who encouraged me to start my research in this area and supported me along the way by all means. I am grateful to Dr. Suren Gigoyan whose collaboration provided me with the opportunity of learning new technical skills and novel ideas.

It was my privilege to be part of an active and friendly research group, *Microwave and Terahertz Photonics Integrated System Lab (MISL)*, at the University of Waterloo. Thanks to all of my friends for their technical help and wonderful friendship.

I wish to express my love to my family; my wonderful wife, my cute son, and my kind parents.

Dedication

To my *parents* who devoted their lives to my success, and

to my darling wife, *Leila*, and

to all *those* who opened the doors of knowledge to me.

Contents

List of Tables

List of Figures

Chapter 1

Introduction

1.1 Motivation

Terahertz gap is part of electromagnetic spectrum laying between microwave and infrared which spans roughly from 300 GHz to 10 THz. In recent years, THz spectrum has been recognized for its new applications in science and technology. Biosensing [1]–[6], biomedical imaging [7], pharmaceutical screening [8]–[9], security [10]–[13], high-speed wireless communication [14]–[18], and astronomy [19]–[20] are just a few applications to name.

Terahertz spectrum is attractive for biomolecular sensing, since many macromolecules such as protein or DNA have vibrational modes in this part of the electromagnetic spectrum [21]. This characteristic enables THz probing techniques to fingerprint biological and chemical agents.

Terahertz radiation is most suitable for imaging and detection applications, since transmission and reflection of terahertz radiation are much more sensitive to the materials it passes through compared to the microwave or infrared radiation, and also the photon energy is not harmful to live cells as in X-ray radiation. For example, in terahertz biomedical imaging, different tissues such as fat, muscle, and their content ratio can be clearly distinguished in a terahertz image as each kind of tissue has its own attenuation coefficient in terahertz range [7].

One interesting aspect of terahertz radiation is that it can pass through many materials such as paper, cardboard, plastic, wood and textile. This capability allows for non-destructive and non-invasive inspection of, e.g. mails and packages in post offices, luggages and persons at airports and security checkpoints and border crossings.

In many communication applications, very high speed data transfer is desirable. To achieve this goal, high frequency THz carrier can be used [14] in short-range wireless communication. However, long range wireless connections may not be feasible in THz frequencies because of the high atmospheric loss.

The richness of terahertz radiation properties has become a strong driver for advancement of THz technology in the last few years, and resulted in a great progress in shrinking the THz gap. However, more research and efforts are needed toward closing the gap entirely.

In this research, the focus is on the design and development of novel integrated circuits and devices working within the terahertz and mm-wave range with the emphasis on chemical and biological sensing applications. Conventionally, the integrated circuits were designed based on circuit theory with the assumption of lumped elements. However, by increasing the frequency toward mm-wave and particularly terahertz range, the conventional approaches certainly can not provide accurate prediction of the circuit performance as the chip dimensions become comparable and likely larger than the wavelength. Based on this fact, in this research, special attention has been paid to applying a global and comprehensive approach for modeling and analysis of distributed THz photomixer sources as the core component in a terahertz integrated circuit (TIC). Using this kind of THz source, a biochip based on planar resonator is proposed and its performance in terms of sensitivity and selectivity is investigated in details. As an alternative to planar resonators, whispering gallery mode dielectric resonators are explored theoretically and experimentally to establish a very high sensitivity sensing platform in millimetre-wave and terahertz range.

1.2 Thesis Overview

Chapter 2 reviews the state-of-the-art sensing techniques in terahertz and millimeter-wave range. Most widely used techniques such as free-space terahertz spectroscopy, waveguide- and resonance-based methods are compared.

Design and analysis of a travelling-wave THz photomixer source, as the core component in a TIC, is discussed in details in Chapter 3. Three solvers based on photonic, semiconductor and electromagnetic theories are developed and combined as a unified analysis tool.

Using the developed THz photomixer source, a resonance-based biochip structure is proposed in Chapter 4 and its operation principle is explained. A planar

metallic resonator acting as a sample holder and transducer is designed, and its performance in terms of sensitivity and selectivity is studied through simulations. The concept of surface impedance for modeling DNA monolayers is proposed and its effectiveness is discussed based on the available data in the literature.

The main disadvantage of planar metallic resonators is that they are lossy at THz range and therefore can not provide high Q factor. This results in a low sensitivity for any sensor using such resonators. As an alternative, Whispering Gallery Mode (WGM) resonators with high Q factor are explored in Chapter 5. Theoretical modeling for axially and radially layered dielectric resonators (DRs) acting on WGM are presented and the analytical results are compared with the measurement. Excitation of WGM through dielectric waveguide is proposed and the critical coupling condition are explained through analytical formulation. The possibility of selecting one resonance among many for sensing application is also studied both theoretically and experimentally.

In Chapter 6, a high sensitivity sensor based on WGM resonance in mm-wave and THz is proposed and its sensitivity are studied in details. The performance of the proposed sensor is examined for sensing drug tablets and also liquid droplets through various measurements in mm-wave range. A comprehensive sensitivity analysis is performed to show that a change in the order of 10^{-4} in the sample dielectric constant can be detected by the proposed sensor. The results of various experiments carried out on drug tablets are reported to demonstrate the potential multifunctional capabilities of the sensor in moisture sensing, counterfeit drug detection, and contamination screening.

Chapter 7 summarizes the findings of this thesis, and gives directions for possible future works.

Chapter 2

Terahertz and Millimeter-Wave Sensing: A Technology Overview

2.1 Introduction

Recent advances in molecular biology and nanotechnology have enabled scientists to study biological systems at molecular and atomic scales. This level of sophistication demands for new technologies to emerge for providing the necessary tools and equipment. Biosensors are among those tools which play a crucial role in this advancement. A biosensor is a tool for detection of a biological analyte (e.g. protein, nucleic acid, polypeptide, glucose) in a sample collection. The operating principle of most biosensors is based on the interaction of the analyte with a transducer. This interaction results in a measurable quantity from which the information of interest is obtained through some data analysis. Depending on the type of the interaction, different kinds of biosensors are introduced such as optical [22] and electro-chemical sensors [23].

In recent years, the physics and fundamentals of the interaction of THz radiation at molecular level have been widely studied for sensing and characterizing chemical and biological agents. For example, highly resolved and reproducible spectra of DNA macromolecules (and other biological materials) have been recently measured in the spectral range from 10cm^{-1} to 500cm^{-1} where reliable data was previously not available [24]. Moreover, various theoretical and experimental attempts have been made to establish THz-frequency sensing as a new characterization tool for chemical, biological and semiconductor materials by introducing novel device concepts within the THz gap. Sensing the complex dielectric properties of a sample

in the terahertz frequency range is performed either by detecting the resonant absorption of molecular or phonon resonances (spectroscopy), or by monitoring the dielectric changes associated with the binding of biomolecules (on-chip sensing).

In this Chapter, we will review the state-of-the-art technology in mm-wave and terahertz frequency sensing and spectroscopy.

2.2 Free-Space THz Spectroscopy

The basic principle of a Terahertz Time-Domain Spectroscopy (THz-TDS) system can be explained as follow; it starts with a femtosecond laser producing an optical-pulse train. Each pulse is split into two paths. One part, called pump, reaches the THz emitter, e.g. a photoconductive antenna or a nonlinear crystal, where the optical pulses are transformed into (sub)picosecond electromagnetic (or THz) pulses. Generated THz pulses then propagate in free space, and are focused onto an ultrafast detector, e.g. a low-temperature-grown GaAs photoconductive switch or an electro-optic crystal. The other part of the optical pulse, called probe, reaches the detector after passing through a time-delay stage. The detector measures the electric-field amplitude of the THz pulses.

In transmission spectroscopy, a specimen is placed in the path of the THz beam propagating from the emitter to the detector in free-space, and the change in the waveform is measured. Generally, the amplitude decreases and the waveform is delayed in the time domain. The complex refractive index of the specimen material can be estimated by comparison of the waveforms with and without the sample.

Since the early 1990s, THz-TDS has been applied to many materials such as biomolecules [21, 25], medicines [8], and tissues [26]. It has been found that terahertz spectroscopy has a unique ability to observe intermolecular vibrations [27] compared to the conventional infrared spectroscopy which is able to detect the intramolecular modes. This new additional tool for intermolecular vibration studies is expected to elucidate the dynamics of large biomolecules.

Several studies have been conducted on the application of terahertz pulse spectroscopy and imaging of skin tissue and related cancers [28]. Since the absorption of terahertz radiation is sensitive to polar molecules, e.g. water, it is possible to differentiate between diseased and normal tissues from their different levels of hydration. As the THz transmittance of ice is much higher than that of water, cancer cells can also be detected in frozen tissues.

Terahertz time-domain reflection spectroscopy is one of the methods with the most potential for investigating the characteristic vibrational mode in biomolecules. In the case of a liquid solution, however, it is difficult to extract information on a solute molecule from the reflection data of the solution because of the extremely short interaction length. To overcome this hurdle, THz Time-Domain Attenuated Total Reflection (TD-ATR) spectroscopy has been proposed [29]. A prism is inserted into the THz beam, which produces evanescent travelling waves on the prism surface. The change in the reflection and phase due to the interaction between the evanescent wave and the sample placed near the prism surface are evaluated by comparing the TDS signals with and without samples.

Although free-space THz sensing and spectroscopy techniques promise to become standard in the study of large molecule dynamics in future, it does not seem to be suitable for applications requiring high sensitivity.

2.3 Integrated THz Biosensors

In comparison with free-space schemes, integrated biochips provide a drastically enhanced sensitivity enabling analysis down to femtomol levels [30]. Beside high sensitivity, integrated biochips have many other advantages including faster analysis and response time, better process control due to the faster response time of the system, compactness of the system, high-throughput analysis, lower fabrication costs due to mass production, and safer platform for chemical, radioactive or biological studies because of less required sample volume.

2.3.1 Waveguide-based sensing

In waveguide-based sensing, the sample is delivered to a waveguide structure. The presence of the sample modifies the amplitude and phase of the propagating wave inside the waveguide. The amount of change in the waveform depends on the interaction length as well as the sample properties. Conventionally in microwave range, broadband measurements of complex permittivity and permeability have been performed based on the transmission/reflection (TR) method [31, 32]. In TR method, the sample is placed in a section of a waveguide or transmission line and the two-port complex scattering parameters are measured preferably by a vectorial network analyzer (VNA). A system of equations, which analytically describes the structure under measurement, relates the measured scattering parameters to the complex

permittivity and permeability of the material. The equations contain the complex permittivity and permeability, the calibration reference plane positions, and the sample length as unknowns. Since the system of equations is generally overdetermined, it can be solved in various ways which has been extensively discussed in the literature. For example, from accuracy viewpoint, the equations should be stable over the frequency range of interest, and preferably do not depend on the position of the calibration reference plane and the sample dimensions.

In recent years, those conventional sensing and characterization methods, developed for microwave region, are revisited to be used in mm-wave and terahertz frequencies. For example, a microstrip line based sensing chip for characterization of polar liquids in terahertz regime has been proposed by Ohkubo et al. [33]. In this chip, terahertz waves are generated and detected with femtosecond optical pulses. The spectroscopic sensitivity can be adjusted by changing the thickness of a polyimide layer covering the strip. The liquid under test is then deposited on top of the polyimide layer, and is laterally confined in a polyethylene vessel with an inner diameter of 6 mm.

The evanescent wave from total internal reflection off a silicon prism has been used to couple pulsed THz radiation frequency selectively into a waveguide [34]. The coupled frequencies were determined via time domain spectroscopy and react sensitively to any changes of thickness or phase shift upon reflection. As reported, the sensitivity to phase shifts makes this waveguide sensor attractive for the detection of very thin adsorbates.

The propagation of terahertz waves in two-dimensional photonic-crystal waveguides has been numerically studied [35] to investigate the effects of introducing small quantities of molecules, such as DNA, into selected air holes for sensor applications. Comparison with bulk systems has shown that photonic-crystal waveguides are promising for biochemical sensing.

A dielectric measurement method based on dielectric image guide (DIG) has been presented [36] in mm-wave range. In this method, the sample droplet is placed on top surface of a dielectric waveguide by a pipette. Once dispensed, the droplet spreads out on the surface to fill the width of the waveguide in a certain length, and form a thin dielectric layer on top of the waveguide. Because of the liquid surface tension, the volume of the droplet can be optimized such that the liquid does not overflow the side walls of the waveguide. This method is ideal for characterization of very small liquid samples, e.g. in the range of 1μl or less, and has the advantage of broadband frequency measurement.

2.3.2 Resonance-based sensing

In resonance-based sensing, the resonant perturbation method [37] is mainly employed. This method has been used for sensing a wide range of physical or chemical properties, e.g. moisture content of wheat grains [38], or chemical binding states of DNA molecules [39]. In this method, a small sized sample is placed on critical points inside, on, or close to a resonator. The sample perturbs the resonance mode, and causes a change in the resonance frequency and/or Q factor. Variation in the resonance characteristics, if calibrated properly, can be used to quantify the property of interest. Resonance-based sensors have the highest sensitivity, but are limited in frequency response bandwidth. Several approaches in terahertz and mm-wave range have been demonstrated in resonance-based sensing, e.g. using planar resonators, Bragg reflection cavities, evanescent field resonances, surface plasmon resonances, and whispering gallery mode resonances.

Passive THz filters based on planar waveguide have been used as sample carriers and transducers for THz transmission analysis [30, 40] where the detection of single base mutations on DNA molecules have been demonstrated.

Lithographically made 1-D symmetric and asymmetric dielectric gratings on metallized high conductivity Si chips have been incorporated within metal parallel plate waveguides to form Bragg waveguides [41]. These waveguides have Bragg resonances with line widths approaching 6 GHz and Q factor as high as 430 which make them excellent structures for THz sensing applications.

The potential use of frequency selective surface made from asymmetric split ring resonators has been numerically studied and the structure has been optimized [42]. Due to interference effects a resonance occurs with a steep flank in the frequency response which is shifted upon dielectric loading. Utilizing a strong E-field concentration, by selective loading, the detection of very small amounts of probe material has been predicted.

A periodic array of metallic columns on a metallic substrate, which constitute a plasmonic metamaterial structure, has been proposed [43]. It has been shown that such structure can support plasmonic surface waves at THz frequencies. Numerical analysis supports that highly sensitive THz sensors can be realized using this structure.

Whispering Gallery Mode (WGM) resonance is among the most sensitive and accurate schemes proposed to date for sensing and dielectric characterization [44]. Krupka et al. have used whispering-gallery and TE modes for broadband charac-

terization of bulk GaAs and GaP samples from 30 to 300K temperature range [45]. They could reach better than 0.2% of total relative measurement uncertainty for real part of permittivity. Annino et al. have measured the complex permittivity of alumina (Al_2O_3) as a solid sample and cyclohexane as a liquid sample in the frequency range of $18 - 26$ GHz by means of whispering gallery dielectric resonators [46]. They applied mode matching method approximation to calculate field distribution in different resonant modes. In their sensitivity measurements, they could detect a minimum variation of ϵ'' equal to 0.00013, which corresponds to a minimum detectable variation of 6.5×10^{-5} in $\tan\delta$. Measured dielectric parameters of some plastic and ceramic materials over the range of 50-110 GHz frequencies are presented in [47] using WGM with large azimuthal mode numbers.

In the optical range, WGM resonance method has been also well recognized for sensing applications. Arnold et al. have presented an approach for specific and rapid unlabeled detection of a virus by using a microsphere-based whispering gallery mode sensor that transduces the interaction of a whole virus with an anchored antibody [48]. They have shown theoretically that this sensor can detect a single virion below the mass of HIV. Yang and Guo have proposed an active optical sensor based on a microcavity with gain [49]. They have shown that an active sensor using a gain-doped microsphere can provide 10^4-fold narrower resonance line width than does a passive microcavity in the transmission spectrum. Their analysis shows that this type of compact active microcavity is sensitive to an effective refractive index change of the order of 10^{-9}. Boyd and Heebner have described a photonic device based on a high-finesse, whispering-gallery-mode disk resonator that can be used for the detection of biological pathogens [50]. Their formulation predicts that, under optimum conditions, as few as 100 molecules can be detected.

Despite a good progress which has been achieved in theoretical study and experimental demonstration of resonance-based sensing approaches, more efforts are still to be made for using these techniques in emerging applications, and also pushing the experimental performance to the theoretical limits by proposing low-cost engineering solutions.

Chapter 3

Analysis of Traveling-Wave Terahertz Photomixers

3.1 Introduction

In recent years, various applications of terahertz technology have become feasible due to the advancement of terahertz generation and detection techniques. Among different terahertz generation techniques, photoconductive sources have shown great promise as they are potentially compact, low power-consuming, coherent, widely tunable, and cost-effective with room temperature operation [51, 52].

Photomixing is a heterodyne scheme in which the outputs of two single-mode lasers or the output modes of a dual-mode laser, with the frequency difference falling in the terahertz range, mix in a nonlinear medium such as photoconductor or superconductor [53, 54]. High performance photomixer design requires the combination of both microwave and photonic techniques.

In conventional small area photomixer structures [55], laser beams illuminate the photoconductor at a small gap between feeding points of an antenna, whereas in a traveling-wave photomixer [56], the laser beams interact with the photoconductor in a relatively large area. In fact, in a traveling-wave photomixer, a microwave waveguide or transmission line is combined with an optical waveguide on the same multi-layer guiding structure. A traveling-wave photocurrent is generated inside the semiconductor due to the laser-photoconductor interaction, and acts as an impressed source for terahertz radiation [57]. When a transmission line such as a coplanar stripline (CPS), or a coplanar waveguide (CPW) is integrated with the photomixer structure, the terahertz wave is coupled into the transmission line as

a guided wave. Therefore, the propagation characteristics of the two waveguides, as well as carrier dynamics in the photoabsorbing region, determine the overall behaviour of the device.

The advantage of traveling-wave scheme is that even for relatively high-power lasers, the power density inside the semiconductor remains bellow the thermal damage threshold resulting in the increased terahertz power. One study shows that in conventional GaAs photomixers the optical power of 60 mW can cause a temperature difference of around 110 K within 10 μm of the surface of the active region [58]. This severe thermal gradient causes the material to fracture and fail. As the next advantage, in a distributed scheme, the RC frequency roll-off, associated with lumped element gap capacitance and the load resistance, is avoided.

Fig. 3.1 shows the schematic of two configurations for a traveling-wave terahertz photomixer integrated with a coplanar strip transmission line. The CPS consists of two metal strips with the width of w and separation distance of s. The total dielectric thickness is d. At THz frequencies, the coplanar structures have attracted the most attention due to their electrical characteristics and integration capability with planar devices along with fabrication compatibility with modern integration technology [59, 60].

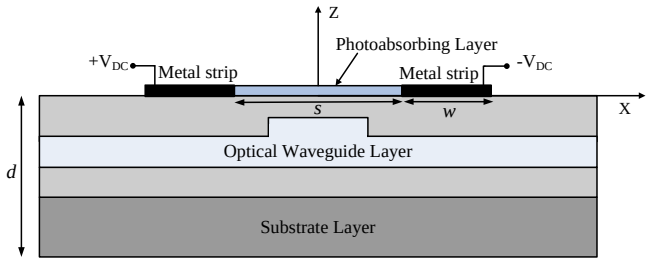

(a)

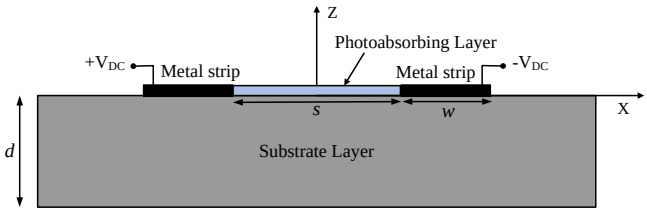

(b)

Figure 3.1: Cross section of (a) an edge-coupled (b) a vertically coupled traveling-wave photomixer integrated with a coplanar stripline.

In the edge-coupled configuration shown in Fig. 3.1(a), two frequency detuned

laser beams are gradually absorbed inside an ultra-fast photoabsorbing layer while propagating along the optical waveguide. Due to the photocarrier generation, upon applying a DC bias field, a traveling wave current with the beat frequency of two lasers flow inside the photoabsorbing layer. The traveling-wave photocurrent acts as an impressed source for terahertz radiation [57]. The terahertz radiation, then, is coupled into the CPS as guided wave.

In the vertically coupled configuration shown in Fig. 3.1(b), same phenomenon happens except that in this case the two laser beams are coupled from the free space into the photoabsorbing layer. In both configurations, the generated photocurrent acts as a source for exciting CPS modes.

Modeling of traveling-wave THz photomixer sources demands a global approach. Rigorous analysis of such sources is a multi-facet problem encompassing three fields of photonics, semiconductor physics and electromagnetics. As illustrated in Fig. 3.2, the interconnected physical processes require one to address each topic on more than an individual basis.

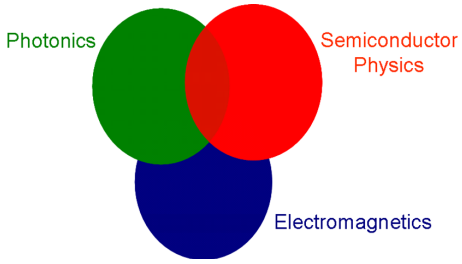

Figure 3.2: Photoconductive THz device modeling is a multi-facet problem.

Thus far, most of the works that have been reported on modeling of photoconductive THz devices deal in detail with one part of the problem while making simplistic assumptions about other aspects of the problem. For example, some researches focus on the details of the electromagnetic part, while using simple models of materials and photo-induced charge carrier transport [61]. Or, some others concentrate on the details of the materials and charge transport, but apply simple models of the electromagnetic fields inside the system, and use equivalent circuits to represent the external system [62].

Our attempt in this Chapter is to incorporate all important physical phenomena which contribute in the operation of a traveling-wave THz photomixer to raise the analytical accuracy, and yet keep the complexity at a reasonable level. Fig. 3.3 shows the combination of various solvers and their relative connections which we have developed for analysis of a THz photoconductive device.

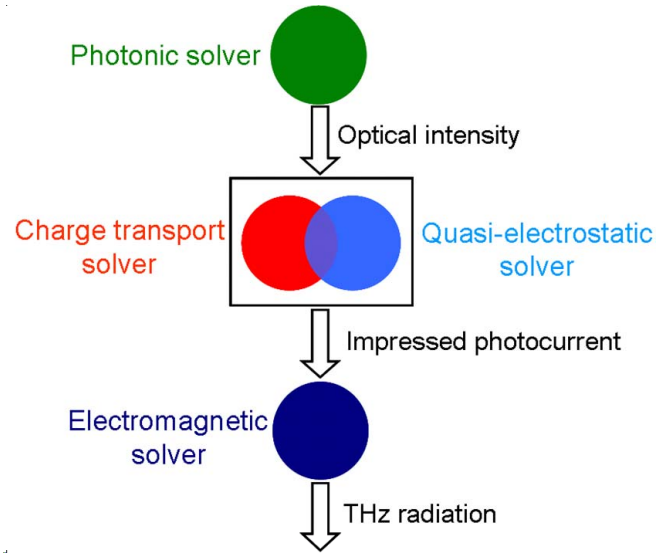

Figure 3.3: Combining various solvers for analysis of THz photoconductive devices.

In Fig. 3.3, photonic solver is basically an optical mode solver which provides the optical intensity distribution across the optical waveguide as its output. The semiconductor solver takes the optical intensity as the excitation, and solves the coupled partial differential equations governing the charge transport inside the photoconductor. As the output, the semiconductor solver calculates the photocurrent distribution inside the photoconductor. Finally, the electromagnetic solver is used to find the coupled and radiated THz signal generated from the previously calculated photocurrent. Our goal in developing these three solvers is to make a balance between the accuracy and the complexity of the techniques and models. In subsequent sections, the theory behind each solver are discussed in detail.

3.2 Optical Waveguide Design and Analysis

In this Section, an optical waveguide structure for traveling-wave photomixer is proposed and its design considerations are discussed. The optical waveguide structure being presented here is inspired from a multilayer dielectric slab waveguide previously proposed in [63] for traveling-wave terahertz photomixers. Fig. 3.4 shows the cross section of the proposed six-layer ridge waveguide structure with refractive indices which satisfy inequality relation $n_{ab} > n_{co} > n_{cl}$. Layer I is made of an ultrafast photoabsorbing material such as low-temperature-grown (LTG) GaAs. LTG-GaAs has been widely used in terahertz photomixers working at optical wave-

lengths around 800 nm. To use LTG-GaAs as the fast photoabsorber, $Al_xGa_{1-x}As$ is the compatible material for other layers which are epitaxially grown over semi-insulating GaAs substrate. By selecting an appropriate range for aluminium mole fraction x in $Al_xGa_{1-x}As$ layers, the absorption of the optical pump signal is prevented in all layers except the LTG-GaAs layer. Moreover, the aluminium mole fraction are chosen so that there exists a desired refraction contrast between low index cladding layers and the higher index core layer.

Choosing $x = 0.2$ and 0.35 for core and cladding, respectively, an $Al_{0.35}Ga_{0.65}As$ layer with the refractive index $n_{cl} = 3.44$ [64] is grown as region IV (see Fig. 3.4(a)) over a semi-insulating GaAs substrate followed by an $Al_{0.2}Ga_{0.8}As$ layer with the refractive index $n_{co} = 3.554$ as region III, followed by another $Al_{0.35}Ga_{0.65}As$ layer as region II, and finally the LTG GaAs layer with the refractive index $n_{ab} = 3.66$ as region I. The energy band-gap for $Al_xGa_{1-x}As$ is Eg =1.42 eV, 1.66 eV, and 1.86 eV, for x =0, x =0.2, and x =0.35, respectively [65]. Hence, applying lasers with wavelength around 780 nm results in photon energy E=1.59 eV, and the optical power absorption takes place only inside the LTG-GaAs layer.

The optical mode in Fig. 3.4(a) is laterally unbounded which is not efficient when a terahertz waveguide with transversely confined modal field such as coplanar stripline or coplanar waveguide is incorporated into the photomixer structure. One way to circumvent this problem is to pattern the photoabsorber layer using etching techniques as shown in Fig. 3.4(b), however, since this layer should be very thin [63], a sufficient etch depth for the required lateral confinement may not be achieved. Growing another layer of $Al_{0.35}Ga_{0.65}As$ on top of the photoabsorber can provide sufficient etch depth as shown in Fig. 3.4(c).

Considering the structure in Fig. 3.4(c), the design parameters are the thickness of the lower cladding, h_4, the core, h_3, the upper cladding, h_2, the photoabsorber layer, h_1, and the ridge, h_0, and also the ridge width, w_r, and the etch depth, h_{etch}. Effective index method (EIM) is used to find an initial value for these parameters, and then, the design is fine-tuned using semi-vectorial beam propagation method (BPM).

A few design parameters can be initialized to reduce the degrees of freedom in the design space. For example, to prevent interaction of the optical mode with the semi-insulating substrate, the lower cladding layer with the thickness of h_4 must be sufficiently thick. In practice, a cladding layer with the thickness of $h_4 = 2 - 3$ μm effectively isolates the mode from the substrate. However, for modeling purpose, the lower cladding layer is assumed to be infinitely thick. Also the LTG-

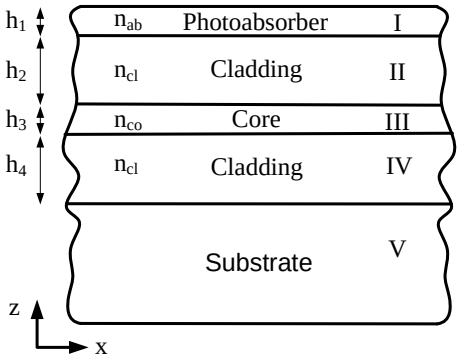

(a)

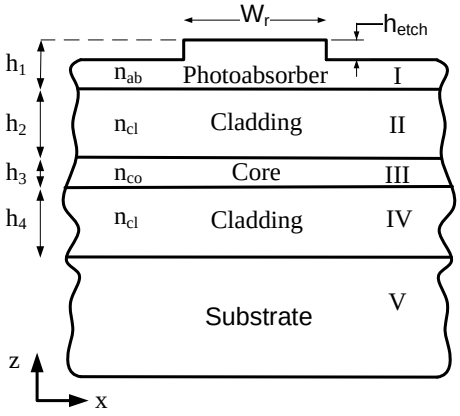

(b)

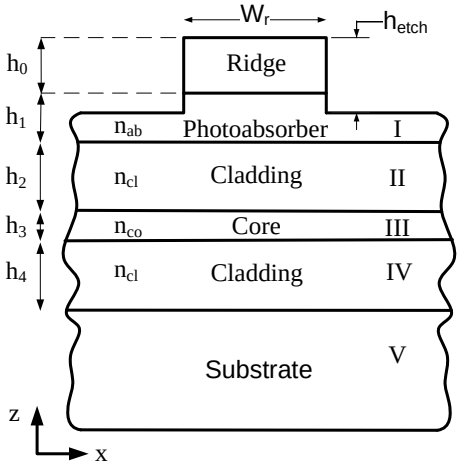

(c)

Figure 3.4: Cross section of optical waveguides showing the design evolution (a) a multilayer slab structure proposed in [63] (b) etching the photoabsorber layer for lateral confinement (c) adding a ridge to increase the lateral confinement.

GaAs photoabsorber layer should be thin ($h_1 \approx 0.1$ μm). This is due to the fact that thin layers reduce the photoabsorber fill factor, and consequently the optical power inside the photoabsorber layer remains bellow the thermal damage threshold. Moreover, the responsivity per unit length of LTG-GaAs photomixers is larger for thin photoabsorber layer as the carrier collection effectively decreases with depth [62].

Single-mode condition sets an upper limit on the core thickness, h_3. Requiring the mode to be well confined, e.g. 65% of the power confined in the core layer, defines the lower limit on h_3. The upper cladding thickness, h_2, controls the field coupling to the LTG-GaAs, and is selected to give the desired photoabsorber fill factor. Field distribution across the optical waveguide and consequently the photoabsorber fill factor can be found through EIM. In effective index method a two-dimensional waveguide is treated as the combination of two orthogonal one-dimensional waveguides [66]. As shown in Fig. 3.5, to solve the two-dimensional problem, the effective index method treats each of the central ridge and the side etched regions as a 1-D multilayer slab waveguide in the z direction (see Fig. 3.5(b)) and solves for the effective index in each region. Then, as shown in Fig. 3.5(c), the effective indices of the ridge and etched regions form a three-layer effective dielectric stack in the x direction. Solving this 1-D dielectric stack approximates the effective index for the 2-D mode along with the lateral mode profile. For analysis of each one-dimensional waveguide we use the wave-transfer model described in Appendix A.

The photoabsorber fill factor, FF, is calculated using one-dimensional analysis explained in Appendix A. Then, the mode effective absorption coefficient, α_e, is obtained by multiplying the photoabsorber fill factor by the bulk absorption coefficient, α, of the absorbing material as discussed in Appendix A.2. It is useful to define an absorption length, l_{ab}, as a length after which the optical power drops off by a factor of e^{-1}.

Knowing the bulk absorption coefficient α of LTG-GaAs and the photoabsorber fill factor FF, one can readily calculate the absorption length l_{ab} from (A.12). Simulation results of the one-dimensional phototabsorber fill factor and the absorption length with respect to the upper cladding thickness for the core thickness of $h_3 = 0.3\mu m$ is shown in Fig. 3.6. For distribution of the optical power over a large area, an appropriate value for the absorption length is first selected, and the corresponding thickness for the upper cladding can be extracted from Fig. 3.6. Shown in Fig. 3.7 are the modal field distribution in 1-D multilayer optical waveguide with different upper cladding thicknesses and for TE modes. The photoabsorber

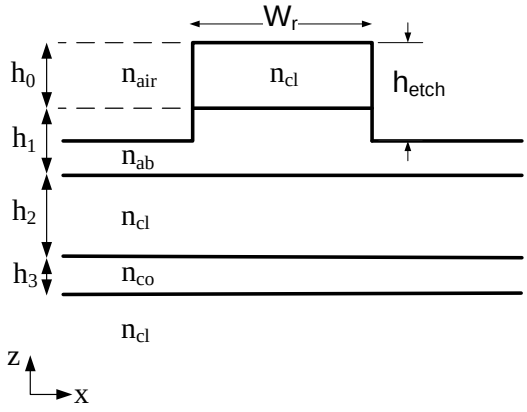

(a)

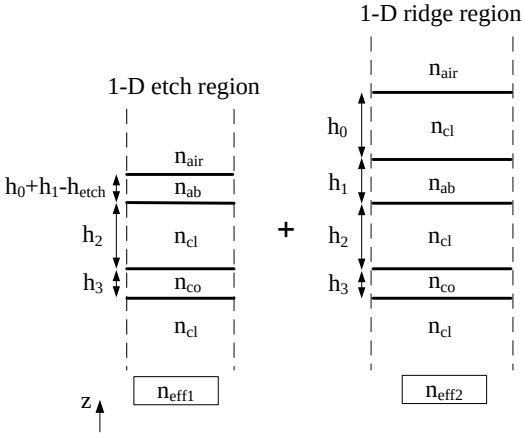

(b)

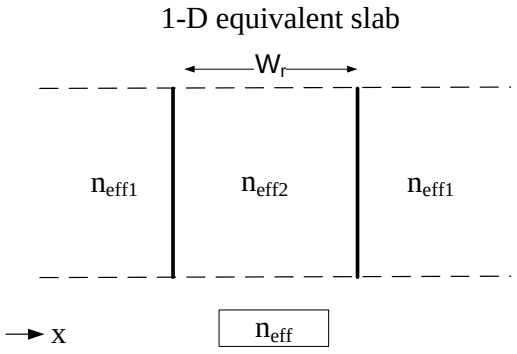

(c)

Figure 3.5: The treatment of a two-dimensional waveguide as the combination of two orthogonal one-dimensional waveguides using the effective index method. Propagation in the ridge waveguide is in y direction.

fill factor and the effective absorption coefficient for even and odd modes are also compared in Table 3.1. It should be noted that by choosing a proper value for h_2, the effective loss for the odd mode can be much higher than that of even mode. Therefore, the waveguide can be considered almost single mode.

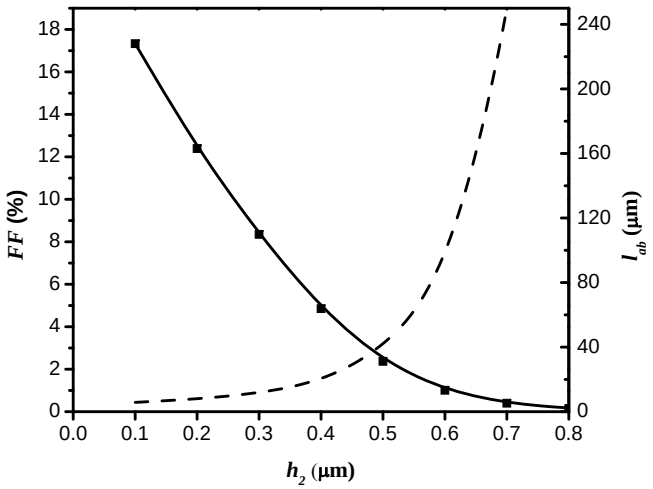

Figure 3.6: One-dimensional phototabsorber fill factor (solid line) and absorption length (dashed line) with respect to the upper cladding thickness. Other parameters were selected as $h_0 = 1\ \mu m$, $h_1 = 0.1\ \mu m$, $h_3 = 0.3\ \mu m$, and $\alpha = 1 \times 10^4\ \text{cm}^{-1}$ for LTG-GaAs at 780 nm.

Table 3.1: Comparison of photoabsorber fill factor and effective absorption coefficient between even and odd TE modes. Design parameters were chosen as $h_0 = 1\ \mu m$, $h_1 = 0.1\ \mu m$, $h_3 = 0.3\ \mu m$, and $\alpha = 1 \times 10^4\ \text{cm}^{-1}$.

$h_2(\mu m)$	$FF(\%)$, even	$FF(\%)$, odd	$\alpha_e(\text{cm}^{-1})$, even	$\alpha_e(\text{cm}^{-1})$, odd
0.1	17.3	14.8	1730	1480
0.2	12.4	21.8	1240	2180
0.3	8.4	26.4	840	2640
0.4	4.9	29.7	490	2970
0.5	2.4	31.9	240	3190
0.6	1.0	33.1	100	3310
0.7	0.4	33.6	40	3360

In lateral direction, the designs with the widest single mode ridge is desired as the wider ridge permits more power being coupled into the guide, and also larger absorber region being provided for better thermal load distribution in the absorber layer. The single mode condition for the symmetric slab shown in Fig. 3.5(c) is

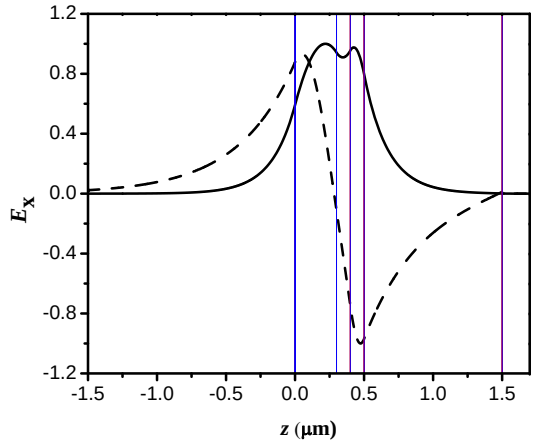

(a)

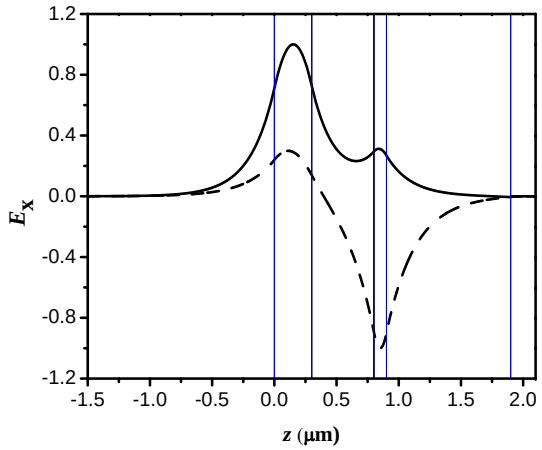

(b)

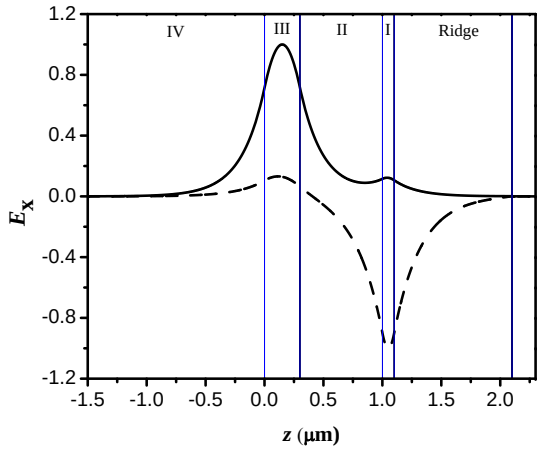

(c)

Figure 3.7: Even (solid line) and odd (dashed line) modes in 1-D multilayer waveguide for (a) $h_2 = 0.1\ \mu m$, (b) $h_2 = 0.5\ \mu m$, and (c) $h_2 = 0.7\ \mu m$. Other parameters: $h_0 = 1\ \mu m$, $h_1 = 0.1\ \mu m$, $h_3 = 0.3\ \mu m$. Vertical lines show the interfaces.

given by

$$W_r \leq \frac{\lambda_0}{2\sqrt{n_{eff2}^2 - n_{eff1}^2}} \tag{3.1}$$

Table 3.2 summarizes the calculated effective indices and the maximum ridge width with respect to the upper cladding thickness.

Table 3.2: Calculated effective indices and maximum ridge width based on EIM. Design parameters were selected as $h_0 = 1\ \mu m$, $h_1 = 0.1\ \mu m$, $h_3 = 0.3\ \mu m$, and $h_{etch} = 1.05\ \mu m$.

$h_2(\mu m)$	n_{eff2}	n_{eff1}	Δn_{eff}	$W_r(\mu m) \leq$
0.1	3.51444	3.49206	0.02238	0.98
0.2	3.50548	3.49463	0.01085	1.42
0.3	3.50066	3.49551	0.00515	2.05
0.4	3.49812	3.49583	0.00229	3.08
0.5	3.49689	3.49594	0.00095	4.78
0.6	3.49637	3.49598	0.00039	7.47
0.7	3.49616	3.49600	0.00016	11.66

The effective index method can be considered as a fast analysis and design tool. However, more accurate mode solving techniques, such as correlation method based on BPM, should be deployed in the final stages of the design. In the correlation method, an arbitrary field is launched into the structure and propagated via normal BPM. During the propagation, a correlation function between the input field and the propagating field is computed [67]. Then, Fourier transform of the computed correlation function should have a spectrum with peaks at the modal propagation constants. Finally, the corresponding modal fields can be obtained with a second propagation by beating the propagating field against the known propagation constants.

Using the initial parameters from EIM, we deploy the implemented correlation method in BeamPROB^{TM}, a commercial software based on BPM [68], to find the modal field distribution and the effective absorption coefficient for the 2-D optical waveguide. There are several considerations that are required to be considered when computing mode eigenvalues and eigenfunctions via the correlation method. One must launch a field which excites all the possible modes, e.g. a Gaussian beam launched off the center by half the waveguide width. Second, since the eigenvalues are obtained by taking the Fast Fourier Transform (FFT) of the correlation

function, the accuracy and bandwidth of the spectrum are determined by standard Fourier sampling. Namely, the narrowness of the peaks, which determines how closely spaced peaks can be resolved, is determined by the propagation length; the longer the propagation the better the resolution. Furthermore, the range of eigenvalues is determined by the sampling period; the shorter the sampling period the wider the range of eigenvalues [68].

Fig. 3.8 shows the modal field distribution obtained from semi-vectorial BPM for TE mode of the structure shown in Fig. 3.4(c). The optical waveguide parameters are given in Table 3.3. The modal analysis showed that the optical waveguide with the given parameters is single-mode.

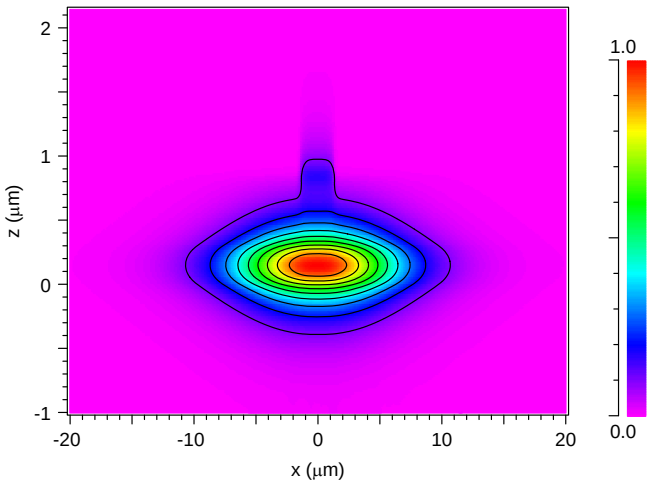

Figure 3.8: Cross sectional profile of the transverse electric field obtained from semi-vectorial BPM.

Table 3.3: Design parameters used in BPM simulation for the optical waveguide shown in Fig. 3.4(c).

$h_0(\mu m)$	$h_1(\mu m)$	$h_2(\mu m)$	$h_3(\mu m)$	$h_{etch}(\mu m)$	$h_4(\mu m)$
1	0.1	0.5	0.3	1.05	2
$W_r(\mu m)$	$\alpha(cm^{-1})$	$\lambda_0(\mu m)$	n_{ab}	n_{cl}	n_{co}
3	1×10^4	0.78	3.66	3.44	3.554

The photoabsorber fill factor, FF, calculated with one-dimensional analysis, as explained in Appendix A, assumes a uniform field distribution laterally, and therefore, it gives an upper limit on the achievable fill factor in a two-dimensional ridge waveguide for the same stack of dielectric layers in the ridge region. However, as seen in Fig. 3.8, the lateral confinement in the ridge is almost ten times smaller

than that in the slab core. We observed the same order of difference in the fill factor calculated from BPM and one-dimensional calculations. Therefore, to have more accurate fill factor from one-dimensional calculation, we define a correction factor, CF, as the ratio of the ridge width to the lateral beam width in the core slab. Then, the modified fill factor (or the absorption coefficient) calculated from one-dimensional analysis should be multiplied by the CF to give more accurate results.

Table 3.4 compares the calculated effective indices and the effective absorption coefficient for several upper cladding thicknesses obtained from EIM and correlation method. Other parameters are the same as those given in Table 3.3.

Table 3.4: Comparison between effective index method (EIM) and correlation method (CM) for 2-D optical waveguide.

$h_2(\mu m)$	n_{eff} (EIM)	n_{eff} (CM)	Modified $\alpha_e(\text{cm}^{-1})$ (EIM)	$\alpha_e(\text{cm}^{-1})$ (CM)	$l_{ab}(\mu m)$ (CM)
0.4	3.49727	3.49577	69.6	65.9	151.7
0.5	3.49635	3.49562	29.4	23.0	435.6
0.6	3.49607	3.49549	11.1	8.1	1239.9
0.7	3.49601	3.49547	4.0	3.0	3294.6

3.3 Photo-induced Carrier Transport

For analysis of semiconductor devices, various models such as Monte Carlo [69], hydrodynamic [70] and drift-diffusion [71] have been developed. Most of them are based on the solution of Poisson's equation along with the Boltzmann transport equation. In choosing the proper analysis model, it is apparent that a trade-off between accuracy and complexity should be performed.

3.3.1 Drift-Diffusion Model

We use the drift-diffusion model to calculate the generated photocurrent inside the fast photoconductive layers in the photomixer device. In this model, only the carrier continuity and carrier momentum conservation are included where as carrier energy conservation is left out. Despite this, drift-diffusion model is able to describe the main physical processes inside the photoconductor, such as optical generation of

carriers and currents, and field-screening effect. This model is also relatively simple in numerical implementation compared to other more rigorous models, leading to better convergence of the numerical algorithm and lower computational time.

The set of basic drift-diffusion equations in the time domain consists of Poisson's equation, continuity equations for electrons and holes, and current equations for electrons and holes as given below [72].

$$\nabla \cdot \left[\epsilon_r \nabla \phi(\mathbf{r};t)\right] = \frac{e}{\epsilon_0}\left[N_n(\mathbf{r};t) - N_p(\mathbf{r};t) - C_t(\mathbf{r};t)\right] \tag{3.2a}$$

$$\frac{\partial N_{n,p}(\mathbf{r};t)}{\partial t} = \pm\frac{1}{e}\nabla \cdot \mathbf{J}_{n,p}(\mathbf{r};t) - R(\mathbf{r};t) + G(\mathbf{r};t) \tag{3.2b}$$

$$\mathbf{J}_{n,p}(\mathbf{r};t) = -e\mu_{n,p}N_{n,p}(\mathbf{r};t)\nabla\phi(\mathbf{r};t) \pm eD_{n,p}\nabla N_{n,p}(\mathbf{r};t) \tag{3.2c}$$

where subscripts n and p distinguish the parameters associated with electron and hole carriers, respectively, ϕ is the electric potential, $N_{n,p}(\mathbf{r};t)$ is carrier density, $\mathbf{J}_{n,p}(\mathbf{r};t)$ is carrier current density, $R(\mathbf{r};t)$ and $G(\mathbf{r};t)$ are carrier recombination and generation rates, respectively, $C_t(\mathbf{r};t)$ is the net trap concentration filled by charge inside semiconductor, $\mu_{n,p}$ is carrier mobility, $D_{n,p}$ is carrier diffusion coefficient, ϵ_0 is vacuum permittivity, ϵ_r is relative permittivity, and e is the electron charge.

It is important to note that when the cross sectional dimensions of the device are comparable with the operating wavelengths, Poisson's equation may not give an accurate representation of the electric field in terms of the distributed time-varying charges, and instead the wave equation should be used. In this case, the basic drift-diffusion equations given in (3.2) are replaced with the following set of equations.

$$\nabla \times \nabla \times \mathbf{E}(\mathbf{r};t) + \frac{\epsilon_r}{c_0^2}\frac{\partial^2 \mathbf{E}(\mathbf{r};t)}{\partial^2 t} = -\mu_0 \frac{\partial}{\partial t}\left[\mathbf{J}_n(\mathbf{r};t) + \mathbf{J}_p(\mathbf{r};t)\right] \tag{3.3a}$$

$$\frac{\partial N_{n,p}(\mathbf{r};t)}{\partial t} = \pm\frac{1}{e}\nabla \cdot \mathbf{J}_{n,p}(\mathbf{r};t) - R(\mathbf{r};t) + G(\mathbf{r};t) \tag{3.3b}$$

$$\mathbf{J}_{n,p}(\mathbf{r};t) = e\mu_{n,p}N_{n,p}(\mathbf{r};t)\mathbf{E}(\mathbf{r};t) \pm eD_{n,p}\nabla N_{n,p}(\mathbf{r};t) \tag{3.3c}$$

where $\mathbf{E}(\mathbf{r};t)$ is the electric vector field, c_0 is the speed of light in vacuum, and μ_0 is the permeability of vacuum. It is important to note that higher accuracy is obtained at the expense of greater complexity in using system of equations in (3.3) instead of system of equations in (3.2).

The set of basic drift-diffusion equations given in (3.2) can be manipulated by substituting the current equation (3.2c) into the continuity equations (3.2b) to yield a system of three partial differential equations with dependent variables ϕ, N_n, and N_p.

$$\nabla \cdot \big[\epsilon_r \nabla \phi\big] = \frac{e}{\epsilon_0}\big[N_n - N_p - C_t\big] \tag{3.4a}$$

$$\frac{\partial N_n}{\partial t} = \nabla \cdot \big[D_n \nabla N_n - \mu_n N_n \nabla \phi\big] - R + G \tag{3.4b}$$

$$\frac{\partial N_p}{\partial t} = \nabla \cdot \big[D_p \nabla N_p + \mu_p N_p \nabla \phi\big] - R + G \tag{3.4c}$$

The compact system of the basic drift-diffusion equations given in (3.4) represents the basis of the numerical algorithm developed for calculation of the photocurrent.

3.3.2 Generation-Recombination Process

Carrier Generation-Recombination (GR) process makes a balance between the electron and hole concentrations inside the semiconductor crystal. Many GR processes have been discovered and explained so far among which the Shockley-Read-Hall (SRH) and the Auger processes have the most important roles in our device modeling.

The SRH GR is a phonon transition which occurs due to trapping of the carriers in the trap states created by the defects in e.g. Low-Temperature-Grown photoconductors such as LTG-GaAs. LTG-GaAs which has been predominantly used in terahertz photomixers is deposited by molecular beam epitaxy (MBE) at low substrate temperature ~ 200°C in an As-rich environment and then is annealed under an arsenic overpressure at higher temperature e.g. 600°C for 10 to 30 min or 700°C or higher for 30 s or less [73]. In LTG- GaAs, because of the low substrate temperature and As-rich growth conditions, about 1% or less excess arsenic is incorporated into the GaAs matrix. When LTG-GaAs is annealed, the arsenic precipitates in the form of clusters. The arsenic clusters in annealed LTG-GaAs results in a large trap density, that consequently results in a high resistivity ($\sim 10^6$ $\Omega-$cm), large breakdown field (~ 50 V/μm), and extremely short carrier lifetime (~ 0.2 ps) [73].

In LTG-GaAs photoconductor, SRH GR process has a major role because of the existence of high density of trap states. There are four partial processes involved in SRH GR process [72]:

- Electron capture - an electron is transferred from the conduction band to a trap state, and fills up the trap state.
- Hole capture - an electron is transferred from the trap state to the valence band and recombines with a hole. The trap state becomes empty.
- Electron emission - an electron from the trap state is transferred to the conduction band, and the trap state becomes empty.
- Hole emission - an electron from the valence band is transferred to a trap state, leaving a hole in the valence band. The trap state is filled up.

Combining the above partial processes and assuming that each trap state has an energy level located in the energy band gap and denoted by E_t^i (superscript i distinguishes discrete levels), the net recombination rate in the presence of electron traps is mathematically given by [72]

$$R^{SRH} = \sum_i \frac{N_n N_p - n_{int}^2}{\tau_p^i (N_n + n_1^i) + \tau_n^i (N_p + p_1^i)} \tag{3.5}$$

where $n_1^i = \frac{n_{int}}{d_{gen}} \exp(E_t^i / K_B T)$ and $p_1^i = n_{int} d_{gen} \exp(-E_t^i / K_B T)$, n_{int} is the intrinsic carrier concentration, the parameter d_{gen} accounts for degeneracy effects, τ_n^i and τ_p^i are electron and hole lifetimes, respectively.

For the analysis of electron trapping process based on SRH model, let N_t^i represents the trap density for the i^{th} level, and let further the fraction of occupied traps at each energy level is denoted by f_t^i (a maximum value of 1 for f_t^i, indicating a completely full trap state). Then, the dynamics of trap state occupied by electrons at each level can be expressed as

$$\frac{\partial (f_t^i N_t^i)}{\partial t} = \frac{(1 - f_t^i) N_n - f_t^i n_1^i}{\tau_n^i} - \frac{f_t^i N_p - (1 - f_t^i) p_1^i}{\tau_p^i} \tag{3.6}$$

The differential equation given in (3.6) is an additional equation which is solved along with the basic drift-diffusion system of equations. Equation (3.6) is coupled to Poisson's equation given in (3.4a) through the occupied trap concentration term C_t

$$C_t(\mathbf{r}; t) = N_D^+ - N_A^- - \sum_i f_t^i N_t^i \tag{3.7}$$

where N_D^+ and N_A^- are densities of ionized deep-donor and -acceptor traps, respectively, and $(f_t^i N_t^i)$ represents density of occupied shallow traps at level i.

The Auger GR is a second important process which involves three particle transitions. Four partial processes are involved:

- Electron capture - an electron is transferred from the conduction band to the valance band, and recombines with a hole. The excess energy of the electron is released to another electron in the conduction band.
- Hole capture - an electron is transferred from the conduction band to the valance band, and recombines with a hole. The excess energy of the electron is released to another hole in the valance band.
- Electron emission - an electron from the valance band is transferred to the conduction band by consuming the energy of a high energetic electron in the conduction band. A hole is left in the valance band.
- Hole emission - an electron from the valance band is transferred to the conduction band by consuming the energy of a high energetic hole in the valance band. A hole is left in the valance band edge.

The Auger recombination rate can be mathematically expressed as [72]

$$R^{AU} = (C_{cn}^{AU} N_n + C_{cp}^{AU} N_p)(N_n N_p - n_{int}^2) \tag{3.8}$$

where C_{cn}^{AU} and C_{cp}^{AU} are the Auger capture coefficients for the electron and hole, respectively, and are obtained experimentally.

3.3.3 Optical Generation

Upon the optical excitation of the photoconductor, photo-induced electron-hole pairs are generated through absorption of photons. The optical generation rate is given by [63]

$$G(\mathbf{r}; t) = \frac{\alpha \lambda_0}{h c_0} I_{opt}(\mathbf{r}; t) \tag{3.9}$$

where $I_{opt}(\mathbf{r}; t)$ is the optical power density, and is obtained through the analysis performed in Section 3.2, h is Plank's constant, c_0 is velocity of light in free space, λ_0 is the optical wavelength in free space, and α is the optical absorption coefficient inside the photoabsorber layer.

3.3.4 Boundary Conditions

Solving the system of partial differential equations given in (3.4) needs proper boundary conditions for the dependent variables ϕ, N_n and N_p. A set of boundary conditions for the ohmic contacts and the interface between a semiconductor and an insulator are briefly discussed.

Ohmic Metallic Contacts

The boundary condition for ohmic contacts between a metal and semiconductor are characterized by vanishing total space charge in the semiconductor at the interface. Therefore, the impressed charge accumulation at the interface does not happen, and the incoming carriers to the boundary can move freely in both directions, depending on the applied potential. For ohmic contacts, the boundary conditions for electric potential and carrier concentrations are given by

$$\phi = \phi_b + \phi_a \tag{3.10}$$

$$N_n = \frac{1}{2}\left[\sqrt{(N_D^+ - N_A^-)^2 + 4n_{int}^2} + (N_D^+ - N_A^-)\right] \tag{3.11}$$

$$N_p = \frac{1}{2}\left[\sqrt{(N_D^+ - N_A^-)^2 + 4n_{int}^2} - (N_D^+ - N_A^-)\right] \tag{3.12}$$

where ϕ_b is the built-in potential due to the fixed charge distribution $(N_D^+ - N_A^-)$, and ϕ_a is the bias potential applied to the metal contact. It is noted that an ohmic contact is characterized by Dirichlet boundary conditions.

Semiconductor-insulator interface

The boundary conditions for the interface between a semiconductor and an insulating material are given by

$$\epsilon_{sem}\frac{\partial\phi}{\partial n}\Big|_{sem} - \epsilon_{ins}\frac{\partial\phi}{\partial n}\Big|_{ins} = \rho_s \tag{3.13}$$

$$\mathbf{J}_n \cdot \hat{\mathbf{n}} = -eR^{Surf} \tag{3.14}$$

$$\mathbf{J}_p \cdot \hat{\mathbf{n}} = eR^{Surf} \tag{3.15}$$

where ϵ_{sem} and ϵ_{ins} are permittivities of the semiconductor and the insulating material, respectively, ρ_s is the surface charge density at the interface, R^{Surf} is the surface recombination rate, and $\hat{\mathbf{n}}$ is the unit normal vector at the boundary. It is good to point out that at the interface between the semiconductor and air, assuming no surface charges and vanishing surface recombination velocities, conditions (3.13)-(3.15) transform into Neumann boundary conditions.

3.3.5 Scaling

The dependent variables ϕ, N_n and N_p in the basic drift-diffusion equations are different in value by several orders of magnitude. This can create significant difficulties in solving the system of equations numerically. Therefore, the first step in solving (3.4) is scaling. The scaling factors are summarized in Table 3.5 [72].

Table 3.5: Scaling factors for the basic drift-diffusion equations

Quantity	Scaling factor
$\lvert\mathbf{r}\rvert$	r_0=maximum dimension
ϕ	$\phi_0=\frac{K_B T}{e}$, K_B Boltzmann constant, T absolute temperature
N_n, N_p, C_t	C_0=maximum doping concentration
D_n, D_p	D_0=maximum diffusion constant
$\lvert\mathbf{E}\rvert$	$\frac{\phi_0}{r_0}$
μ_n, μ_p	$\frac{D_0}{\phi_0}$
R, G	$\frac{D_0 C_0}{r_0^2}$
t	$\frac{r_0^2}{D_0}$
$\lvert\mathbf{J}_n\rvert, \lvert\mathbf{J}_p\rvert$	$-\frac{eD_0C_0}{r_0}$

After scaling, the compact drift-diffusion equations transform into

$$\lambda^2 \nabla \cdot \left[\epsilon_r \nabla \hat{\phi}\right] = \left[\hat{N}_n - \hat{N}_p - \hat{C}_t\right] \tag{3.16a}$$

$$\frac{\partial \hat{N}_n}{\partial \hat{t}} = \nabla \cdot \left[\hat{D}_n \nabla \hat{N}_n - \hat{\mu}_n \hat{N}_n \nabla \hat{\phi}\right] - \hat{R} + \hat{G} \tag{3.16b}$$

$$\frac{\partial \hat{N}_p}{\partial \hat{t}} = \nabla \cdot \left[\hat{D}_p \nabla \hat{N}_p + \hat{\mu}_p \hat{N}_p \nabla \hat{\phi}\right] - \hat{R} + \hat{G} \tag{3.16c}$$

where

$$\lambda^2 = \frac{\phi_0 \epsilon_0}{e C_0 r_0^2} \tag{3.17}$$

In (3.16), the scaled variables and parameters are shown as ($\hat{.}$). The scaled system of the basic drift-diffusion equations in (3.16) is numerically more stable than the non-scaled system in (3.4).

3.3.6 Results and Discussion

Fig. 3.9 shows the cross section of a travelling wave Metal-Semiconductor-Metal (MSM) photomixer. It consist of an optical waveguide with the physical and geometrical parameters given in Table 3.3 integrated with a coplanar stripline. The metallic strips act as biasing electrodes as well as THz transmission line. A DC voltage, V_{DC}, is applied between two electrodes to provide the necessary DC electric field for photocurrent excitation.

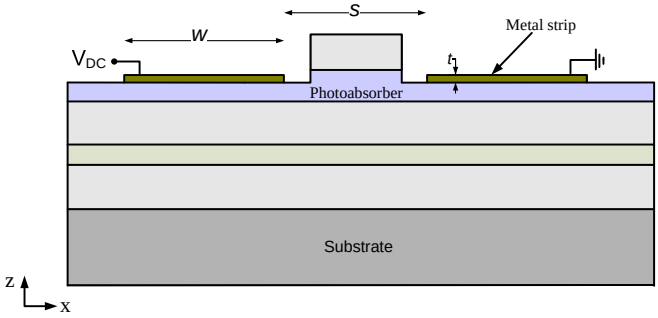

Figure 3.9: Cross section of a travelling wave MSM photomixer.

Theory of photomixing has been very well established in the litrature [74, 75], and here we only use the relevant results. Upon the excitation of the optical waveguide with two detuned laser whose frequency difference falls in THz region, photo-induced electron-hole pairs are generated inside the photoabsorber. The density of

carriers is modulated with the beat frequency, and terahertz photocurrent is excited inside the photoabsorber due to the applied DC voltage. The cross sectional terahertz photocurrent is approximated by

$$\mathbf{J}_{THz} = \eta \left[\frac{\mathbf{J}_n}{\sqrt{1 + (\omega_{THz}\tau_n)^2}} + \frac{\mathbf{J}_p}{\sqrt{1 + (\omega_{THz}\tau_p)^2}} \right] \tag{3.18}$$

where $0 < \eta \leq 1$ is the modulation index or grating contrast, $\mathbf{J}_{n,p}$ is the time-averaged carrier current density calculated from (3.2c), ω_{THz} is the angular terahertz frequency, and $\tau_{n,p}$ is the carrier recombination life time. To solve the basic drift-diffusion equations given in (3.4) along with the equation governing the dynamics of trap states in (3.6) at the cross section of MSM photomixer, Taurus Medici [76], a commercial 2-D device simulator, was used. Using the parameters given in Table 3.6, Fig. 3.11 shows the carrier photogeneration inside the LTG-GaAs layer for the total optical power of 42mW. Fig. 3.11 shows the cross sectional DC photocurrent with respect to the applied voltage for the total optical power of 42mW.

Table 3.6: Physical parameters of the MSM photomixer with LTG-GaAs as photoabsorber

Parameter	Value
Strip width, w	18.4 μm
Electrode gap, s	6.2 μm
Strip thickness, t	0.3 μm
Operating temperature, T_0	300K
Modulation index, η	1
Laser central wavelength, λ	780nm
Absorption coefficient at $\lambda = 780$nm, α	$^*10000\text{cm}^{-1}$
Electron saturation velocity, v_{sn}	$^*4 \times 10^4$m/s
Hole saturation velocity, v_{sp}	$^*1 \times 10^4$m/s
Low field electron lifetime, τ_{n0}	*0.1ps
Low field hole lifetime, τ_{p0}	*0.4ps
Low field electron mobility, μ_{n0}	$^{**}200\text{cm}^2$/Vs
Low field hole mobility, μ_{p0}	$^{**}50\text{cm}^2$/Vs
Carrier trap density, N_t	$^{**}3 \times 10^{18}\text{cm}^{-3}$

References: *[75], **[77]

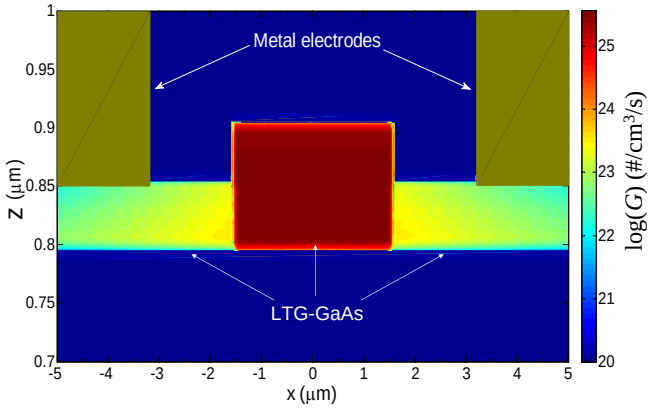

Figure 3.10: Carrier photogeneration inside the LTG-GaAs layer for the total optical power of 42 mW.

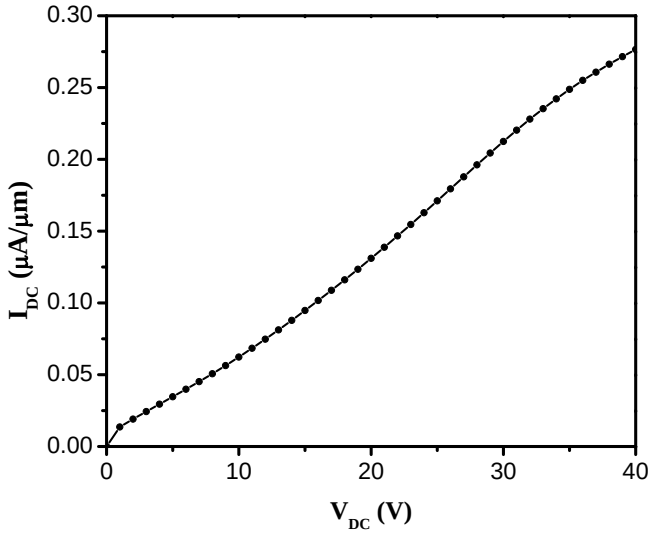

Figure 3.11: Cross sectional DC photocurrent of the MSM photomixer with total optical power of 42 mW.

It is known that in LTG-GaAs material the carrier life time at high DC electric field increases. A model presented in [77] for dependency of carrier life time on applied field was used to find the photo-current presented in Fig. 3.11. The amplitude of cross sectional THz photocurrent versus beat frequency is illustrated in Fig. 3.12 for different DC voltages. The total optical power is assumed 42 mW. As expected, the frequency bandwidth of the photomixer decreases by increasing the applied DC voltage as shown in Fig. 3.12. This is due to the increase of the carrier life time at higher DC electric fields.

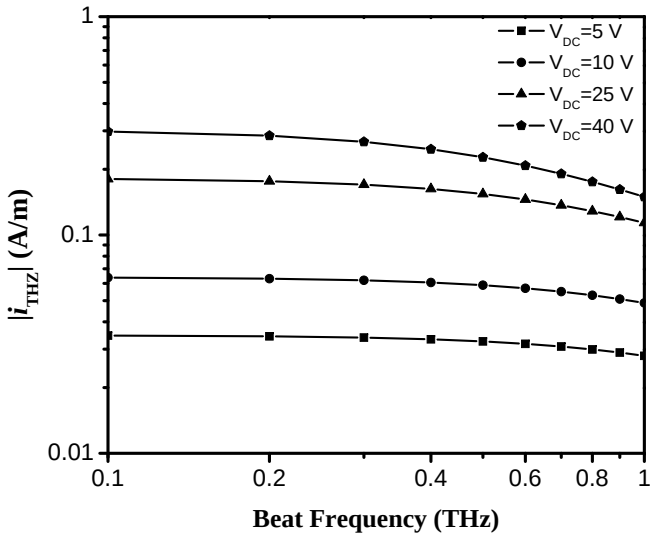

Figure 3.12: Cross sectional THz photocurrent versus beat frequency and for several DC voltage. The total optical power is assumed 42 mW.

3.4 Electromagnetic Modeling of Active Region

In this Section, the aim is to develope a theoretical tool to determine the guided electromagnetic field generated by the photocurrent in the active region of the photomixer. To do so, it is convenient to express the field in terms of the modal fields in the structure. The main advantage of using modes is that they provide the field distribution over the whole space, once their amplitude are known on a given section. In fact, once modal amplitudes are known, it is sufficient to multiply each of them by the corresponding propagation factor to obtain the field at any given distance.

3.4.1 Modal Analysis of Coplanar Stripline (CPS)

Cross section of the coplanar stripline is shown in Fig. 3.13. It consists of two metallic strips with the width of w running in parallel on a dielectric substrate with the relative permittivity of ϵ_r and thickness of d. The strips are separated with the distance of s. For modal analysis, it is assumed that the structure is uniform along the y direction, and also is infinite.

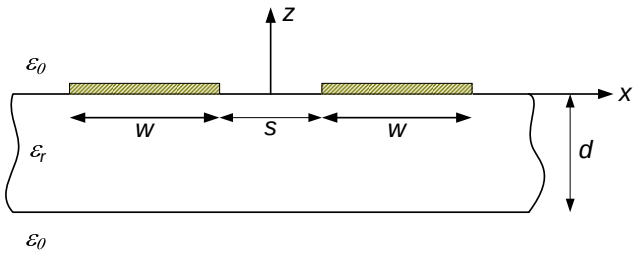

Figure 3.13: Cross section of a coplanar stripline.

Coplanar stripline is an open waveguide and its complete spectra includes both discrete and continuous spectrum representing bound modes and radiation modes, respectively [78]. Bound modes falls into two categories; the guided modes which propagates along the CPS and their modal field distribution is mostly concentrated around the strips. And surface waves which propagate in an angle away from the strips and their modal field is distributed all over the dielectric substrate.

On a uniform coplanar transmission line, it is expected for the dominant mode to be purely guided mode, and this is true at lower and middle ranges of frequency. However, as the frequency exceeds a critical value determined by the dielectric constant and the relative cross-section dimensions, the dominant mode wave number becomes complex and power leaks away into the substrate at an angle from the transmission line in the form of a surface wave. In fact, CPS dominant mode will become leaky and lose energy by exciting surface waves once the dispersion curve for the lowest surface wave far from the CPS center electrodes crosses the dispersion curve for the dominant CPS mode [79]. The mode wave number becomes complex if the structure is infinite laterally; if it is finite on the sides, the wave number may remain real and the leaking power still spreads out but is reflected from the sides [80]. In any case, power can be coupled to a neighbouring line resulting undesired cross-talks.

Shah et al. have used electrooptic sampling to measure photoconductively generated signals on coplanar striplines [81]. They performed field measurements at

positions laterally displaced from the center of the transmission line to demonstrate that the surface waves are indeed excited in THz range.

To avoid the excitation of surface waves one way is to add a superstrate for elimination of the dielectric inhomogeneity encountered by the electric field [82]. However, tiny air gaps or an insufficient thickness of the superstrate layer degrades the performance. A superior approach appears to be the reduction of the substrate thickness, as in the guiding structures demonstrated by Keil et al. [83], where the substrate material has been mostly etched away, leaving almost free-standing metal coplanar electrodes, or by Cheng et al. [84], where a CPS has been fabricated on a 1.4-μm-thick membrane.

From the design point of view, the thickness of the SI-GaAs substrate in our structure should be selected small enough in order to prevent the leakage of the guided mode into the surface waves on the one hand, but on the other hand the chip should have enough rigidity and mechanical strength for handling and manipulation. To study all surface waves supported in a multilayer substrate, and to find the characteristic equation governing their propagation constants, transverse resonance technique [85] was deployed as it is straightforward and easy to implement. Formulation of the surface wave characteristic equation based on this technique is presented in the following.

Surface waves from transverse resonance

Fig. 3.14 shows an N-layer substrate which is transversely unbounded with respect to z axis. Each layer can have different dielectric property, $n_i = \sqrt{\epsilon_{ri}}$, and thickness, d_i. Bellow and above the substrate designated by layer 0 and $N+1$ can be either half space or ground plane. It is assumed without loss of generality that surface waves propagate in y direction.

It has been shown [86] that electric and magnetic field components parallel to the interfaces of a planar multilayer substrate, as in Fig. 3.14, can be interpreted as voltage and current, respectively, in a cascaded transmission line representation. Therefore, the original vector problem in space domain is reduced to a scalar transmission line problem which is much easier to solve. It should be noted that there are two types of transmission line involved, one for TE^z modes and another for TM^z modes. The solution of equations for both types of transmission lines is the same except for their characteristic impedances which are different. The characteristic impedance in the i^{th} $(0 \leqslant i \leqslant N+1)$ layer is given by

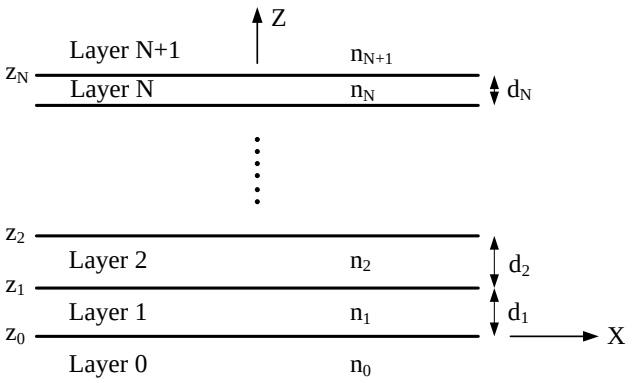

Figure 3.14: A multilayer substrate.

$$Z_{0i} = \begin{cases} \frac{\omega\mu_0}{k_{zi}} & \text{TE-to-}z \\ \frac{k_{zi}}{\omega\epsilon_0\epsilon_{ri}} & \text{TM-to-}z \end{cases} \tag{3.19}$$

where ω is the angular frequency, μ_0 and ϵ_0 are permeability and permittivity of free-space, respectively, and k_{zi} is the transverse wave number in the i^{th} layer which is related to the propagation constant in y direction, β, through

$$k_i^2 = k_{zi}^2 + \beta^2 \tag{3.20}$$

where $k_i = \omega\sqrt{\mu_0\epsilon_0\epsilon_{ri}}$. From transmission line theory, total impedance seen from the interface at $z = z_j$ downward, $Z_j^{\downarrow}$, is given by

$$Z_j^{\downarrow}(\beta,\omega) = Z_{0j}\frac{Z_{j-1}^{\downarrow} + jZ_{0j}\tan(k_{zj}d_i)}{Z_{0j} + jZ_{j-1}^{\downarrow}\tan(k_{zj}d_j)}, \qquad 1 \leqslant j \leqslant N \tag{3.21}$$

$$Z_0^{\downarrow} = \begin{cases} Z_{00} & \text{Half space} \\ 0 & \text{Ground plane} \end{cases} \tag{3.22}$$

As seen in (3.21), total impedance at j^{th} interface is recursively related to that of $(j-1)^{th}$ interface. Similarly, total impedance seen from the interface at $z = z_j$ upward, $Z_j^{\uparrow}$, is given by

$$Z_j^{\uparrow}(\beta,\omega) = Z_{0j}\frac{Z_{j+1}^{\uparrow} + jZ_{0j}\tan(k_{zj}d_j)}{Z_{0j} + jZ_{j+1}^{\uparrow}\tan(k_{zj}d_j)}, \qquad 0 \leqslant j \leqslant N-1 \tag{3.23}$$

$$Z_N^{\uparrow} = \begin{cases} Z_{0N} & \text{Half space} \\ 0 & \text{Ground plane} \end{cases} \tag{3.24}$$

Remembering that surface waves are transversely confined in the substrate, transverse resonance provides necessary and sufficient condition for such modes to exist. At transverse resonance the total impedance at any interface is zero.

$$Z_j^{\downarrow}(\beta,\omega) + Z_j^{\uparrow}(\beta,\omega) = 0, \qquad 0 \leqslant j \leqslant N \tag{3.25}$$

Equation (3.25) is the dispersion equation governing the propagation constant of all surface waves in a multilayer substrate. At any given frequency, all the real roots of (3.25) represented by $\beta = \beta_n$ ($n = 0, 1, 2, ...$ is the mode order), which lies between minimum and maximum of k_i, constitute a discrete spectrum corresponding to all possible surface waves supported by the multilayer substrate.

Using (3.25), Fig. 3.15 shows the normalized propagation constant or the effective index, $n_{eff} = \frac{\beta}{k_0}$, versus frequency for all possible surface waves supported in a symmetric dielectric slab waveguide. Layer parameters were chosen as follow; $N = 1$, $\epsilon_{r1} = 12.9$, $d_1 = 150\mu m$ in Fig. 3.15(a) and (b), and $d_1 = 20\mu m$ in Fig. 3.15(c) and (d). Layer 2 is half-space with $\epsilon_{r2} = 1$, layer 0 is half-space with $\epsilon_{r0} = 1$ in Fig. 3.15(a) and (c), and is ground plane in Fig. 3.15(b) and (d).

For a symmetric dielectric slab waveguide the cut-off frequency, at which $\beta = k_0$, of the n^{th} order surface wave is given by

$$f_c = n\frac{c}{2d_1\sqrt{\epsilon_{r1} - \epsilon_{r0}}} \tag{3.26}$$

Therefore, by decreasing the slab thickness, d_1, the cut-off frequency inversely increases, and by choosing a proper thickness, all higher order surface waves are suppressed within a given frequency range of interest as demonstrated in Fig. 3.15(c) and Fig. 3.15(d). It is noted that since the cut-off frequency of TE_0 and TM_0 modes is zero, they can exist at any given frequency. However, by choosing proper design values for d, w, and s in Fig. 3.13, it is possible to make the propagation constant of the fundamental guided mode of the CPS greater than that of TE_0 and TM_0 modes to prevent the leakage. In the next subsection, a formulation for hybrid mode analysis is presented through which propagation constant and modal field distribution of CPS guided modes can be obtained.

Hybrid Mode Formulation

Presence of the strips in the CPS structure produces transverse diffraction which can not be represented by TE or TM modes alone, and rigorously hybrid modes

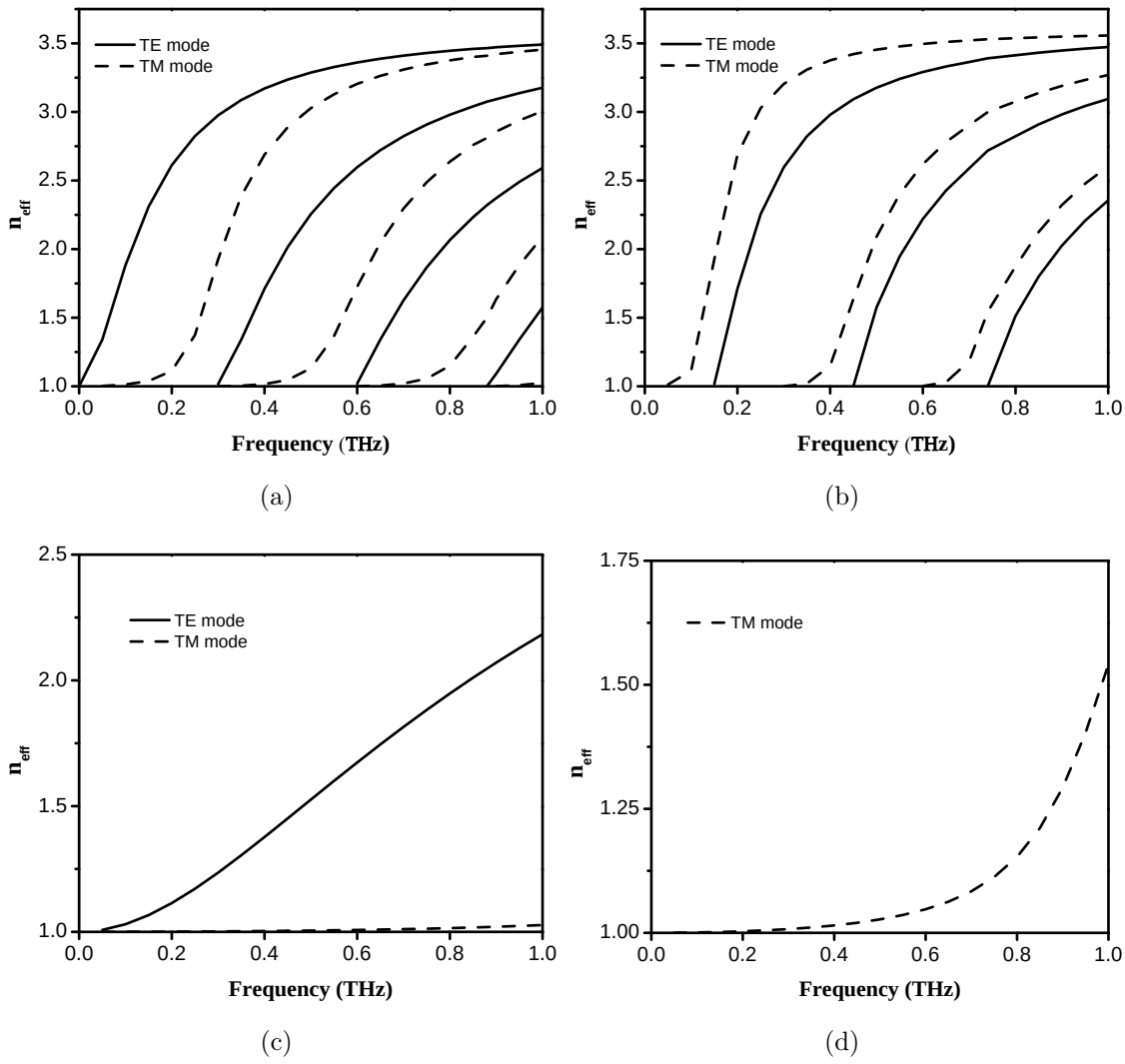

Figure 3.15: Normalized propagation constant versus frequency for a symmetric dielectric slab waveguide with (a) $d_1 = 150\ \mu m$ without ground plane (b) $d_1 = 150\ \mu m$ with ground plane (c) $d_1 = 20\ \mu m$ without ground plane and (d) $d_1 = 20\ \mu m$ with ground plane. For this simulation $\epsilon_{r0} = \epsilon_{r2} = 1$, and $\epsilon_{r1} = 12.9$.

should be considered. Assuming that the infinite axis of the guide is along the y-axis, as shown in Fig. 3.13, and the wave is propagating in the y direction, the guided modal fields can be expressed as

$$\mathbf{E}(x,y,z) = \mathbf{E}(x,z)e^{j(\omega t-\beta y)} \tag{3.27}$$
$$\mathbf{H}(x,y,z) = \mathbf{H}(x,z)e^{j(\omega t-\beta y)} \tag{3.28}$$

where ω denotes the angular frequency and β denotes the propagation constant. Substituting these into the source-free Maxwell's equations yields

$$\frac{\partial E_y}{\partial z} = -j\beta E_z + j\omega\mu_0 H_x \tag{3.29a}$$
$$\frac{\partial E_y}{\partial x} = -j\beta E_x - j\omega\mu_0 H_z \tag{3.29b}$$
$$\frac{\partial E_z}{\partial x} - \frac{\partial E_x}{\partial z} = j\omega\mu_0 H_y \tag{3.29c}$$
$$\frac{\partial H_y}{\partial z} = -j\beta H_z - j\omega\epsilon E_x \tag{3.29d}$$
$$\frac{\partial H_y}{\partial x} = -j\beta H_x + j\omega\epsilon E_z \tag{3.29e}$$
$$\frac{\partial H_z}{\partial x} - \frac{\partial H_x}{\partial z} = j\omega\epsilon E_y \tag{3.29f}$$

It should be noted that the permittivity in (3.29d)-(3.29f) is a function of the transverse coordinate z, namely, $\epsilon = \epsilon(z)$. Complete determination of the fields reduces to find longitudinal components, E_y and H_y, which satisfy proper boundary conditions. The differential equations governing E_y and H_y can be derived from (3.29a)-(3.29f) as

$$-\frac{\partial}{\partial x}\left(\frac{\mu_0}{k_t^2}\frac{\partial H_y}{\partial x}\right) - \frac{\partial}{\partial z}\left(\frac{\mu_0}{k_t^2}\frac{\partial H_y}{\partial z}\right) + \frac{\beta}{\omega}\left[\frac{\partial}{\partial z}\left(\frac{1}{k_t^2}\frac{\partial E_y}{\partial z}\right) - \frac{\partial}{\partial x}\left(\frac{1}{k_t^2}\frac{\partial E_y}{\partial z}\right)\right] - \mu_0 H_y = 0 \tag{3.30a}$$
$$-\frac{\partial}{\partial x}\left(\frac{\epsilon}{k_t^2}\frac{\partial E_y}{\partial x}\right) - \frac{\partial}{\partial z}\left(\frac{\epsilon}{k_t^2}\frac{\partial E_y}{\partial z}\right) - \frac{\beta}{\omega}\left[\frac{\partial}{\partial z}\left(\frac{1}{k_t^2}\frac{\partial H_y}{\partial z}\right) - \frac{\partial}{\partial x}\left(\frac{1}{k_t^2}\frac{\partial H_y}{\partial z}\right)\right] - \epsilon E_y = 0 \tag{3.30b}$$

where $k_t^2 = (\epsilon_r k_0^2 - \beta^2)$ is the transverse wavenumber, ϵ_r is the relative permittivity, and $k_0 = \omega\sqrt{\mu_0\epsilon_0}$ is the free space wavenumber. System of partial differential

equation given in (3.30) has no closed form solution in general, and a numerical scheme such as Finite Element Method (FEM) should be deployed.

The E_y-H_y scalar formulation given in (3.30) suffers from two major difficulties when an FEM solver is used; the first is the occurrence of non-physical solutions, and the second is its inability to treat general anisotropic materials, for which the permittivity and/or permeability tensors can not be reduced to a diagonalized form [87]. To overcome these difficulties, one can use three-component formulation governing electric or magnetic field vector with three components. Since we consider a non-magnetic multilayer structure within which the magnetic field is continuous, it is advantageous to use the magnetic field as the working quantity. The magnetic field satisfies the vector differential equation given as

$$\nabla \times (\frac{1}{\epsilon_r} \nabla \times \mathbf{H}) - k_0^2 \mathbf{H} = 0 \tag{3.31}$$

In the context of variational FEM, after following a few mathematical steps as explained in [87, pp. 254–256], the functional of (3.31) can be discretized as

$$\begin{bmatrix} A_{xx}(\beta) & A_{xy}(\beta) & A_{xz}(\beta) \\ A_{yx}(\beta) & A_{yy}(\beta) & A_{yz}(\beta) \\ A_{zx}(\beta) & A_{zy}(\beta) & A_{zz}(\beta) \end{bmatrix} \begin{bmatrix} H_x \\ -jH_y \\ H_z \end{bmatrix} = k_0^2 \begin{bmatrix} B_x & 0 & 0 \\ 0 & B_y & 0 \\ 0 & 0 & B_z \end{bmatrix} \begin{bmatrix} H_x \\ -jH_y \\ H_z \end{bmatrix} \tag{3.32}$$

where the matrices are assembled from their corresponding elemental matrices as described in [87]. The system of equation in (3.32) is a symmetric generalized eigenvalue problem. The matrices involved contain the unknown parameter β only. Therefore, given a specific value for β, one can solve (3.32) for the eigenvalue k_0 and by repeating this one may generate the desired dispersion curve. Following the calculation of the eigenvalues, the corresponding eigen vectors $\mathbf{H}$ or the modal fields are obtained from (3.32).

To enforce boundary conditions, with no surface currents present, the interface conditions must be fulfilled.

$$\hat{\mathbf{z}} \times [\mathbf{E}_i - \mathbf{E}_{(i+1)}] = \mathbf{0} \tag{3.33}$$

$$\hat{\mathbf{z}} \times [\mathbf{H}_i - \mathbf{H}_{(i+1)}] = \mathbf{0} \tag{3.34}$$

Condition 3.33 is the natural boundary condition which comes from the three-component formulation, and is implicitly enforced during the FEM solution process.

The condition for magnetic field is best satisfied by choosing proper interpolation basis functions such as Lagrange interpolation polynomials.

Assuming a finite thickness for the conducting strips of the CPS, zeroth order impedance boundary condition [88, Appendix A] can be applied on the strip surfaces.

$$\hat{\mathbf{n}} \times \mathbf{E} = Z_c \hat{\mathbf{n}} \times (\hat{\mathbf{n}} \times \mathbf{H}) \tag{3.35}$$

$$Z_c = \sqrt{\frac{\mu_0}{\epsilon_c' - j\epsilon_c''}} \tag{3.36}$$

where $\epsilon_c = \epsilon_c' - j\epsilon_c''$ is the complex permittivity of the conductor, and $\hat{\mathbf{n}}$ is the normal unit vector.

Since FEM with finite size elements is applicable only to close waveguide problems, its application to the analysis of open waveguides must be adapted to model an open, infinite region. A simple approach is to enclose the waveguide in a large enough fictitious boundary. Then, a zero boundary condition such as Perfect Electric Conductor (PEC) or Perfect Magnetic Conductor (PMC) is applied at the fictitious boundary to define the boundary-value problem uniquely. The drawback of this approach is that for a given accuracy, correct location of the fictitious boundary is unknown, although it can be determined iteratively at the expense of more computational efforts. Also the boundary must be sufficiently far away from the waveguide and the distance between the boundary and the waveguide must be increased as the propagation constant approaches cut-off (for open waveguide structures cut-off is usually defined as $\beta = k_0$ rather than $\beta = 0$ as for closed waveguides [87]). Since the asymptotic dependence of the fields in a transverse plane can be expressed as

$$\mathbf{E}(\rho),\ \mathbf{H}(\rho) \sim \begin{cases} \dfrac{e^{-j\sqrt{k_0^2-\beta^2}\rho}}{\sqrt{\rho}} & \text{for} \quad \beta \leqslant k_0 \\ \dfrac{e^{-\sqrt{\beta^2-k_0^2}\rho}}{\sqrt{\rho}} & \text{for} \quad \beta \geqslant k_0 \end{cases} \tag{3.37}$$

where $\rho = \sqrt{x^2 + z^2}$, the fields decay exponentially when $\beta > k_0$, but propagate to infinity when $\beta < k_0$. Therefore, this approach is suitable only when the propagation characteristics in the guided-wave region is concerned. In the region of $\beta < k_0$, this approach could result in enormous errors since the fictitious PEC or PMC boundary conditions prevents the energy from travelling away from the waveguide,

and completely reflects the incoming wave back into the computational domain. In order to overcome such deficiency, the so-called absorbing boundary conditions have been introduced. The absorbing boundary conditions (ABCs) simulate or replace the infinite space that surrounds a finite computational domain. It should be noted that the solution computed within an ABC is an estimate to the solution that would be computed within the actual infinite domain. Moreover, the ABCs only absorb fields produced by sources located inside the surrounded domain, and they can not be placed outside the ABCs. Over the years, various ABCs from the extrapolation [89] or the radiating boundary [90] to the Perfectly Matched Layer (PML) [91] and the complementary operators method [92] have been developed. Among all ABCs, the PML has been proven to be advantageous in modal analysis [93]-[95], e.g. it can be placed closer to the guide.

Using a mode solver implemented in HFSS, a commercial software based on finite element method [96], a full wave modal analysis was carried out to study the guided modes in a CPS structure enclosed in a PEC shield as shown in Fig. 3.16.

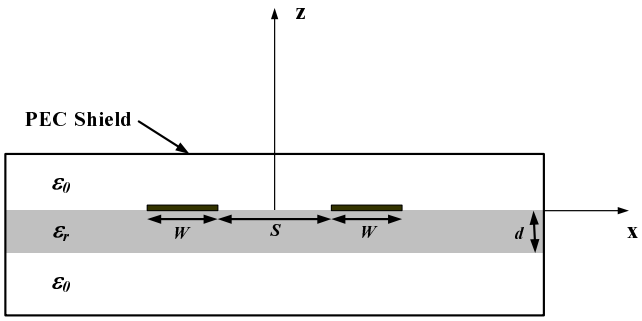

Figure 3.16: The coplanar stripline structure used for modal analysis.

Selecting the physical parameters same as those given in Table 3.7, Fig. 3.17 shows the dispersion diagram for the first three guided modes. Fig. 3.18 illustrates the modal field distribution across the x-z plane.

To make use of PML in modal analysis, COMSOL Multiphysics, a commercial software based on finite element method [97], was deployed. Selecting the physical and geometrical parameters similar to those given in Table 3.8, Fig. 3.19 shows the results obtained from modal analysis.

In Fig. 3.19(a), the normalized propagation constant of the CPS mode is compared with those of surface wave modes. Higher effective index of the CPS mode prevents any power leakage into the surface waves. In Fig. 3.19(b), the total loss due to the metallic, dielectric and radiation losses are shown with respect to the frequency. It should be noted that the metallic loss was dominant at all frequencies.

Table 3.7: CPS parameters

Parameter	Value
Strip width, w	20 μm
CPS gap, s	10 μm
Substrate thickness, d	20 μm
Substrate relative permittivity, ϵ_r	12.9
Fundamental Guiding wavelength at 0.5THz, λ_g	239 μm
Normalized fundamental propagation constant at 0.5THz, $\frac{\beta_1}{k_0}$	2.51
Characteristic impedance at 0.5THz, Z_0	73.7 Ω

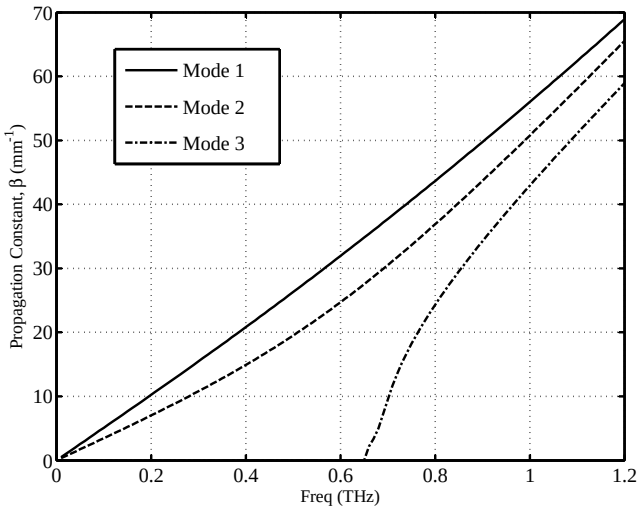

Figure 3.17: Dispersion diagram of the coplanar stripline enclosed in a PEC shield as shown in Fig. 3.16.

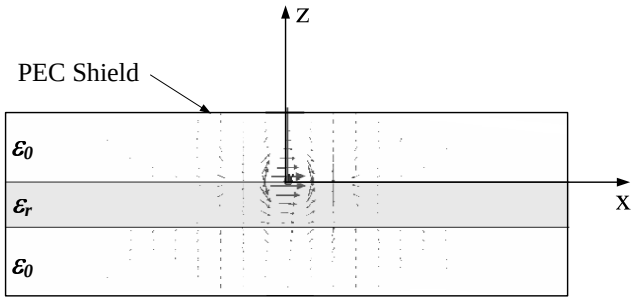

(a)

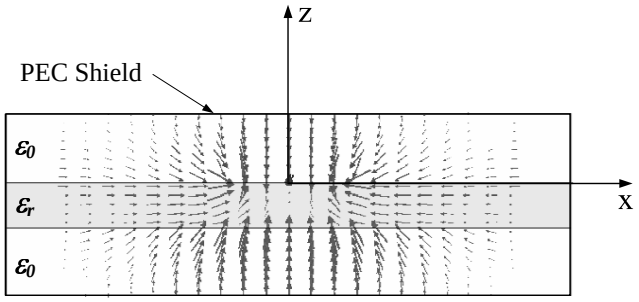

(b)

Figure 3.18: Modal electric field distribution across the x-z plane for the coplanar stripline structure enclosed in PEC (a) mode 1 and (b) mode 2. CPS parameters are given in Table 3.7.

Table 3.8: CPS structure parameters

Parameter	Value
Strip width, w	18.4 μm
CPS gap, s	6.2 μm
Substrate thickness, d	20 μm
Gold strip thickness	0.3 μm
Gold relative permittivity (real part @1THz) [98]	-8.62×10^4
Gold relative permittivity (imaginary part @1THz) [98]	6.23×10^5
SI-GaAs substrate relative permittivity, ϵ_r	12.9
SI-GaAs substrate bulk conductivity	2.38×10^{-7} S/m

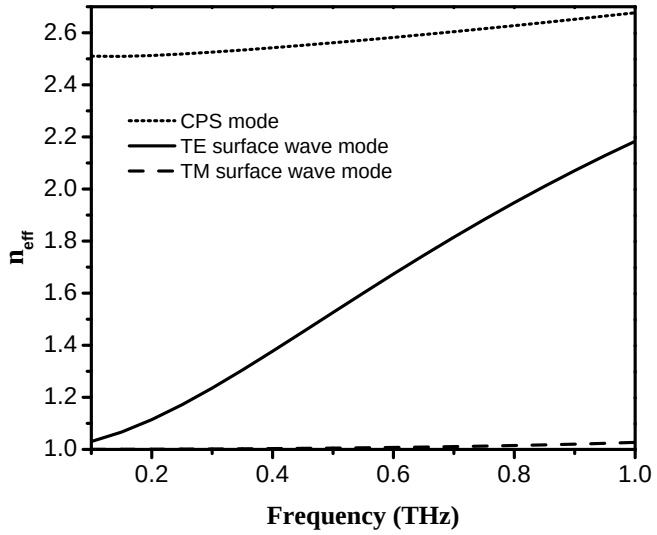

(a)

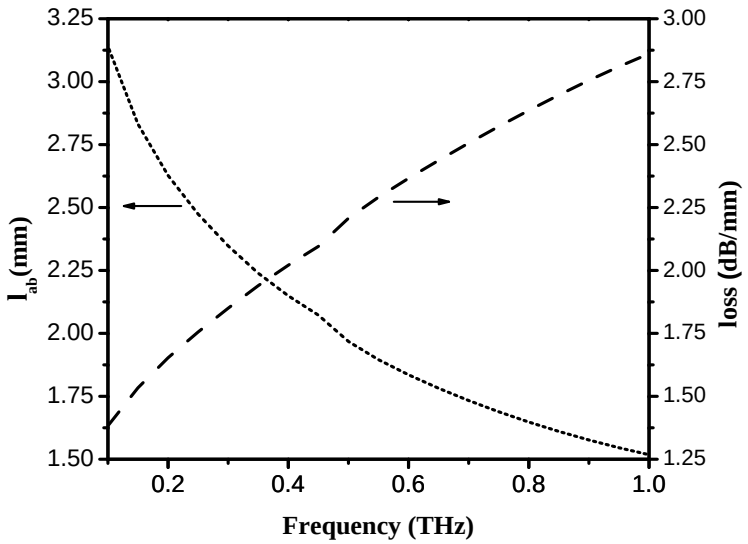

(b)

Figure 3.19: (a) Normalized propagation constant versus frequency for CPS mode (dotted line), TE surface wave mode (solid line) and TM surface wave mode (dashed line). (b) Loss (dashed line) and power absorption length (dotted line). Structure parameters are given in Table 3.8.

Shown also is the power absorption length defined as the length after which the THz power decays by a factor of e^{-1} or 37%.

Modal analysis results obtained in this section will be used in the subsequent sections to calculate the generated THz signal coupled to the CPS.

3.4.2 Calculation of the Generated THz Signal based on Distributed Source Transmission Line

Analysis of traveling-wave photomixers can be addressed through distributed-source transmission line theory [99] and planar transmission line excitation [100] which have been well established in the literature. However, there are very few reports on treating the problem in the question by direct use of this theory. Recently, Pasqualini et al. [61] have addressed some theoretical aspects of the distributed source excitation of CPW on thin membranes applicable to traveling-wave photomixers.

In this subsection, a semi-analytical approach [101] based on distributed-source transmission line theory is proposed to calculate the coupled terahertz signal into a CPS transmission line integrated with a terahertz photomixer source. The proposed method is general, and can be used to design and optimize traveling-wave THz photomixers integrated with planar quasi-TEM guiding structures.

Distributed Source Transmission Line Model

The schematic of the traveling-wave photomixer shown in Fig. 3.1 is considered in the following discussion. Generated traveling-wave photocurrent inside the thin photoabsorbing layer can be modeled, in its general form, as a current sheet at $z = 0$ flowing in the direction of the DC bias electric field [57], i.e. x-direction in Fig. 3.1. In the case of a vertically coupled photomixer the generated terahertz photocurrent can be written as

$$\mathbf{J}(\mathbf{r}) = J(x,y)\delta(z)\exp(-jK_y y)\hat{x} \tag{3.38}$$

$$J(x,y) = I_0(x,y)\frac{e}{\hbar\omega_{opt}}\times \left[\frac{\tau_n v_n}{\sqrt{1+(\omega\tau_n)^2}} + \frac{\tau_p v_p}{\sqrt{1+(\omega\tau_p)^2}}\right] \tag{3.39}$$

$$K_y = \frac{2\omega_{opt}}{c}\sin(\frac{\theta}{2}) \tag{3.40}$$

where $\mathbf{J}(\mathbf{r})$ denotes the photocurrent density inside the thin photoabsorbing layer, ω_{opt} is the average optical angular frequency, c is the speed of light, θ is the angle between two vertically illuminating optical beams, $I_0(x, y)$ is the optical intensity distribution, e is the electron charge, $\hbar\omega_{opt}$ is the optical photon energy, τ_n and τ_p are the photocarrier recombination life time, v_n and v_p are the photocarrier drift velocity, and ω is the THz angular frequency. In the case of an edge coupled photomixer the generated terahertz photocurrent can be represented in the same form as given in (3.38) in terms of the parameters of the guided optical waves [63].

In a high efficient design, most of the generated THz power is coupled into the guiding quasi-TEM mode of the CPS where surface modes and radiation modes are negligible. This condition allows to apply transmission line theory, and obtain fairly accurate results. To study the induced voltage and current along the CPS, we consider the distributed-source transmission line model. Adopting the method discussed in [102] for the current problem, one can derive the canonical form of the transmission line equations for the induced voltage, $V(y)$, and current, $I(y)$, along the CPS as

$$\frac{dV(y)}{dy} = -\gamma(\omega)Z_0(\omega)I(y) - v_s(y) \tag{3.41}$$

$$\frac{dI(y)}{dy} = -\gamma(\omega)Y_0(\omega)V(y) \tag{3.42}$$

$$Z_0(\omega) = \frac{1}{Y_0(\omega)} \tag{3.43}$$

$$\gamma(\omega) = \alpha(\omega) + j\beta(\omega) \tag{3.44}$$

where $v_s(y)$ denotes the distributed voltage source, Z_0 and Y_0 are the characteristic impedance and admittance of the CPS, respectively, γ is the complex propagation constant whose real part, $\alpha(\omega)$, denotes the attenuation constant and its imaginary part, $\beta(\omega)$, represents the phase constant of the quasi-TEM mode of the CPS, and ω is the terahertz angular frequency.

The induced voltage and current along the CPS are obtained by solving the distributed-source transmission-line equations in (3.41) and (3.42) where $v_s(y)$ represents the distributed source term, and is related to the *incident* electromagnetic field. The incident field, $(\mathbf{E}^i, \mathbf{H}^i)$, is defined as the field excited by the impressed photocurrent, given in (3.38), in the presence of the dielectric slab and in the absence of the metallic strips. The relation between the distributed voltage source, $v_s(y)$, and the incident magnetic field is given by

$$v_s(y) = -j\omega\mu \int_{-\frac{s}{2}}^{+\frac{s}{2}} \mathbf{H}^i(x, y, 0) \cdot \hat{z} dx \tag{3.45}$$

where the integrand in (3.45) is the z component of the incident field at $z = 0$, and μ is the permeability of the medium. In fact, $v_s(y)$ in (3.45) describes the electromotive force (emf) induced along the unit length of the CPS due to the time variation of the incident magnetic flux at any given y coordinate.

Evaluation of the Distributed Voltage Source

For evaluation of the distributed source term, $v_s(y)$, it is necessary to determine the incident field. For this purpose, we use spectral domain method which is more convenient in the analysis of planar multilayer structures.

Considering a planar layered medium which is transversely unbounded with respect to z axis, and each layer is homogeneous and isotropic, it is possible to utilize 2-D Fourier transform to convert any field component in the spatial domain (x, y) into its corresponding component in the spectral domain (k_x, k_y). The benefit of this transformation is that Green's functions for the field can be represented in closed-form expressions in the spectral domain [103]. The spatial domain Green's functions are then expressed as Sommerfeld integrals, that are inverse Hankel transform of the corresponding spectral domain Green's functions, and are time-consuming to evaluate. To accelerate the numerical evaluation of the Sommerfeld integrals, the complex image method [104, 105] can be applied. In this method, the Sommerfeld integral is transformed to a series of complex exponentials which is numerically very fast to calculate.

To illustrate the aforementioned technique, consider the vertically coupled configuration in Fig. 3.1(b). The structure is a dielectric slab with permittivity of ϵ_1 and thickness of d. Above and bellow the slab are assumed to be free space with permittivity of ϵ_0. The incident field is produced by the photocurrent impressed on the upper slab/free-space interface when the metal strips are removed. For this geometry the spectral domain Green's function for the magnetic vector potential can be written as

$$G_A^{xx} = \frac{1}{j2k_{z1}}[e^{-jk_{z1}|z|} + Be^{+jk_{z1}z} + De^{-jk_{z1}z}]; \quad -d \leq z \leq 0 \tag{3.46}$$

where G_A^{xx} denotes the x component of the potential vector field due to an x-directed electric dipole source, $k_{z1} = [\epsilon_1 k_0^2 - k_x^2 - k_y^2]^{\frac{1}{2}}$ is the phase constant along the z-

direction in the slab, B and D are constant coefficients obtained from boundary conditions at the interfaces [106].

$$B = R_{TE}\frac{1 + R_{TE}e^{-j2k_{z1}d}}{M} \tag{3.47}$$

$$D = R_{TE}e^{-j2k_{z1}d}\frac{1 + R_{TE}}{M} \tag{3.48}$$

$$M = 1 - R_{TE}^2 e^{-j2k_{z1}d} \tag{3.49}$$

$$R_{TE} = \frac{k_{z1} - k_{z0}}{k_{z1} + k_{z0}} \tag{3.50}$$

The spectral domain Green's function given in (3.46) is transformed into spatial domain through Sommerfeld integral [105]. Applying complex image method, one can represent the spatial domain Green's function with a series of complex exponentials in a closed-form expression as

$$G_A^{xx}(\mid \boldsymbol{\rho} - \boldsymbol{\rho'} \mid) = \frac{1}{4\pi}\frac{e^{-jk_1|\boldsymbol{\rho}-\boldsymbol{\rho'}|}}{\mid \boldsymbol{\rho} - \boldsymbol{\rho'} \mid} + \frac{1}{4\pi}\sum_{k=1}^{N_{ci}} b_k \frac{e^{-jk_1 r_k}}{r_k} \tag{3.51}$$

$$r_k = \sqrt{\mid \boldsymbol{\rho} - \boldsymbol{\rho'} \mid^2 - \beta_k^2} \tag{3.52}$$

where $\boldsymbol{\rho}$ and $\boldsymbol{\rho'}$ are the observation and the source points at $z = 0$ interface, respectively, k_1 is the wave number inside the slab, N_{ci} is the number of complex images required to reconstruct the Green's function, b_k and β_k are complex constants obtained through the method explained in [104]. Usually a few number of complex image terms is enough to give accurate results.

To find the distributed source term, from (3.45), it is only required to evaluate the $\mathbf{H}_z^i$ component of the incident field at $z = 0$ interface as

$$\mathbf{H}_z^i(\boldsymbol{\rho}, z = 0) = -\frac{\partial}{\partial y}\int_{source} G_A^{xx}(\mid \boldsymbol{\rho} - \boldsymbol{\rho'} \mid) J_x(\boldsymbol{\rho'}) d\boldsymbol{\rho'} \tag{3.53}$$

where $J_x(.)$ is the impressed current given in (3.38).

Solving Transmission Line Equations Excited by a Distributed Source

Once the distributed voltage source in (3.45) is determined, the solution to the transmission line equations in (3.41) and (3.42) can be obtained from the superpo-

sition integrals using one dimensional Green's functions of the transmission line.

$$V(y) = \int_{y_1}^{y_2} V_V(y; y') v_s(y') dy' \tag{3.54}$$

$$I(y) = \int_{y_1}^{y_2} I_V(y; y') v_s(y') dy' \tag{3.55}$$

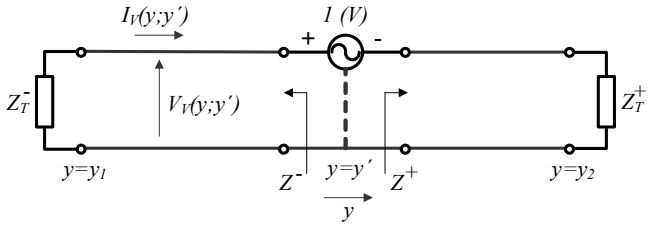

Figure 3.20: General representation of a transmission line loaded at the end points y_1 and y_2, and excited by a voltage point source located at y'.

where $V(y)$ and $I(y)$ are the induced voltage and current along the CPS transmission line, respectively. $V_V(y; y')$ and $I_V(y; y')$ are one dimentional voltage and current Green's functions defined as the response of the circuit shown in Fig. 3.20 when excited by a voltage point source located at $y = y'$. In Fig. 3.20, Z_T^- and Z_T^+ are the arbitrary terminating impedances at the end points y_1 and y_2, respectively, and Z_0 and γ are the characteristic impedance and propagation constant of the line. A detailed approach for finding the response of a general transmission line network shown in Fig. 3.20 has been given in [103]. For the sake of completeness, only the final results are repeated here.

For $y > y'$,

$$V_V(y; y') = -\frac{1}{2} \frac{Z^+(y') + Z_0}{Z^+(y') + Z^-(y')} \times \left[e^{-\gamma(y-y')} + \Gamma^+(y') e^{+\gamma(y-y')} \right] \tag{3.56}$$

$$I_V(y; y') = -\frac{Y_0}{2} \frac{Z^+(y') + Z_0}{Z^+(y') + Z^-(y')} \times \left[e^{-\gamma(y-y')} - \Gamma^+(y') e^{+\gamma(y-y')} \right] \tag{3.57}$$

while for $y < y'$,

$$V_V(y;y') = +\frac{1}{2}\frac{Z^-(y')+Z_0}{Z^+(y')+Z^-(y')}\times \left[e^{+\gamma(y-y')}+\Gamma^-(y')e^{-\gamma(y-y')}\right] \tag{3.58}$$

$$I_V(y;y') = -\frac{Y_0}{2}\frac{Z^-(y')+Z_0}{Z^+(y')+Z^-(y')}\times \left[e^{+\gamma(y-y')}-\Gamma^-(y')e^{-\gamma(y-y')}\right] \tag{3.59}$$

where $Z^+(y')$ and $Z^-(y')$ are the impedances when looking to the right and to the left, respectively, from the source terminals (Fig. 3.20). The reflection coefficients $\Gamma^+(y')$ and $\Gamma^-(y')$ looking to the right and left, respectively, are obtained in terms of the corresponding impedances $Z^+(y')$ and $Z^-(y')$ as

$$\Gamma^+(y') = \frac{Z^+(y')-Z_0}{Z^+(y')+Z_0} \tag{3.60}$$

$$\Gamma^-(y') = \frac{Z^-(y')-Z_0}{Z^-(y')+Z_0} \tag{3.61}$$

Results given in (3.56)-(3.59) are general solutions of a transmission line problem excited by a point source. For special cases, e.g. matched transmission line for which $Z_T^+ = Z_T^- = Z_0$, appreciable simplification is achieved. One dimensional Green's functions for the matched transmission line are reduced to

$$V_V(y;y') = -\frac{1}{2}\mathrm{sgn}(y-y')\exp(-\gamma|y-y'|) \tag{3.62}$$

$$I_V(y;y') = -\frac{Y_0}{2}\exp(-\gamma|y-y'|) \tag{3.63}$$

where $\mathrm{sgn}(\cdot)$ represents the sign function.

Results and Discussion

To study the accuracy of the results obtained from the proposed method, they were compared with those obtained from full wave analysis using HFSS. Selecting the physical parameters similar to those given in Table 3.7, the propagation constant, β, of the CPS can be extracted from Fig. 3.17 at the desired operating frequency. From modal field distribution shown in Fig. 3.18(a), mode 1 represents the quasi-TEM mode of the CPS with odd symmetry. It has a linear dispersion relation with

cut-off frequency of zero. It is the desirable mode to be excited by the impressed photocurrent. As shown in Fig. 3.18(b), mode 2 is very similar to the even mode of the CPS. This mode is not excited by the photocurrent given in (3.38), since the mode field is perpendicular to the exciting current density [107]. Mode 3 and other higher order modes will not be excited as long as the operating frequency is less than their cut-off frequencies. Conclusively, the modal analysis shows that the dominant mode excited at the operating frequency of 0.5 THz for the designed structure is quasi-TEM mode of the CPS with odd symmetry. It should be noted that radiation is not included in the previous modal analysis as the CPS was enclosed in a PEC shield. The radiation effect will be investigated later in this section.

When the laser beams are focused on a small spot in the vertically coupled configuration, the generated photocurrent can be modeled as a dipole current source, $\mathbf{J}(\mathbf{r}) = J_0\delta(x)\delta(y)\delta(z)\hat{x}$, as shown in Fig. 3.21. In Fig. 3.22, the incident field calculated from complex image method, using (3.53), is compared with the result obtained from finite element method, using HFSS, with the observation points on the y axis. As mentioned before, the incident field is calculated when the metal strips are removed. As seen in Fig. 3.22, the result from complex image method is in a good agreement with those obtained from finite element method. For this plot only 5 complex images were considered for the summation in (3.51) ($N_{ci} = 5$).

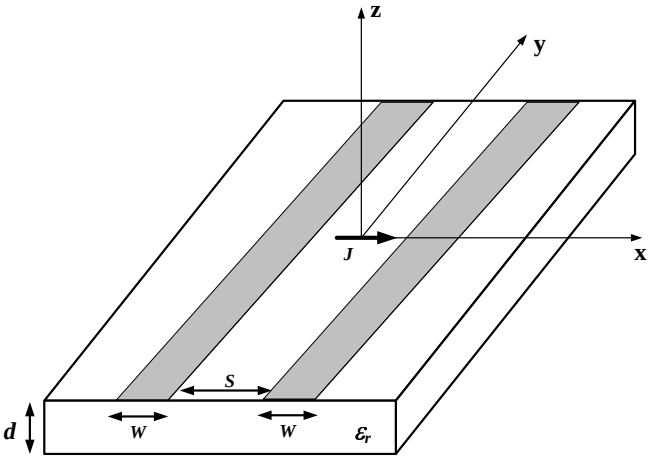

Figure 3.21: Vertically coupled configuration excited by a dipole current source at the origin.

Fig. 3.23 shows the induced voltage along the CPS transmission line obtained from (3.54) when the CPS is excited by the dipole current source at 500 GHz located at the origin. The CPS transmission line extends from $y_1 = -1.25\lambda_g$ to $y_2 = +1.25\lambda_g$ where λ_g is the guiding wavelength. It is assumed that the CPS is terminated to its

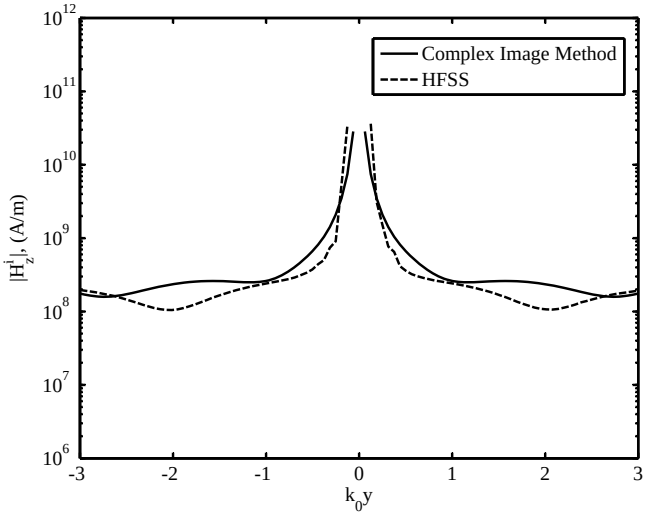

Figure 3.22: Magnitude of the incident field for the vertically coupled configuration shown in Fig 3.21 when excited by a dipole current source at the origin.

characteristic impedance at both ends to avoid standing wave effect, however, any terminating impedance can be easily accommodated using general results given in (3.56)-(3.59). In Fig. 3.23, the results from the proposed method are verified by the full wave analysis using HFSS. While the accuracy is kept the same as the finite element method, the computation time and memory usage are reduced significantly in the proposed method.

Once the induced voltage along the CPS is known, the delivered power to each terminating impedance can be easily calculated, e.g.

$$P(y_2) = \frac{1}{2}\left|\frac{V(y_2)}{Z_T^+}\right|^2 Re\Big\{Z_T^+\Big\} \tag{3.64}$$

where $P(y_2)$ is the average power delivered to Z_T^+ and $V(y_2)$ is the induced voltage at y_2 where the terminating impedance is located, and $Re\{.\}$ represents the real part.

To compare the guided power delivered to the terminating loads with the total radiation power, we enclosed the structure shown in Fig. 3.21 in an air box with radiation boundary condition and let HFSS to calculate the total radiated power. The result showed that the radiated power is less than one percent of the guided power for the designed structure. It suggests that with a proper design most of the power will be coupled into the CPS line.

In the next example, we applied the proposed method to treat a distributed impressed current source problem. Fig. 3.24 shows the induced voltage along

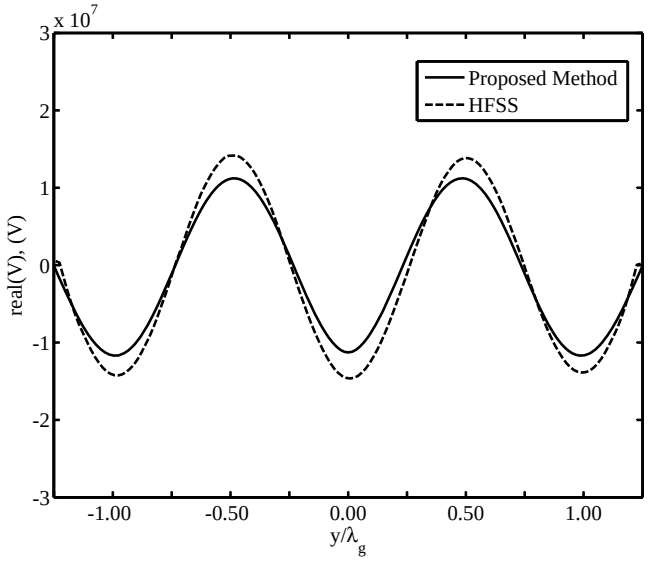

(a)

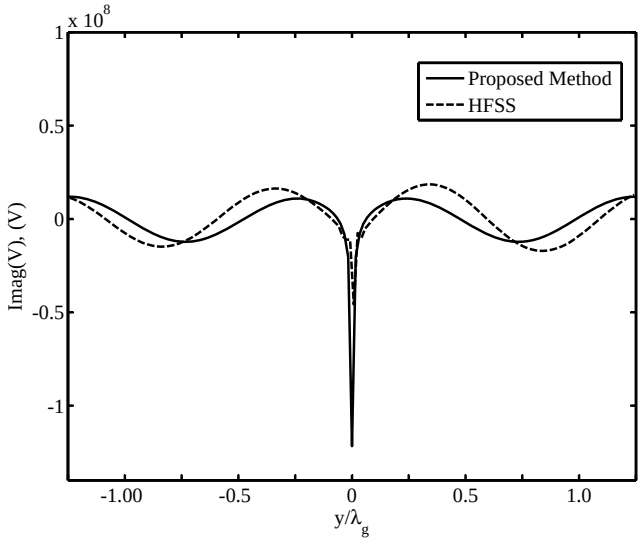

(b)

Figure 3.23: (a) real and (b) imaginary part of the induced voltage along the CPS transmission line shown in Fig. 3.21 excited by a dipole current source at 500 GHz. The result of the proposed method (solid line) is compared with full wave analysis (dashed line).

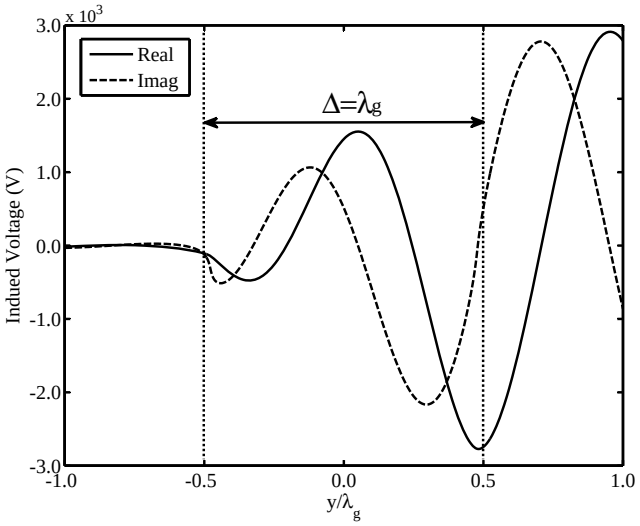

(a)

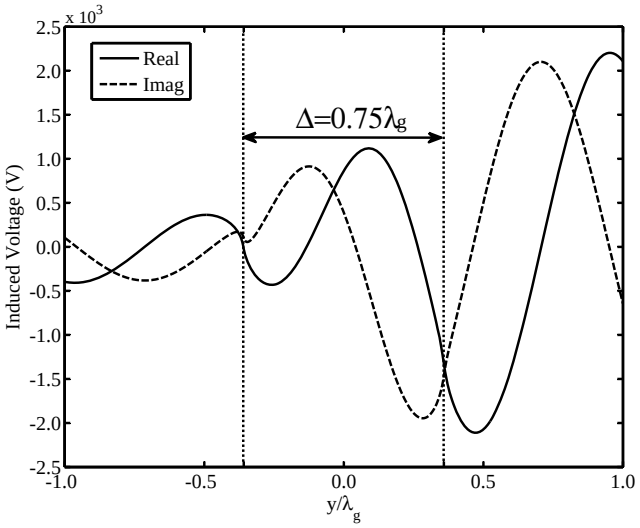

(b)

Figure 3.24: Real and imaginary part of the induced voltage along the CPS transmission line excited by a traveling-wave line current, $\mathbf{J}(\mathbf{r}) = \delta(x)rect(\frac{y}{\Delta})\delta(z)\exp(-jK_y y)\hat{x}$, at 500 GHz for two different photoabsorbing length (a) $\Delta = \lambda_g$ (b) $\Delta = 0.75\lambda_g$.

the CPS transmission line obtained from (3.54) when the CPS is excited by a traveling-wave line current source, $\mathbf{J}(\mathbf{r}) = J_0\delta(x)rect(\frac{y}{\Delta})\delta(z)\exp(-jK_y y)\hat{x}$, at 500 GHz. The CPS transmission line extends from $y_1 = -\lambda_g$ to $y_2 = +\lambda_g$ while the photoabsorbing layer extends from $y = -0.5\Delta$ to $y = +0.5\Delta$. It is assumed that the CPS is terminated to its characteristic impedance at both ends, and the phase velocity of the current is equal to that of the quasi-TEM guided mode of the CPS. In practice, this condition can be achieved by adjusting the angle θ in (3.40) such that $K_y = \beta$ is satisfied. It has been shown that under phase-matched condition the coupled THz power to the transmission line is maximum [108]. As seen in Fig. 3.24, unlike the dipole excitation where the signal is equally distributed in the forward and backward directions (Fig. 3.23), the coupled signal increases in the forward direction. It is noted that in Fig. 3.24(a), where the photoconductive length, Δ, is equal to λ_g, no signal is coupled to the backward direction. However, in Fig. 3.24(b), where the photoconductive length, Δ, is equal to $0.75\lambda_g$, some signal is coupled to the backward direction. This observation is consistent with the general fact reported in [61] where if the length of the photoconductive area is an integer multiple of the half guiding wavelength, no power is coupled to the backward direction. This fact can be used as a design guide when the backward coupling is not desirable.

3.4.3 Calculation of the Generated THz Signal based on Lorentz Reciprocity Theorem

In this subsection, we apply an alternative method to find the field radiated by an arbitrary impressed photocurrent distribution in an open guide, i.e. CPS. In this rigorous method, the radiated field is expanded in terms of a suitable set of orthogonal modes where the expansion coefficients are determined by applying the Lorentz reciprocity theorem. This approach has been applied to the classic problem of the excitation of modes by a probe in closed cylindrical waveguides [107], and here it is extended to be used for open waveguides.

Unlike closed waveguides that comprise an infinite, numerable spectrum of discrete modes, open waveguides comprise a few discrete (guided) modes and besides a continuous (radiative) spectrum [109]. It is possible to apply reciprocity to an open waveguide as long as the mode of interest is confined and mode orthogonality can still be applied, which is usually the case if one chooses the expansion modes (discrete and continuous) properly.

With reference to Fig. 3.25, let $\mathbf{J}(\mathbf{r})$ represents an arbitrary current distribution in an open waveguide, e.g. it could be the generated photocurrent in a MSM photomixer integrated with a CPS guide as shown in Fig. 3.9.

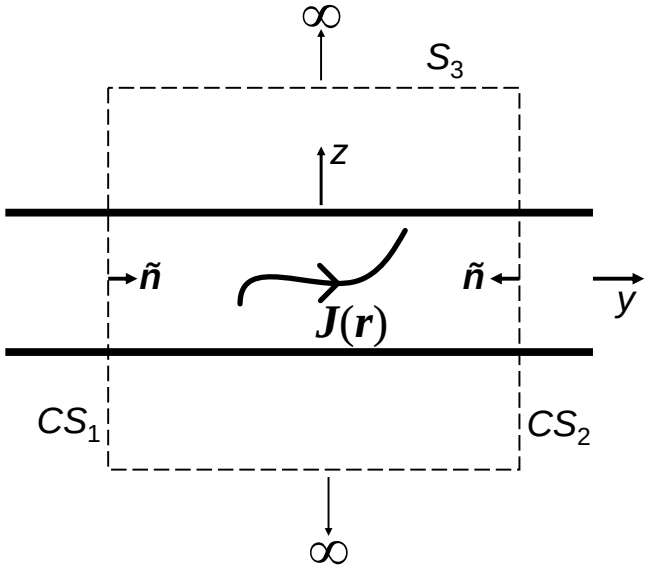

Figure 3.25: An arbitrary current distribution in an open waveguide.

Fields for the n^{th} guided mode propagating in the positive y direction are represented as follows

$$\mathbf{E}_n^+ = (\mathbf{e}_n + \mathbf{e}_{yn})e^{-\gamma_n y} \tag{3.65a}$$

$$\mathbf{H}_n^+ = (\mathbf{h}_n + \mathbf{h}_{yn})e^{-\gamma_n y} \tag{3.65b}$$

and for propagation along the negative y direction, the fields are then given by

$$\mathbf{E}_n^- = (\mathbf{e}_n - \mathbf{e}_{yn})e^{\gamma_n y} \tag{3.66a}$$

$$\mathbf{H}_n^- = (-\mathbf{h}_n + \mathbf{h}_{yn})e^{\gamma_n y} \tag{3.66b}$$

In (3.65) and (3.66), $\mathbf{e}_n$ and $\mathbf{h}_n$ are transverse vector eigenfunctions dependent on the transverse coordinates, i.e. (x,z), whereas $\mathbf{e}_{yn}$ and $\mathbf{h}_{yn}$ are longitudinal vector functions of the transverse coordinates. Discrete eigenfunctions are mutually orthonormal over the guide cross section CS, so that

$$\iint_{CS} \mathbf{e}_m \times \mathbf{h}_n \cdot \hat{\mathbf{y}} \mathrm{d}S = \delta_{mn} \tag{3.67}$$

where δ_{mn} represents the Kronecker delta function. The above orthogonal property is also valid for degenerate modes [107].

The response of the guide to a source involves excitation of the discrete (guided) modes of the CPS as well as of a continuum of modes which radiate transversally, and either propagate, or are evanescent along the guide axis y. Such continuous modes can be seen as wave packets in k_x [109], where each packet corresponding to a fixed value of k_t which individually satisfy boundary and edge conditions on the strips, radiation at infinity, and continuity of the tangential fields at the interfaces between dielectrics.

For a given k_t, there is still the possibility of degeneracy, that is the existence of a number of different strip currents and field configurations satisfying all boundary and edge conditions, pertaining to the same value of k_t, which are labeled by the discrete index μ.

It can be shown that wave packets corresponding to different values of k_t and of the discrete index μ are mutually orthonormal over the cross section [78], as defined below

$$\iint_{CS} \mathbf{e}_\mu(k_t) \times \mathbf{h}_\nu(k_t') \cdot \hat{\mathbf{y}} \mathrm{d}S = \delta_{\mu\nu}\delta(k_t - k_t') \tag{3.68}$$

where $k_t^2 = k_0^2 - \beta^2$ and $0 < k_t < \infty$. The orthogonality relation also exists between guided and radiative modes. Beside orthogonality, the completeness of the combined discrete and continuos spectra of an open waveguide has been proven in [78, Ch.7]. Therefore, any field radiated in the positive y direction by the impressed current distribution can be expanded in terms of discrete and continuos eigenmodes as

$$\mathbf{E}^+(\mathbf{r}) = \sum_n a_n \mathbf{E}_n^+(\mathbf{r}) + \int_0^\infty \sum_\mu a_\mu(k_t)\mathbf{E}_\mu^+(\mathbf{r}; k_t)\mathrm{d}k_t \tag{3.69a}$$

$$\mathbf{H}^+(\mathbf{r}) = \sum_n a_n \mathbf{H}_n^+(\mathbf{r}) + \int_0^\infty \sum_\mu a_\mu(k_t)\mathbf{H}_\mu^+(\mathbf{r}; k_t)\mathrm{d}k_t \tag{3.69b}$$

and the field radiated in the negative y direction can be represented by

$$\mathbf{E}^{-}(\mathbf{r}) = \sum_{n} b_n \mathbf{E}_n^{-}(\mathbf{r}) + \int_0^{\infty} \sum_{\mu} b_\mu(k_t) \mathbf{E}_\mu^{-}(\mathbf{r}; k_t) \mathrm{d}k_t \tag{3.70a}$$

$$\mathbf{H}^{-}(\mathbf{r}) = \sum_{n} b_n \mathbf{H}_n^{-}(\mathbf{r}) + \int_0^{\infty} \sum_{\mu} b_\mu(k_t) \mathbf{H}_\mu^{-}(\mathbf{r}; k_t) \mathrm{d}k_t \tag{3.70b}$$

In particular, the expansion (3.69) gives the radiated field on the cross-sectional plane CS_2, whereas (3.70) gives the radiated field on CS_1 as shown in Fig. 3.25.

From Lorentz reciprocity theorem [107]

$$\oiint_S (\mathbf{E}_n^{\pm} \times \mathbf{H} - \mathbf{E} \times \mathbf{H}_n^{\pm}) \cdot \hat{\mathbf{n}} \, \mathrm{d}S = \iiint \mathbf{J} \cdot \mathbf{E}_n^{\pm} \, \mathrm{d}V \tag{3.71}$$

where $\mathbf{E}$ and $\mathbf{H}$ are the total fields radiated by the current $\mathbf{J}$, surface S encloses the current distribution $\mathbf{J}$, and $\hat{\mathbf{n}}$ has been chosen as the inward-directed normal to S. We now choose the surface S composed of the two cross-sectional planes CS_1 and CS_2, and a cylindrical side wall which expands to infinity as in Fig. 3.25. There is no contribution to the surface integral arising from the side wall since guided modal fields $\mathbf{E}_n^{\pm}$ and $\mathbf{H}_n^{\pm}$ are exponentially decaying as seen from their asymptotic behaviour given in (3.37), and they become zero on the side wall which is located at transversally far away distance. When the expansion (3.69) and (3.70) for $\mathbf{E}$ and $\mathbf{H}$ on the cross sections are used along with mode orthogonality, the left-hand side integral in (3.71) is readily calculated as

$$\iint_{CS_1} (\mathbf{E}_n^{+} \times \mathbf{H} - \mathbf{E} \times \mathbf{H}_n^{+}) \cdot \hat{\mathbf{y}} \, \mathrm{d}S = -2b_n \tag{3.72a}$$

$$\iint_{CS_2} (\mathbf{E}_n^{+} \times \mathbf{H} - \mathbf{E} \times \mathbf{H}_n^{+}) \cdot (-\hat{\mathbf{y}}) \, \mathrm{d}S = 0 \tag{3.72b}$$

$$\iint_{CS_1} (\mathbf{E}_n^{-} \times \mathbf{H} - \mathbf{E} \times \mathbf{H}_n^{-}) \cdot \hat{\mathbf{y}} \, \mathrm{d}S = 0 \tag{3.72c}$$

$$\iint_{CS_2} (\mathbf{E}_n^{-} \times \mathbf{H} - \mathbf{E} \times \mathbf{H}_n^{-}) \cdot (-\hat{\mathbf{y}}) \, \mathrm{d}S = -2a_n \tag{3.72d}$$

Therefore, by substituting (3.72) in (3.71), the amplitudes of the forward, a_n, and backward, b_n, propagating waves of the n^{th} guided mode outside the active region are obtained as

$$a_n = -\frac{1}{2}\iiint \mathbf{J}(\mathbf{r}) \cdot \mathbf{E}_n^-(\mathbf{r})\ \mathrm{d}V \tag{3.73a}$$

$$b_n = -\frac{1}{2}\iiint \mathbf{J}(\mathbf{r}) \cdot \mathbf{E}_n^+(\mathbf{r})\ \mathrm{d}V \tag{3.73b}$$

It should be noted that in (3.73), $\mathbf{E}_n^{\pm}(\mathbf{r})$ is the modal field of interest which is obtained from the modal analysis discussed in Section 3.4.1, and also the integration is performed on the volume where the current $\mathbf{J}(\mathbf{r})$ is distributed.

Results and Discussion

The travelling-wave photocurrent and fundamental quasi-TEM mode of the CPS inside the active region can be expressed as

$$\mathbf{J}(\mathbf{r}) = \boldsymbol{J}_{THz}(x,z)e^{-\alpha_e y}\ e^{j(\omega_{THz}t - K_y y)} \tag{3.74a}$$

$$\mathbf{E}_1^+(\mathbf{r}) = \mathbf{e}_1(x,z)e^{-j\beta y} \tag{3.74b}$$

$$\mathbf{E}_1^-(\mathbf{r}) = \mathbf{e}_1(x,z)e^{+j\beta y} \tag{3.74c}$$

where $\boldsymbol{J}_{THz}(x,z)$ is the cross sectional current distribution obtained in Section 3.3.6, α_e is the effective optical power absorption calculated in Section 3.2, ω_{THz} is the angular difference frequency of two lasers, $K_y = \frac{\omega_{THz}}{c_0} n_{eff}$ is the current phase propagation, $\mathbf{e}_1(x,z)$ and β are the 2-D modal field distribution and propagation constant of the quasi-TEM mode of CPS, respectively, obtained in Section 3.4.1. It should be noted that $\mathbf{e}_1(x,z)$ is normalized according to (3.67). Substituting (3.74) into (3.73), and assuming that the active region is distributed from $y = 0$ to $y = \Delta$, the expansion coefficients of the forward, a_1, and backward, b_1, propagating waves of the quasi-TEM mode of CPS outside the active region are obtained as

$$a_1 = C_a(\beta, K_y)\iint_{CS} \boldsymbol{J}_{THz}(x,z) \cdot \mathbf{e}_1(x,z)\mathrm{d}x\mathrm{d}z \tag{3.75a}$$

$$b_1 = C_b(\beta, K_y)\iint_{CS} \boldsymbol{J}_{THz}(x,z) \cdot \mathbf{e}_1(x,z)\mathrm{d}x\mathrm{d}z \tag{3.75b}$$

where

$$C_a(\beta, K_y) = -\frac{e^{\frac{\gamma_a \Delta}{2}}}{\gamma_a} \sinh(\frac{\gamma_a \Delta}{2}) \tag{3.76a}$$

$$C_b(\beta, K_y) = -\frac{e^{\frac{\gamma_b \Delta}{2}}}{\gamma_b} \sinh(\frac{\gamma_b \Delta}{2}) \tag{3.76b}$$

$$\gamma_a = -\alpha_e - j(K_y - \beta) \tag{3.76c}$$

$$\gamma_b = -\alpha_e - j(K_y + \beta) \tag{3.76d}$$

Shown in Fig. 3.26 are the amplitude of complex coefficients $C_a(\beta, K_y)$ and $C_b(\beta, K_y)$ with respect to the normalized terahertz mode propagation constant. In Fig. 3.26, it is assumed that the optical power absorption coefficient and the effective refractive index are 2300 m^{-1} and $n_{eff} = 3.49562$, respectively, as given in Table 3.4. The beat frequency is 500GHz. From Fig. 3.26(a), it is evident that when phase velocity matching condition, $\beta = K_y$, between the travelling-wave photocurrent and the propagating mode occurs, maximum power is coupled in the forward direction. Moreover, by increasing the active region length Δ up to a maximum length, the peak increases. Any length longer than about four times of the optical absorption length does not effectively increase the terahertz mode power. This is due to the fact that the amplitude of the traveling-wave photocurrent approaches zero value. For the CPS structure parameters given in Table 3.8, the normalized terahertz mode propagation constant is $\frac{\beta}{K_y} = 0.73$ at 500GHz. It is worth to note that this ratio can approach unity by using e.g. slow-wave transmission lines [110] or by confining the terahertz mode entirely in a dielectric waveguide with refractive index close to that of the optical waveguide.

Fig. 3.27 shows the calculated THz mode power coupled in the forward direction, $|a_1|^2$, and backward, $|b_1|^2$. Solid lines are for the case of unmatched phase velocity ($\frac{\beta}{K_y} = 0.73$) whereas dotted lines show the matched phase velocity case ($\frac{\beta}{K_y} = 1$). In Fig. 3.27 other parameters are selected as follow; the optical absorption length $l_{ab} = 434.8\mu$m, total optical power 42mW, optical effective refractive index $n_{eff} = 3.49562$, beat frequency $f = 500$GHz, and $V_{DC} = 40V$. In the unmatched phase velocity case, the forward mode power has a resonance behaviour with respect to the length of the active region. Its peak value happens at a certain length around $\Delta = \frac{\pi}{K_y - \beta}$. In the matched phase velocity case, the forward mode power increases when the active region becomes longer and start to saturate beyond a length of about four times of the optical absorption length. Comparing the graphs in Fig. 3.27(a) reveals that by satisfying phase match condition and

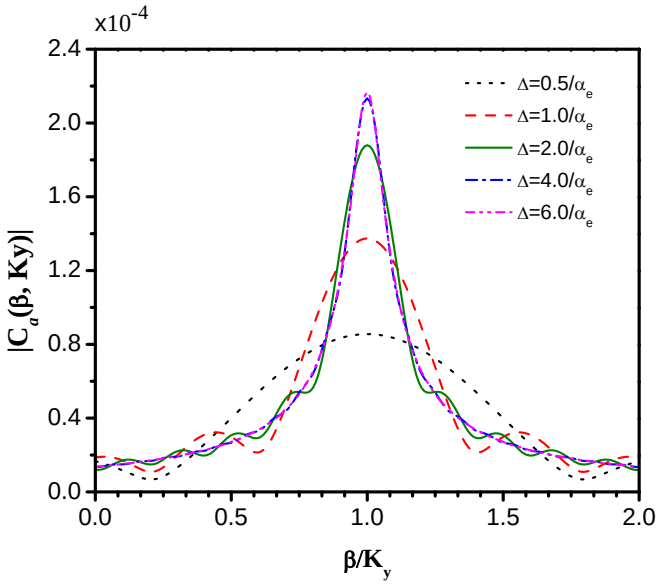

(a)

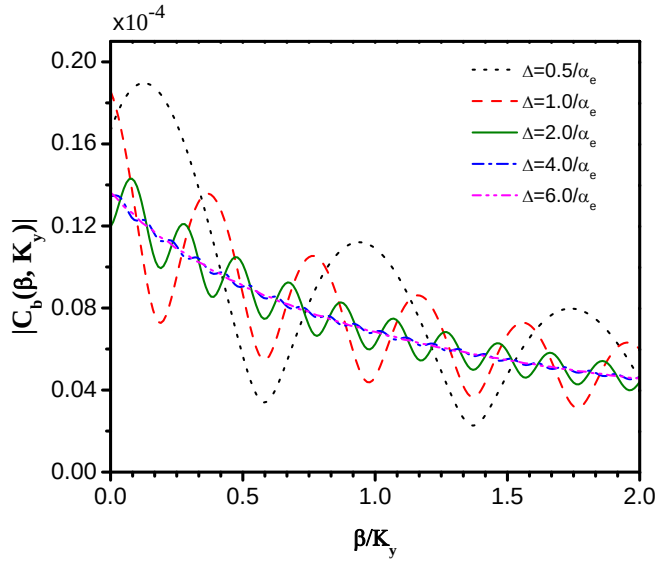

(b)

Figure 3.26: Amplitude of complex coefficient (a) $C_a(\beta, K_y)$ and (b) $C_b(\beta, K_y)$ with respect to the terahertz mode propagation constant. Parameters are the optical absorption length $1/\alpha_e = 434.8\mu$m, optical effective refractive index $n_{eff} = 3.49562$ and beat frequency $f = 500$GHz.

asssuuming the modal field and current distribution does not change, the coupled power will increase by a factor of around 2 for the equal length and by a factor of about 8 for the increased length. Moreover, by comparing Fig. 3.27(a) and 3.27(b), it is evident that the power coupled in the backward direction is negligibly small compared to that coupled in the forward direction.

Fig. 3.28 shows the maximum achievable mode power with respect to frequency for a travelling-wave MSM photomixer illustrated in Fig. 3.9. The optical, semiconductor and electromagnetic parameters used for this simulation are given in Table 3.3, Table 3.6 and Table 3.8, respectively. For the unmatched case, the peak power is selected for the resonance length whereas in the matched case, it is assumed that the active region is long enough to get the maximum power. It should be noted that the calculated values for the level of the generated THz power compares with some of the experimental results reported in the litrature [111].

3.5 Conclusion

Rigorous analysis of CW traveling-wave terahertz photomixers demands for a global approach which includes all the involved physical phenomena. The main aim of this Chapter was to establish such approach by formulating an example structure. Moreover, several advancement have been introduced in the design and analysis of such terahertz sources. For example, a systematic method was proposed for the optical waveguide design. The main design parameter is the optical fill factor of the photoabsorbing region which determines the absorption length and the optimum length of the active region. Moreover, in drif-diffusion model, the trap charge dynamic was included in the formulation to increase the accuracy and to prevent from non-physical net charge creation. Additionally, two methods were proposed for calculating the coupled THz signal into the CPS structure. The proposed semi-analytical method is summarized in three main steps; in the first step, the incident field produced by the impressed photocurrent is found in the absence of the guiding structure. In the next step, the distributed source term in the transmission line representation is calculated from the incident field, and in the final step, the distributed-source transmission line equations are solved by using one-dimensional Green's functions. By representing the total field in terms of the guided and radiated modes, a rigorous method was proposed to find the coupled terahertz power into any desired guided mode. The importance of phase velocity match was studied numerically. Finally, the proposed global analysis approach can be used for opti-

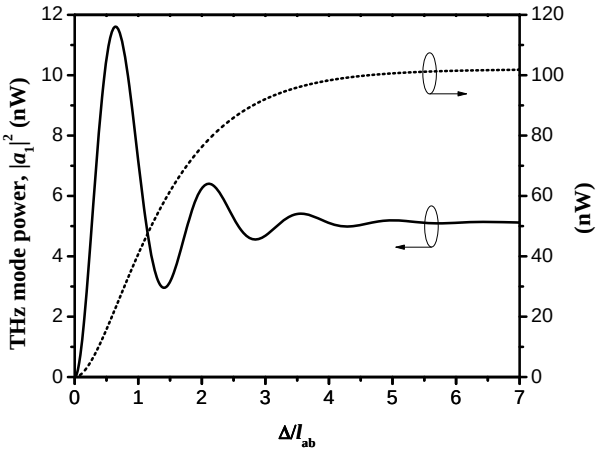

(a)

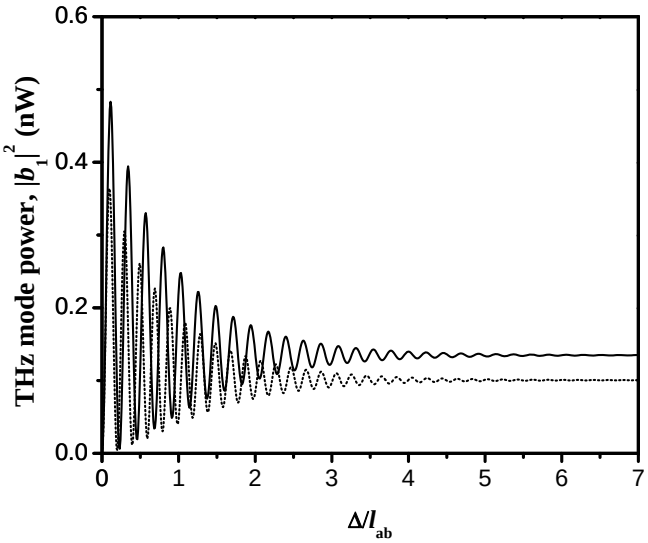

(b)

Figure 3.27: Calculated THz mode power coupled in (a) forward direction and (b) backward direction. Solid lines are for the case of unmatched phase velocity ($\frac{\beta}{K_y} = 0.73$) and dotted lines are for the matched phase velocity ($\frac{\beta}{K_y} = 1$). Parameters are the optical absorption length $l_{ab} = 434.8\mu$m, total optical power 42 mW, optical effective refractive index $n_{eff} = 3.49562$, beat frequency $f = 500$ GHz, and $V_{DC} = 40\ V$.

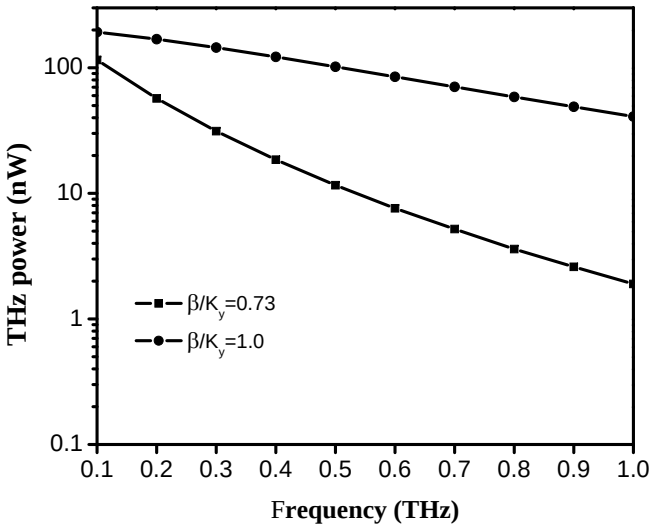

Figure 3.28: Maximum achievable mode power with respect to frequency for a travelling-wave MSM photomixer shown in Fig. 3.9. The optical, semiconductor and electromagnetic parameters used for this simulation are give in Table 3.3, Table 3.6 and Table 3.8, respectively.

mization of both material and geometry in terahertz photoconductive sources for increased optical-to-terahertz power conversion.

Chapter 4

Biochip Sensors Based on Terahertz Photonics

4.1 Introduction

In recent years, THz spectrum has been recognized for new applications in biology and medicine specifically in biosensing [1], biomedical imaging [7], and pharmaceutical screening [8].

THz spectrum is promising for biosensing applications, since many macromolecules such as deoxyribonucleic acid (DNA) and proteins tend to have vibrational modes falling in this range of the electromagnetic spectrum [21]. It has been also reported that hybridized and denatured DNA can be distinguished based on their dielectric property differences, so that research can progress towards the development of label-free DNA chips [112]. Given this unique property of THz range which is not seen in other frequencies, it is expected that the use of biochip sensors based on terahertz technology will grow in near future [112]. Today, e.g. the dominant approach for hybridization detection in DNA molecules is based on fluorescent labeling of the target DNA strand. Although fluorescent labeling has given rise to efficient biosensing systems in some cases [113], it generally suffers from a number of deficiencies; labeling not only constitutes an additional costly and time-consuming preparatory steps, but also introduces modifications in molecular conformation which lowers the precision of the sensing. Therefore, there is a strong interest in developing alternative label-free detection and sensing schemes.

Recent studies on the interaction of THz radiation with biomolecules have shown that it is feasible to sense and distinguish biomolecules from their dielectric prop-

erties in the THz range. Based on this principle, various THz biosensors using resonant structures have been introduced for label free DNA analysis. Nagel and Kurz [114] proposed a corrugated parallel plate resonator-based THz sensor chip for DNA analysis. Using THz pulses, they were able to detect a complementary gene sequence with a length of 28 bases. Baras et al. [115] performed a numerical study on different planar resonator geometries and examined the influence of critical experimental parameters on the transmission characteristics of the resonant structures in THz biosensors. Kato et al. [116] proposed a THz biosensor based on thin metallic mesh structure. Kurt and Citrin [35] studied the propagation of terahertz waves in two-dimensional photonic-crystal waveguides to investigate the effects of introducing small quantities of biomolecules, such as DNA, into selected air holes for sensor applications.

In all these structures, a THz resonator is used as a sample carrier and transducer. When the resonator is loaded by a bio-material, the characteristic parameters of the resonator, such as resonance frequency and quality factor, change in accordance with the refractive index and the attenuation coefficient of the sample. Given the fact that target-probe hybridization state influences the refractive index and the attenuation coefficient of the sample [117], by monitoring and processing the data on resonance characteristic, the hybridization state between target DNA and probe DNA is determined.

Among different kinds of resonators, those with planar structures are more promising for low-cost integrated biosensors, as their fabrication technology is fully compatible with readily available planar integrated circuit technology. Recently, various THz biosensors using metallic planar waveguide structures have been introduced for label-free DNA analysis [30]–[40].

In this Chapter, the aim is to develope a systematic approach based on the fundamental theory laid down in Chapter 3 for modeling and analysis of such THz biosensors described above. We also propose a new continuous-wave integrated THz biosensor device. In the following sections, the structure of the proposed biosensor device is discussed, and the performance of the bio-chip in terms of sensitivity and selectivity is investigated through numerical modeling.

4.2 Biochip Structure

Fig. 4.1 shows the schematic of the proposed THz biochip sensor [120]. It illustrates a single element THz biosensor consisting of three major parts; a THz

traveling-wave photomixer source, a THz resonator which receives the sample, and a THz antenna, all integrated on a single chip. These components are connected to each other through coplanar stripline which is shown as metallic strips in Fig. 4.1. The optical waveguide section is the same as that described before in Fig. 3.4(c).

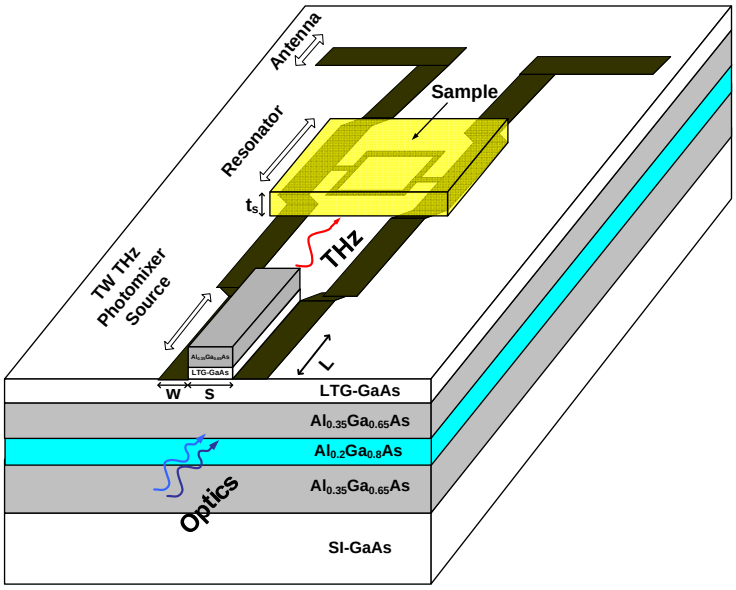

Figure 4.1: Schematic of the proposed THz biochip sensor.

The chip facet is illuminated through free space or by a single mode fiber carrying two detuned lasers with the wavelength around 780nm. The optical waveguide is designed such that most of the optical power is guiding in the slab waveguide while the remaining part is travelling inside the ridge waveguide, and is gradually absorbed in the ultra-fast photoabsorbing layer, i.e. LTG-GaAs. Using two coupled waveguides allows the optical power to be absorbed in a longer distance, and consequently keeps the laser power density bellow the thermal damage threshold of the photo absorbing layer [63].

As previously discussed in Chapter 3, a traveling-wave photocurrent is generated inside the LTG-GaAs layer by beating of the two CW detuned lasers propagating in the ridge waveguide. The generated photocurrent acts as an impressed source to excite a THz signal in the CPS transmission line. The THz signal propagates along the CPS and interacts with the biomolecules placed on top of the planar resonator. After interaction, the THz signal propagates toward the antenna to be detected either on-chip or off-chip. To maximize the generated THz power and enhance the performance of the biochip, the design guides discussed in Chapter 3 should be followed.

4.3 Operation Principle

The operating principle of the proposed THz biochip sensor is based on the resonance perturbation method [107]. Presence of the bio-sample immobilized on top of the resonator surface alters the effective refractive index of the medium surrounding the resonator, and consequently the resonance characteristics, i.e. resonance frequency and quality factor, will change according to the sample dielectric properties. Therefore, those sensing parameters which are linked to the dielectric behaviour of the sample can be extracted through processing of the changes occur in the resonance characteristics.

The resonance characteristics in the proposed device show up in the transmission coefficient of the resonator. The transmission coefficient in the frequency domain is measured by sweeping the wavelength in one of the CW lasers. From the transmission response, the change in the characteristic parameters of the resonator due to the presence of bio-sample is processed to extract information about the refractive index and the attenuation coefficient of the sample under test. In a further step, the dielectric parameters can be used to quantify the sensing parameter of interest.

A significant advantage of using a resonator as transducer is that the volume of the analyte required for a reliable sensing is reduced dramatically by several order of magnitude compared to free-space spectroscopy approach [121]. The reduction in the level of the analyte gives rise to much higher analytic sensitivity for the resonance based biochips. This benefit comes from the fact that electromagnetic field inside the resonator is highly localized, therefore, interaction between field and the sample can take effect in a very small area. However, in free-space spectroscopy, a large amount of bio-material has to be distributed over a large area with a thick thickness to increase the interaction between THz wave and the sample, and also to minimize the diffraction effect at the sample edges. Another advantage of using resonators as transducer is that it increases the throughput of the biosensing system. Arrays of resonators can be implemented on a single chip in order to detect several unknown samples simultaneously.

Using the proposed biochip, one can differentiate e.g. the fragments of single strand DNA (ss-DNA) and double strand DNA (ds-DNA) molecules from their dielectric differences. This capability enables the device to be used for DNA sequencing which is essential in the determination of genome sequence, mutation detection, gene discovery and gene expression [122].

4.4 Design of Coplanar Strip Resonator

Fig. 4.2 illustrates the layout of the proposed planar CPS resonator [123]. This resonator consists of a combination of short- and open-ended T-stubs placed inside and outside of a CPS transmission line, respectively. To place the short ended T-stub between the narrowly spaced CPS strips, the transmission line is widened which corresponds to a small change in the characteristic impedance value. From the design point of view, when the short-ended T-stub length is around $L_{R1} = 0.5\lambda_g$, where λ_g is the wavelength inside the CPS transmission line, this stub acts as a shunt band pass resonator [124]. The open-ended T-stub acting as a band stop resonator is added to enhance the out-of-band rejection in the lower part of the frequency response.

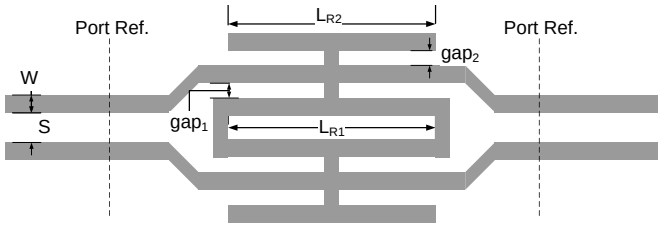

Figure 4.2: Layout of the proposed planar CPS resonator.

The physical dimensions of the CPS transmission line, such as metallic strip width, w, distance between two strips, s, and substrate thickness, d, are chosen such that the quasi-TEM mode becomes the dominant propagating mode along the CPS transmission line at the operating frequency range. Then, the wavelength inside the CPS structure, λ_g, for the dominant mode is obtained from modal analysis as discussed earlier in Section 3.4.1. Finally, the short- and open-ended T-stub lengths, L_{R1} and L_{R2}, are optimized around the half of the guiding wavelength. Selecting $w = 20\ \mu m$, $s = 10\ \mu m$, and $d = 20\ \mu m$, we designed a CPS resonator with resonant frequency of 500 GHz on a GaAs substrate with relative permittivity of $\epsilon_r = 12.9$. Fig. 4.3 compares the simulated frequency response of the unloaded and loaded resonator using HFSS. In the loaded resonator, a 3-μm-thick thin film dielectric covers the resonator on top to mimic the presence of a sample. The refractive index and loss tangent of the thin film are 1.5 and 0.001, respectively, which are in the range of those reported for air-dried amorphous DNA [117].

In the transmission response of the unloaded resonator, shown in Fig. 4.3, the insertion loss of 3.8 dB is observed at the center frequency of 500GHz. The loss can be attributed to the dielectric, metallic and radiation loss which all have been

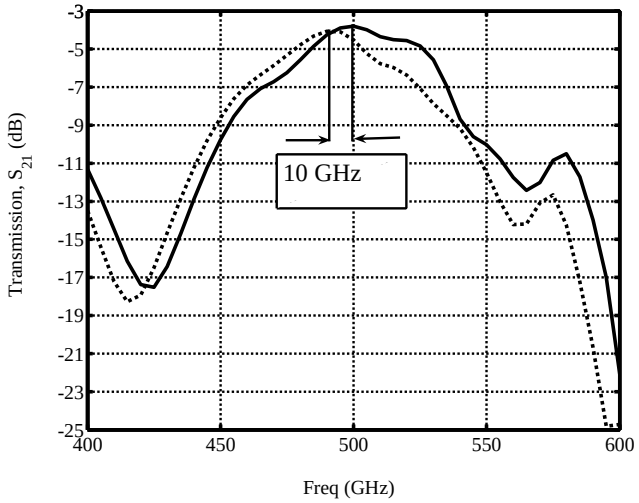

(a)

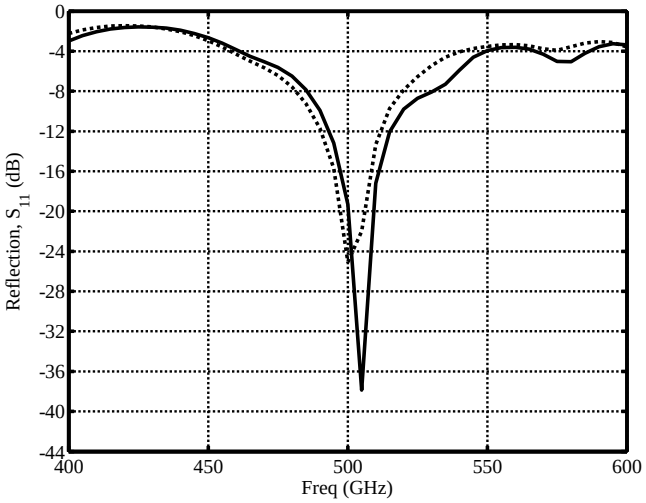

(b)

Figure 4.3: Frequency response of the CPS resonator; unloaded (solid line) and loaded with a 3-μm-thick thin film dielectric with refractive index and loss tangent of 1.5 and 0.001, respectively (dotted line).

included in the full-wave simulation. As shown in Fig. 4.3, a detectable 10 GHz down shift occurs in the resonance frequency after loading the resonator with the thin film sample. Detailed discussion on analyte sensitivity and selectivity is given in Section 4.6.

4.5 Electromagnetic Modeling of Thin Film Biomolecules

In numerical simulation of terahertz DNA biochips, modeling of DNA self-assembled monolayer immobilized on a metallic surface is challenging. Most of the numerical techniques such as finite element method (FEM) fail to give accurate results, when the monolayer is modeled with a thin film dielectric. This failure is due to an extremely large aspect ratio introduced in the biochip structure, since the thickness of the DNA monolayer (in the range of several nanometers) is much smaller than the chip dimensions (in the range of several hundred micrometers). Therefore, using ultra-thin dielectric film to model the bio-layers not only reduces the accuracy, but also requires large amounts of computational resources for the simulation. This is because of the huge number of unknowns introduced in the nodal points of the generated mesh.

To circumvent the aforementioned numerical problem, we propose an alternative approach for modeling the DNA monolayer. Our approach is based on the equivalent surface impedance boundary condition. Using the equivalent surface impedance boundary condition instead of a thin dielectric layer eliminates the mesh generation along the thickness of the layer and consequently makes the simulation faster and more accurate. First order surface impedance boundary condition is investigated in what follows to show whether it can replicate the electromagnetic properties of a DNA monolayer.

To apply the equivalent surface impedance for modeling of DNA monolayer, the structure of a THz biochip sensor experimentally demonstrated in [114] is considered here. The structure is based on parallel plate waveguide components and consists of four separable parts: a THz emitter, a THz detector, a flat metalized silicon chip and a corrugated metalized silicon chip called the biochip. The biochip, on which the probe DNA strands are immobilized, contains a periodic sequence of eight v-grooves with a defect in periodicity in the centre position of the corrugation. This structure generates a narrow transmission band within a broad

stop-band [114] which can be considered as a high Q resonator. The probe-target DNA hybridization can be detected from the change in the resonance frequency.

As reported in [114], the measured values of the shift in the resonance frequency due to the loading of DNA samples on the biochip surface is 5-8 times larger than that obtained from FEM simulation using thin film dielectric model. This discrepancy can most likely have two main reasons; first, the dielectric properties of an ultra thin film of DNA would be different from that of dehydrated amorphous DNA sample as used in the simulations. Second, the FEM simulator fails to give accurate results when the thickness of the dielectric layer is extremely small (in the range of several nanometers) due to an extremely large aspect ratio introduced in the model.

In the new simulation approach for modelling the loaded surface, we replace the functionalized corrugated surface of the biochip by a surface impedance boundary condition $Z_s = R_s + jX_s$ as shown in Fig. 4.4. An unloaded surface is modeled by $Z_s = 0$ which is equivalent to a perfect electrical conductor (PEC) boundary. The functionalized surface can be modeled by a purely reactive surface when the loss is negligible ($R_s \approx 0$). In Fig. 4.4, all the dimensions are the same as those given in [114]. Since the structure is relatively long in y-direction, periodic boundary conditions are used at $y = \pm 120\mu m$ to truncate the computational domain and speed up the simulation. In Fig. 4.4, the field distribution at the input port is shown, using HFSS. As expected, the excited field is similar to the TEM mode of a parallel plate waveguide.

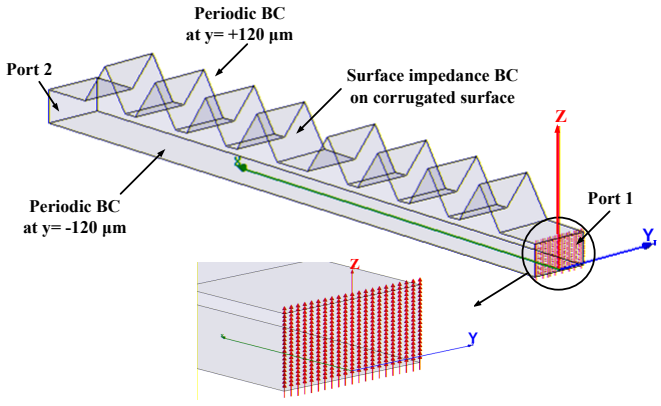

Figure 4.4: Corrugated parallel plate structure along with the field distribution at port 1. All dimensions are the same as those given in [114].

Fig. 4.5 shows the simulation results for the transmission parameter, S_{21}, of the unloaded structure. Two resonances are observed near 500GHz and 606GHz. Fig.

4.6 shows variation of the first resonance frequency f_{R1} versus surface reactance. The resonance frequency is calculated for the structure shown in Fig. 4.4 using the eigenmode solver in HFSS. The surface resistance R_s mainly contributes to the transmission loss with negligible effect on the resonance frequency. The inset illustrates the details for very small values of X_s. As seen in Fig. 4.6, the resonance frequency is nearly a linear function of the surface reactance.

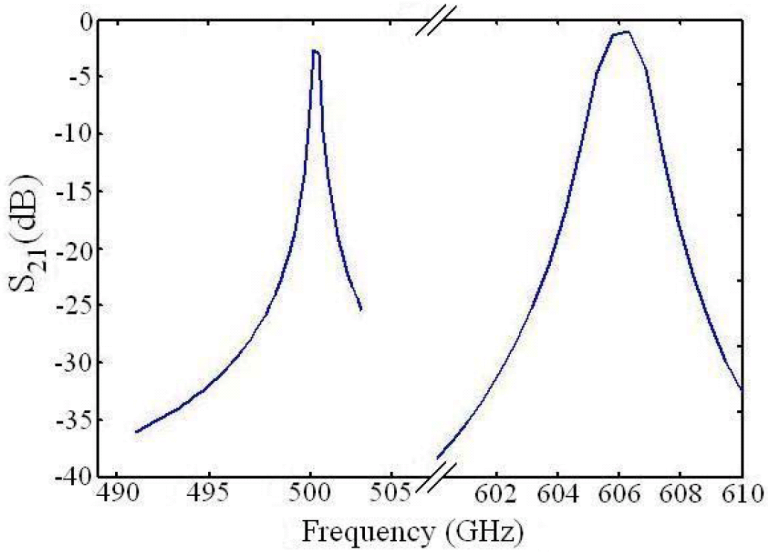

Figure 4.5: Simulated transmission parameter, S_{21}, for the unloaded resonator ($R_s = X_s = 0$). Two resonance frequencies are $f_{R1} = 500$GHz and $f_{R2} = 606$GHz.

The first order surface impedance [88] relates the physical parameters of the DNA monolayer to the surface reactance.

$$X_s = \frac{\mu_r \eta_0}{n_s} \tan(n_s k_0 t_s) \tag{4.1}$$

where $n_s = \sqrt{\epsilon_r \mu_r}$ is the refractive index of the DNA monolayer, $\eta_0 = 120\pi$ is the free space intrinsic impedance, $k_0 = \frac{2\pi}{\lambda_0}$ is the free space wave number, λ_0 is wavelength in free space, and t_s is the thickness of the monolayer.

One can find the corresponding relative permittivity and permeability of the thin film DNA from (4.1), provided the corresponding surface reactance for the two resonance frequencies. In [114], the shift in the first and second resonance frequency for a resonator loaded with double strand (ds-)DNA thin film are measured as 150 MHz and 280 MHz, respectively. The corresponding surface reactance for these resonance frequencies are 0.15 Ω and 0.28 Ω, respectively, from Fig. 4.6. Hence, the relative permittivity and permeability of the thin film ds-DNA from

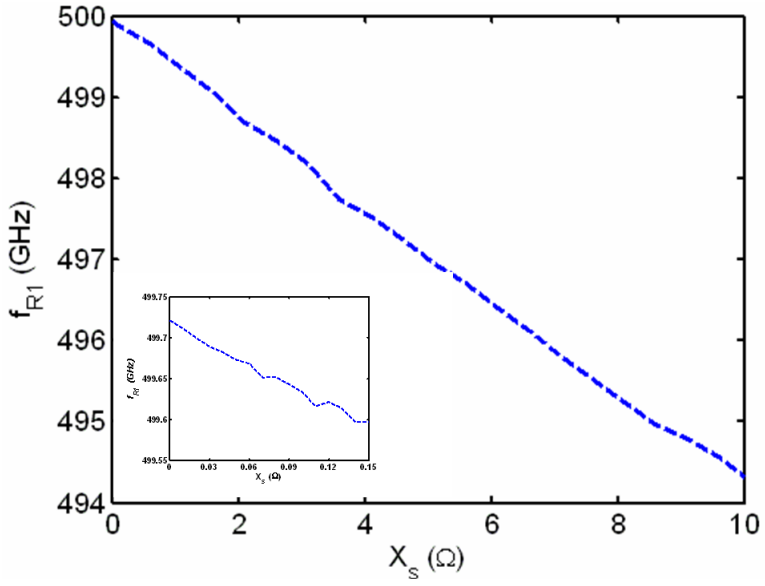

Figure 4.6: Calculated resonance frequency in terms of the surface reactance of the biochip. The inset shows the detail for very small values of X_s.

(4.1) will be $\epsilon_r = 47 \times 10^6$ and $\mu_r = 2.2$, which result in the equivalent refractive index of $n_s = 1 \times 10^4$ for the ds-DNA thin film. This is much higher than the reported value of $n_s = 2.6$ for the refractive index of amorphous DNA [21]. The relative permeability greater than unity implies that the thin film DNA behaves as a magnetic material. In the literature, the dielectric constant as high as 19×10^4 has been reported for thin solid films made of aligned ds-DNA [125], also in solid DNA films the formation of ferroelectric domains have been observed [126]. These reports support the predictions of the proposed surface impedance model.

4.6 Performance Analysis of the Biochip

The performance of a biosensor is determined by certain specifications which contribute to its functionality. High sensitivity and selectivity, simple preparatory steps, minimum sample modification and portability among other specifications distinguish a high performance biosensor.

In the proposed biochip sensor, since the device is capable of performing label-free recognition, fewer sample preparation steps are required compared to the schemes using markers. In addition, a label-free scheme have the advantage of causing minimum or no modification to the sample molecules. In the following,

the analytic sensitivity and selectivity of the proposed device are studied in more details.

4.6.1 Analytic Sensitivity and Selectivity

The analytic sensitivity is the lowest level of the analyte that can be reliably detected by the sensor. For the proposed device, the analytic sensitivity depends directly on the minimum measurable resonance frequency shift of the loaded resonator.

In practice, the resonator is coated with a thin film of e.g. DNA sample by simply pipetting the bio-material from an aqueous solution onto the device using microinjector. After the water evaporation, a thin film of DNA is formed above the resonator. As a more advanced method, the thiol-modified DNA strands can be immobilized on the golden regions of the resonator to give a better repeatability in the sensing process [127, 39].

To study the analytic sensitivity of the biochip, we model the presence of the biosample on the metal strips by a reactive surface impedance, X_s, as discussed in the previous Section. Given the accuracy of the resonance frequency shift measurement, the minimum thickness of the sample corresponding to the smallest detectable frequency shift is calculated as a measure of analytic sensitivity. We define the sensitivity of the resonance frequency, f_r, with respect to the sample thickness, t_s, as

$$S_{t_s} = \left.\frac{\partial f_r}{\partial t_s}\right|_{t_s=0} = \left.\frac{\partial f_r}{\partial X_s}\right|_{X_s=0} \cdot \left.\frac{\partial X_s}{\partial t_s}\right|_{t_s=0} \tag{4.2}$$

Given the reactive surface impedance in (4.1) and the resonance frequency as $f_r = \frac{c_0}{2L_{R1}n_{eff}}$, where n_{eff} is the effective refractive index seen by the CPS mode and c_0 is the speed of light in free space, the derivatives in (4.2) can be expressed as

$$\left.\frac{\partial f_r}{\partial X_s}\right|_{X_s=0} = -\frac{c_0}{2L_{R1}} \cdot \frac{1}{n_{eff}^2} \cdot \left.\frac{\partial n_{eff}}{\partial X_s}\right|_{X_s=0} \tag{4.3}$$

$$\left.\frac{\partial X_s}{\partial t_s}\right|_{t_s=0} = \frac{\pi\mu_r\eta_0}{L_{R1}} \cdot \frac{1}{n_{eff}} \tag{4.4}$$

Substituting (4.3) and (4.4) into (4.2) yields

$$S_{t_s} = -\frac{\pi c_0 \mu_r \eta_0}{2L_{R1}^2} \cdot \frac{1}{n_{eff}^3} \cdot \left.\frac{\partial n_{eff}}{\partial X_s}\right|_{X_s=0} \tag{4.5}$$

The dependency of the effective index on the surface reactance can be calculated from modal analysis discussed in Section 3.4.1. Fig 4.7 shows the effective index seen by the CPS mode as a function of the surface reactance at 500 GHz. The CPS dimensions were chosen as $w = 8.4\mu$m, $s = 8.4\mu$m and $d = 20\mu$m.

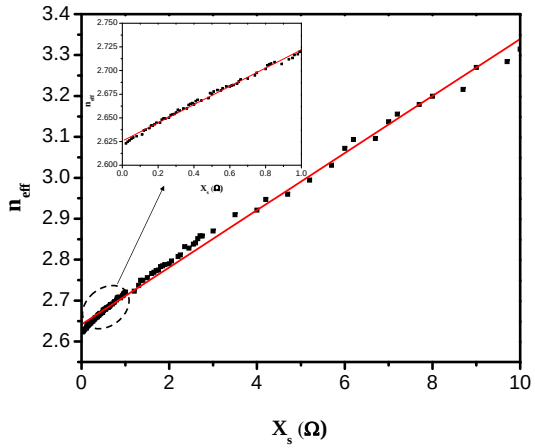

Figure 4.7: Effective index seen by the CPS mode as a function of the surface reactance at 500 GHz. The CPS dimensions were chosen as $w = 8.4\mu$m, $s = 8.4\mu$m and $d = 20\mu$m.

Using (4.5), Fig. 4.8 illustrates the analytic sensitivity, i.e. the lowest detectable sample thickness, as a function of the minimum measurable resonance frequency shift for two thin film samples with different permeability.

The analytic selectivity is a measure of the sensor ability to distinguish the analyte of interest from others. For example, in a DNA-base biosensor, the selectivity determines the ability of the device to distinguish between a single strand DNA (ss-DNA) and double strand DNA (ds-DNA) possessing a certain number of bases based on the slight difference in their refractive index. Given the accuracy of the resonance frequency shift measurement, the smallest difference in refractive indices of two samples which corresponds to the minimum detectable frequency shift can be consider as a measure of analytic selectivity. We define the sensitivity of the resonance frequency, f_r, with respect to the sample refractive index, n_s, as

$$S_{n_s} = \frac{\partial f_r}{\partial n_s} = \frac{\partial f_r}{\partial X_s} \cdot \frac{\partial X_s}{\partial n_s} \tag{4.6}$$

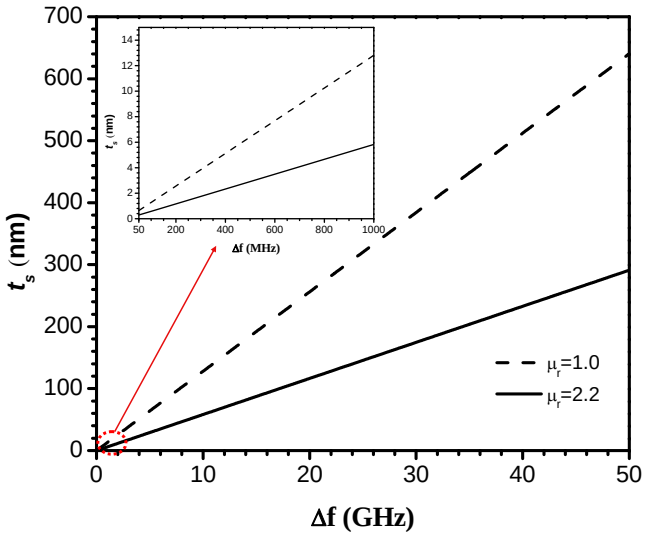

Figure 4.8: The lowest detectable sample thickness as a function of the minimum measurable resonance frequency shift for two thin film samples with different permeability.

Given the reactive surface impedance in (4.1) and the resonance frequency as $f_r = \frac{c_0}{2L_{R1}n_{eff}}$, (4.6) can be expressed as

$$S_{n_s} = -\frac{n_{eff}}{n_s} \cdot \frac{[AB^2D - (BD)X_s + (AD)X_s^2]}{n_{eff}B + [AB^2 + AX_s^2]\frac{\partial n_{eff}}{\partial X_s}} \cdot \frac{\partial n_{eff}}{\partial X_s} \tag{4.7}$$

where

$$A = \frac{\pi n_s t_s}{L_{R1} n_{eff}} \tag{4.8a}$$

$$B = \frac{\mu_r \eta_0}{n_s} \tag{4.8b}$$

$$D = \frac{c_0}{2L_{R1} n_{eff}^2} \tag{4.8c}$$

Using (4.7), Fig. 4.9 illustrates the analytic selectivity, i.e. the lowest detectable refractive index contrast, as a function of the minimum measurable resonance frequency shift for a non-magnetic sample with refractive index of $n_s = 2.6$ and for several thicknesses.

As an example, the selectivity analysis (Equation (4.7)) predicts a requirement of at list 2 GHz frequency resolution to be able to distinguish between two thin film samples with refractive indices of 1.5 and 1.7 (index contrast of 0.2) and thickness of 3 μm. Fig. 4.10, compares the frequency response of the resonator loaded with such

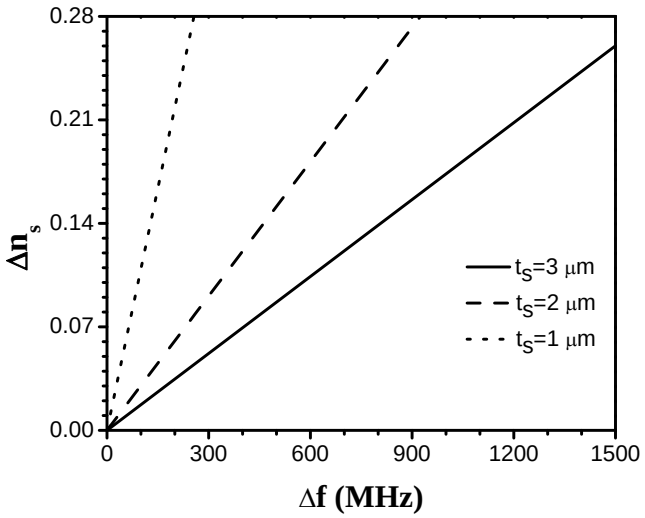

Figure 4.9: The lowest detectable refractive index contrast as a function of the minimum measurable resonance frequency shift for a non-magnetic sample with refractive index of $n_s = 2.6$ and thickness as a parameter.

samples obtained from full-wave simulation. The actual frequency shift is around 2.5 GHz. Obviously the frequency measurement resolution should be better than this value. It is worth to note that the frequency measurement resolution depends on several factors including the laser line widths, Q-factor of the resonator and the post-processing algorithm which extracts the resonance frequency from measured data.

4.7 Conclusion

The proposed integrated CW THz biosensor has several advantages over the previously proposed THz biochips working based on time-resolved THz pulse emission; the frequency response of the resonator, which possesses the sensing information, is simply obtained directly by tuning one of the laser frequencies around the resonance frequency. Moreover, in CW regime, the frequency resolution is much better compared to time domain methods, therefore, the finest features in the frequency response is resolved. Additionally, coherent detection is not necessary as required in THz pulse detection which results in a simpler hardware setup. Finally, the generated THz power is higher compared to non-distributed THz photomixers leading to an improved signal-to-noise ratio.

By making an array of resonators, several unknown targets are detected simul-

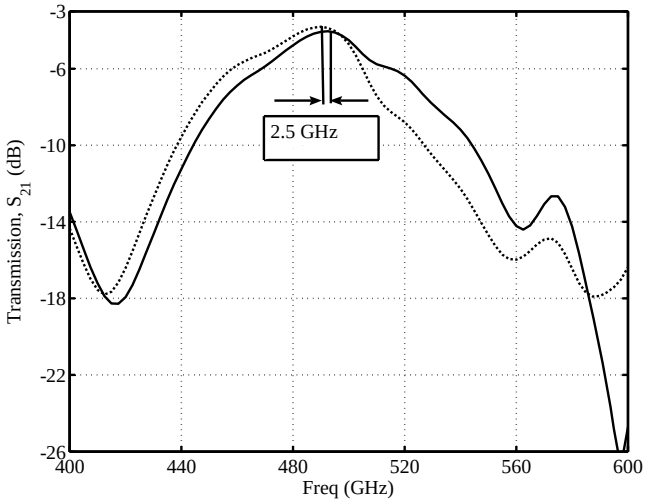

(a)

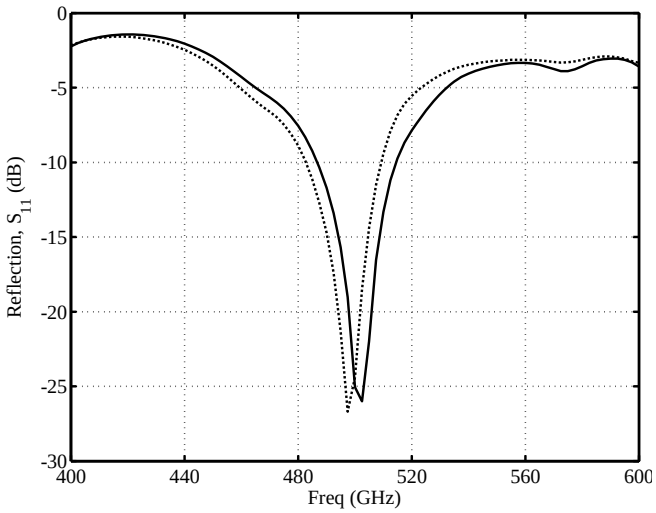

(b)

Figure 4.10: Comparison of the frequency response of the CPS resonator obtained from full-wave simulations. The resonator is loaded with 3-μm-thick thin film dielectric samples having refractive indices of $n_s = 1.5$ (solid line) and $n_s = 1.7$ (dotted line).

taneously which increases the sensing throughput. The significant advantage of using the integrated biosensor system is that the amount of the target sample required for reliable detection is reduced dramatically compared to other conventional approaches.

The Main benefit of the THz biochip compared to its commercially available optical counterpart is that it is label-free, namely, no additional label molecules are needed to be attached to the target molecules for recognition. Labelling schemes not only impose additional costly and time-consuming preparatory steps, but also they may introduce modifications in the target molecule structure, e.g. DNA strand conformation, and lower the precision of the recognition.

Applying the concept of reactive surface impedance for modeling of functionalized metallic surfaces by DNA monolayer was proposed for the first time based on which an analytical tool for evaluating the sensitivity and selectivity was developed.

Chapter 5

Whispering Gallery Mode Resonators

5.1 Introduction

In Chapter 4, a representative design of planar resonators with coplanar metallic strips was studied when used as a dielectric sensing transducer. The planar resonator is advantageous in a sense that it can be monolithically fabricated and integrated with the active components such as source and detector of a biochip, however, its sensitivity is limited. This is because, at very high frequencies, the unloaded Q-factor of such resonators can not reach large values (at best several tens in value) due to high conduction loss and attenuation coefficient, α, which is inverse proportion with the Q-factor ($Q = \frac{\beta}{2\alpha}$, where β is the propagation constant). Therefore, to achieve high Q-factor, other type of resonators should be considered.

In this Chapter, we turn our attention to dielectric resonators (DRs) acting on higher order modes or the so-called Whispering Gallery Modes (WGMs). Whispering gallery mode resonances are excited in an axisymmetric dielectric resonator such as sphere, disk or ring. WGMs are travelling waves around the center of such DR, and are confined inside the resonator through repeated total internal reflections from the exterior interface. The phase shift in each rotation is integer multiples of 2π. WGMs are attractive for sensing applications due to high sensitivity and selectivity resulting from the fact that they exhibit high unloaded Q-factor. For highly confined modes, the Q-factor is mainly limited by the loss tangent of the resonator material which could be very small ($\tan\delta \approx 10^{-4}$) at mm- and submillimeter-wave range. Size of the resonator becomes impractically small at conventional TE, TM

or hybrid modes [128]. Nevertheless, DRs acting on WGMs have relatively large dimensions even in the mm- and submillimeter-wave range which makes them less sensitive to fabrication tolerances.

In a disk shaped resonator, whispering gallery modes can be classified as WGE_{mpl}, having transverse electric field, or WGH_{mpl}, having axial electric field [37]. The integer subscripts m, p and l denote zero crossings in the electric field amplitudes in the azimuthal, radial, and axial directions, respectively. WGE_{m00} and WGH_{m00} modes are more suitable for sensing application since most of the electromagnetic energy is essentially confined in a small region around the boundary of the DR, therefore, any perturbation on the border area due to the presence of a sample produces a significant change in the resonance characteristics, and results in a high sensitivity.

In this Chapter, an analytical model for resonance frequency and Q-factor is proposed for two configurations of layered cylindrical dielectric resonators acting on whispering gallery modes. This model is later used in sensitivity analysis and dielectric sensing discussed in the next Chapter. Moreover, WGM excitation through dielectric image waveguide is investigated.

5.2 Theoretical Modeling of Layered Dielectric Disk Resonator

In this section, analytical models estimating the resonance frequency and Q-factor of the layered cylindrical dielectric resonators acting on whispering gallery modes are presented. Both axially and radially layered configurations are investigated.

5.2.1 Axially Layered DR

Various approximate analytical models exist for analysis of single-layered dielectric resonators [129], however, multi-layered whispering gallery dielectric resonators have not been studied as extensively as single-layered counterparts. In [130], a mode matching method for determining the resonance frequencies of the whispering gallery modes in a double cylindrical disk dielectric resonator has been presented. Also a double stacked configuration of dielectric resonators working in whispering gallery modes has been discussed in [131] using the same method of mode matching.

Here, we extend the Dielectric Waveguide Model (DWM) [132] to estimate the resonance frequency of a two-layer axially stacked DR acting on WGM. Fig. 5.1(a) illustrates a two-layer axially stacked dielectric resonator placed on a ground plane. Region 1 and 2 represents two disks with relative permittivity of ε_{rd} and ε_{rs}, respectively, surrounded by free space with dielectric constant of ε_0. Thickness of the lower and upper disk is b and h, respectively, and they have the same radius a.

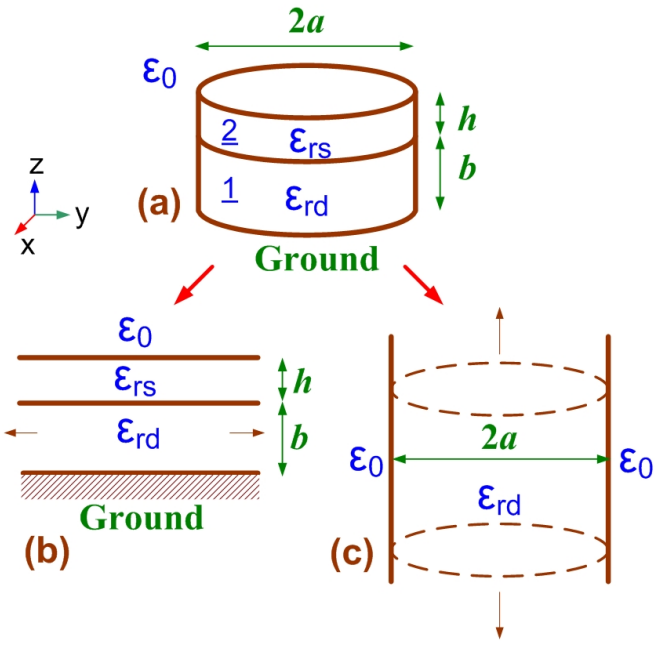

Figure 5.1: Illustration of dielectric waveguide model for (a) an axially layered DR. Axial wavenumber is approximated from (b) an infinite two-layer slab waveguide, whereas radial wavenumber is obtained from (c) an infinitely long cylindrical waveguide.

DWM is an extension of the Marcatili's method [133] which has been successfully used to find the propagation constant of a dielectric waveguide with rectangular cross section. The basic idea is to reduce the object dimension in one direction when solving the wavenumber in the other direction.

For the purpose of this study, it is assumed that the whispering gallery resonance mode is axially confined in the main resonator in region 1, and the field decays exponentially in region 2 where a sample is placed. This assumption is true when total reflection occurs at the interface of region 1 and 2, i.e. $\sqrt{\varepsilon_{rs}}k_0 < k_\rho < \sqrt{\varepsilon_{rd}}k_0$ where k_ρ is the radial wavenumber in region 1, and k_0 is the free space wavenumber. This assumption implies that the sample acts as a surrounding medium for the lower disk resonator, and its impact is to perturb the propagation constant of the excited

whispering gallery resonance mode in region 1. In our model, the axial wavenumber, k_z, of the resonator in region 1 is approximated by k_z of the corresponding region of an infinite two-layer slab waveguide shown in Fig. 5.1(b), whereas the radial wavenumber, k_ρ, in region 1 is approximated by that of corresponding infinitely long cylindrical waveguide having a relative dielectric constant of ε_{rd}.

In the two-layer dielectric slab shown in Fig. 5.1(b), k_z in the lower slab is obtained from a transcendental equation for TM_l modes given by [134]

$$1 - \frac{\varepsilon_{rs} k_z}{\varepsilon_{rd} k_{z2}} \tan\left(k_z b\right) \tan\left(k_{z2} h\right) = \frac{1}{\alpha_{z3} \varepsilon_{rs}} \left[k_{z2} \tan\left(k_{z2} h\right) + \frac{\varepsilon_{rs} k_z}{\varepsilon_{rd}} \tan\left(k_z b\right) \right] \tag{5.1}$$

where

$$\begin{aligned} \alpha_{z3} &= \sqrt{k_0^2 \left(\varepsilon_{rs} - 1\right) - k_{z2}^2} \\ k_{z2} &= \sqrt{k_z^2 - k_0^2 \left(\varepsilon_{rd} - \varepsilon_{rs}\right)} \end{aligned} \tag{5.2}$$

It is noted that some TE modes including the one corresponds to the lowest order of the similar slab with double height are suppressed by the ground plane as the ground plane can be considered as a symmetry plane for the slab with double height.

The transcendental equation governing the radial wavenumbers, as shown in Fig. 5.1(c), is approximated by that of an infinite cylindrical dielectric waveguide [135]

$$\left[\frac{J_m'\left(u\right)}{u J_m\left(u\right)} + \frac{K_m'\left(v\right)}{v K_m\left(v\right)} \right] \left[\frac{J_m'\left(u\right)}{u J_m\left(u\right)} + \frac{K_m'\left(v\right)}{\varepsilon_{rd} v K_m\left(v\right)} \right] = m^2 \left(\frac{1}{u^2} + \frac{1}{v^2} \right) \left(\frac{1}{u^2} + \frac{1}{\varepsilon_{rd} v^2} \right) \tag{5.3}$$

where $J_m\left(\cdot\right)$ and $K_m\left(\cdot\right)$ are the m-th order bessel function of the first kind and modified bessel function of the second kind, respectively. $J_m'\left(\cdot\right)$, $K_m'\left(\cdot\right)$ are the derivatives of bessel functions with respect to the argument, and $u = k_1 a$ and $v = k_2 a$ with a representing the radius of the cylinder and

$$\begin{aligned} k_1 &= \sqrt{k_0^2 \varepsilon_{rd} - k_z^2} \\ k_2 &= \sqrt{k_z^2 - k_0^2} \end{aligned} \tag{5.4}$$

Equations (5.1) and (5.3) form a system of nonlinear equations with k_z and k_0 as unknown variables from which the resonance frequency, $k_0 = \frac{\omega_r}{c_0}$, of the

two-layer axially stacked DR shown in Fig. 5.1(a) is obtained. ω_r is the angular resonance frequency and c_0 is speed of light in free space. In Table 5.1, the WGH_{m00} resonance frequencies calculated from the aforementioned analytical method are compared with those obtained from full-wave numerical method based on finite element method (FEM) for Body of Revolution (BOR) [136]. For this simulation the following parameters were chosen: $a = 5.0\ mm$, $b = 1.0\ mm$, $h = 4.0\ mm$, $\varepsilon_{rd} = 14.80$, and $\varepsilon_{rs} = 2.33$. Also the measured resonance frequency up to $m = 10$ is included in Table 5.1 for the same resonator structure. The good agreement between the two methods and the measured frequencies validate the accuracy of the analytical method.

Table 5.1: Comparison of WGH_{m00} resonance frequencies of a two-layer axially stacked resonator ($a = 5.0\ mm$, $b = 1.0\ mm$, $h = 4.0\ mm$, $\varepsilon_{rd} = 14.80$, and $\varepsilon_{rs} = 2.33$)

Resonance frequency (GHz)						
m	DWM	FEM-BOR	Measured	m	DWM	FEM-BOR
6	27.598	28.277	27.675	11	40.006	40.433
7	30.035	30.671	30.332	12	42.539	42.922
8	32.497	33.080	32.988	13	45.082	45.426
9	34.982	35.510	35.665	14	47.634	47.943
10	37.486	37.962	38.365	15	50.192	50.469

5.2.2 Radially Layered DR

A field-theoretical model has been derived in [137] for prediction of the resonance frequency of nonradiative dielectric multiple-ring structure placed between two parallel conducting plates. Here, we adopt the previously discussed DWM for a two-layer radially stacked dielectric resonator placed on one conducting plate.

Fig. 5.2(a) illustrates a two-layer radially stacked dielectric resonator placed on a ground plane. Region 1 and 2 are represented by relative permittivity of ε_{rs} and ε_{rd}, respectively, surrounded by free space with dielectric constant of ε_0. The inner and outer radius is r_1 and r_2, respectively, and the thickness is b.

For the purpose of this study, it is assumed that the whispering gallery resonance mode is radially confined in region 2, and the field decays exponentially in region 1 where a sample is placed. This assumption implies that the sample acts as

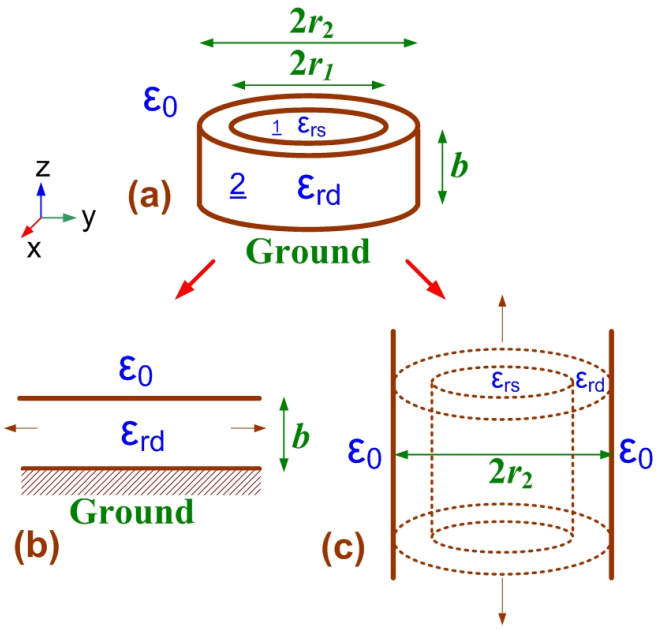

Figure 5.2: Illustration of dielectric waveguide model for (a) a radially layered DR. Axial wavenumber is approximated from (b) an infinite slab waveguide, whereas radial wavenumber is obtained from (c) an infinitely long radially inhomogeneous cylindrical waveguide.

a surrounding medium for the ring resonator, and its impact is to perturb the propagation constant of the excited whispering gallery resonance mode in region 2. The axial wavenumber, k_z, of the ring resonator in region 2 is approximated by k_z of an infinite slab waveguide shown in Fig. 5.2(b), whereas the radial wavenumber, k_ρ, in region 2 is approximated by that of corresponding infinitely long radially inhomogeneous cylindrical waveguide as shown in Fig. 5.2(c).

In the dielectric slab shown in Fig. 5.2(b), k_z is obtained from a transcendental equation for TM_l modes given by [134]

$$\frac{\varepsilon_{rd}\alpha_{z0}}{k_z} = \tan\left(k_z b\right) \tag{5.5}$$

where

$$\alpha_{z0} = \sqrt{k_0^2\left(\varepsilon_{rd}-1\right) - k_z^2} \tag{5.6}$$

The transcendental equation governing the radial wavenumbers, as shown in Fig. 5.2(c), is approximated by that of an infinite cylindrical dielectric waveguide. In [138], the dispersion relation for a radially inhomogeneous dielectric cylinder problem has been discussed in detail based on 4 by 4 transfer matrix technique.

Only the relevant formulations are repeated here for the sake of completeness. The dispersion relation is obtained by setting the determinant of a 4 by 4 matrix equal to zero [138]

$$\det \begin{bmatrix} c_1(r_1) & 0 & -M_{11} & -M_{13} \\ 0 & d_1(r_1) & -M_{21} & -M_{23} \\ e_1(r_1) & f_1(r_1) & -M_{31} & -M_{33} \\ g_1(r_1) & h_1(r_1) & -M_{41} & -M_{43} \end{bmatrix} = 0 \tag{5.7}$$

where the elements of the this matrix is given in the Appendix B. Equations (5.5) and (5.7) form a system of nonlinear equations with k_z and k_0 as unknown variables from which the resonance frequency, $k_0 = \frac{\omega_r}{c_0}$, of the two-layer radially stacked DR shown in Fig. 5.2(a) is obtained. In Table 5.2, the WGH_{m00} resonance frequencies calculated from the aforementioned analytical method are compared with those obtained from full-wave numerical method based on FEM-BOR. For this simulation the following parameters were chosen: $r_1 = 4.0\ mm$, $r_2 = 5.0\ mm$, $b = 3.0\ mm$, $\varepsilon_{rd} = 14.80$, and $\varepsilon_{rs} = 2.33$. The excellent agreement between the two methods validates the accuracy of the analytical method.

Table 5.2: Comparison of WGH_{m00} resonance frequencies of a two-layer radially stacked resonator ($r_1 = 4.0\ mm$, $r_2 = 5.0\ mm$, $b = 3.0\ mm$, $\varepsilon_{rd} = 14.80$, and $\varepsilon_{rs} = 2.33$)

Resonance frequency (GHz)					
m	DWM	FEM-BOR	m	DWM	FEM-BOR
6	25.136	25.176	11	38.181	38.186
7	27.766	27.797	12	40.770	40.772
8	30.383	30.405	13	43.357	43.356
9	32.989	33.004	14	45.943	45.940
10	35.588	35.597	15	48.529	48.523

5.2.3 Q-Factor Estimation

Using the field distribution of a lossless structure as an estimation of the field for lossy one, Q-factor of the resonator structures shown in Fig. 5.1(a) and Fig. 5.2(a) can be estimated as

$$Q_u^{-1} = \gamma_d \tan\delta_d + \gamma_s \tan\delta_s + Q_{con}^{-1} + Q_{rad}^{-1} \tag{5.8}$$

where Q_u is the unloaded Q-factor of the layered resonator structure, γ_d and γ_s are the electric energy filling factor for regions represented by ε_{rd} and ε_{rs}, respectively, and is defined as the ratio of the stored electric energy in the corresponding region to the total electric energy stored in the whole resonator structure, $\tan\delta_d$ and $\tan\delta_s$ are the loss tangent of the regions represented by ε_{rd} and ε_{rs}, respectively, Q_{con} represents the Q-factor due to conduction loss, and Q_{rad} accounts for the radiation loss. Q_{con} is obtained from

$$Q_{con}^{-1} = \frac{R_s \iint_S \overrightarrow{H_t} \cdot \overrightarrow{H_t^*} dS}{4\omega_r W_e} \tag{5.9}$$

where $\overrightarrow{H_t}$ is the magnetic field tangential to the metallic surface S with surface resistance of $R_s = \sqrt{\frac{\omega_r \mu_0}{2\sigma}}$, ω_r is the angular resonance frequency, and W_e is the total electric energy stored in the whole resonator structure.

The radiation loss can be estimated by Volume Current Method (VCM) which has been discussed in [139]. The VCM is an approach by which the unknown far field is calculated from the known near field. In this method, an equivalent volume current source is defined based on the calculated near field. In our case the near field is obtained from DWM presented before. Once the equivalent current source is known, the problem of finding the radiation field is analogous to an antenna problem.

In Table 5.3, the unloaded Q-factor of a two-layer axially stacked resonator calculated from (5.8) is given for different values of $\tan\delta_s$. For this calculation the following parameters were chosen: $a = 5.0\ mm$, $b = 1.0\ mm$, $h = 4.0\ mm$, $\tan\delta_d$=0.0001, $m = 10$, $\varepsilon_{rd} = 14.80$, and $\varepsilon_{rs} = 2.33$.

Q_{con} and Q_{rad} for this structure are calculated as 3.6×10^3 and 1.1×10^8, respectively. It is noted that once the resonator is coupled to an exciting waveguide, the resulting loaded Q-factor decreases depending on the amount of the coupling coefficient as discussed in the next section.

Table 5.3: Calculated unloaded Q-factor of a two-layer axially stacked resonator ($a = 5.0\ mm$, $b = 1.0\ mm$, $h = 4.0\ mm$, $tan\delta_d$=0.0001, $m = 10$, $\varepsilon_{rd} = 14.80$, and $\varepsilon_{rs} = 2.33$)

Unloaded Q-factor				
$\tan\delta_s$	0.1	0.01	0.001	0.0001
Q_u	230	1,200	2,030	2,190

5.3 Whispering Gallery Mode Excitation by a Dielectric Image Waveguide

Excitation of WGMs in optical wavelengths is usually achieved through coupling into tapered fibers [139]. In mm-wave range a dielectric image waveguide (DIW) is a good candidate as it exhibits low-loss characteristic and wide-band performance. Moreover, DIW is easy to fabricate and test.

Fig. 5.3 shows our fabricated prototype consisting of a dielectric disk resonator coupled to a dielectric image waveguide. Dielectric waveguide has the width of w, height of t, and length of L. The disk resonator has the radius of a and thickness of b, and is placed in a distance of s from the waveguide. Both waveguide and DR are placed on a metallic support plate. The power coupling into and out of the dielectric image waveguide is realized by using two rectangular metallic waveguide adaptors (shown as 2.9 mm coaxial to WR-28 waveguide adaptors in Fig. 5.3). To increase coupling efficiency between the dielectric waveguide and rectangular metallic waveguide, and to decrease the loss due to the reflection and scattering at the discontinuities, the dielectric waveguide is linearly tapered at the input and output ends.

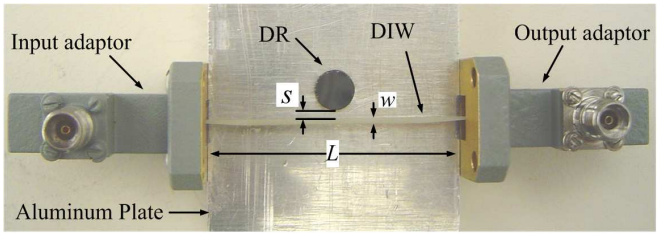

Figure 5.3: Prototype of a dielectric disk resonator coupled to a dielectric image waveguide.

Dielectric image waveguides exhibit low-loss characteristic and wide-band performance at mm-wave frequencies. Fig. 5.4 illustrates the measured transmission

and reflection response of the fabricated DIW (w = 1 mm, t = 2.1 mm, L = 35 mm, $\epsilon_r = 9.8$, $\tan\delta = 0.0001$) without any disk resonator in place at the frequency range of 26–36 GHz. As shown in Fig. 5.4, the insertion loss and return loss is less than 1 dB and -10 dB, respectively, in the frequency range of interest.

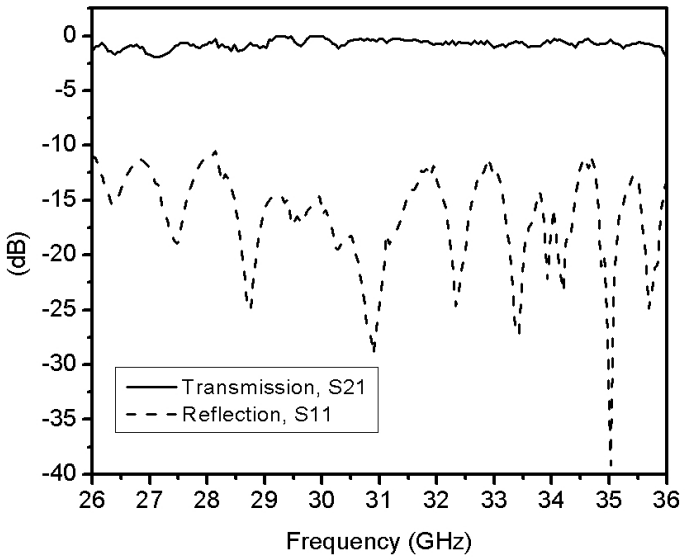

Figure 5.4: Measured transmission and reflection response of a designed dielectric image waveguide (w = 1 mm, t = 2.1 mm, L = 35 mm, $\epsilon_r = 9.8$, $\tan\delta = 0.0001$).

In DIW structures, most of the wave energy is confined inside the dielectric region while an evanescent tail of the guided field is accessible outside the waveguide which makes it suitable for power coupling into a dielectric resonator. The extension of the field tail can be controlled by the width of the dielectric waveguide (parameter w in Fig. 5.3). Smaller width results in a longer tail for the field, and therefore, in practice coupling between DR and DIW will be less sensitive to the distance s.

In a disk or ring type resonator, the energy density of WGH_{m00} mode mainly concentrates near the outer rim, and in general can be decomposed into two traveling waves propagating in opposite directions along the circumference of the resonator. When utilizing a standard magnetic or electric field probes both directions are excited resulting in a standing wave resonance. If the excitation method is made directional, it is possible to excite only one direction and form a traveling wave resonance [140]. An evanescent tail of the field is extended outside the resonator, therefore, these modes can be easily excited when the DR is placed in the vicinity of the evanescent field of a DIW structure [141]. In full wave simulations of the structure shown in Fig. 5.3, we observed the excitation of both traveling and standing wave resonances, depending on the mode number, m, distance s and

geometrical dimensions.

To analyze the exchange of power between the dielectric image waveguide and the resonator, we consider a generic model. Assuming that the coupling between DR and DIW is directional and lossless, the power transmission coefficient, T, of the waveguide coupled to the resonator can be expressed as [142]

$$T = \frac{1 + \eta^2 - \kappa^2 - 2\eta\sqrt{1-\kappa^2}\cos\,\theta}{1 + \eta^2 - (\eta\kappa)^2 - 2\eta\sqrt{1-\kappa^2}\cos\,\theta} \tag{5.10}$$

where $0 < \eta < 1$ is the loss factor of the resonator and is defined as the normalized amplitude after a single turn propagation around the resonator ($\eta = 1$ represents a lossless resonator), κ is the coupling coefficient magnitude, and θ is the phase shift per rotation inside the resonator. θ can be related to the angular frequency, ω, by $\theta = \frac{\omega}{c_0} n_{\mathtt{eff}} l$ where $n_{\mathtt{eff}}$ is the effective refractive index of the mode and l is the circumference of the DR.

At the resonance condition, $\theta = 2\pi m$, when $\eta = \sqrt{1-\kappa^2}$ is satisfied, the transmitted power vanishes in (5.10), and $T = 0$. Under this condition, known as critical coupling [142], the transmission response is extremely sensitive to any perturbation occurring in the value of η, κ, or θ as will be demonstrated in the next Chapter.

The coupling coefficient, κ, is obtained from an overlap integral of the resonator and DIW mode fields. Field expression for the resonator is estimated from DWM. Fig. 5.5 shows the calculated κ^2 for a structure with $w = 1.0$ mm, $t = 2.0$ mm, $\epsilon_r = 9.8$ for DIW, and $a = 5.0$ mm, $b = 1.0$ mm, $\varepsilon_{rd} = 14.80$ for the resonator. As seen, κ^2 is exponentially decaying with respect to the separation distance s.

Once the coupling coefficient is known, the external Q-factor, Q_{ext}, is estimated as [139]

$$Q_{ext} = \frac{2\pi m}{\kappa^2} \tag{5.11}$$

The loaded Q-factor, Q_l, then is calculated from

$$Q_l^{-1} = Q_u^{-1} + Q_{ext}^{-1} \tag{5.12}$$

5.3.1 Resonance Mode Selection

A dielectric resonator have many orders of WGM resonances spreading out over a wide range of frequency spectrum. Each of those modes when excited under critical

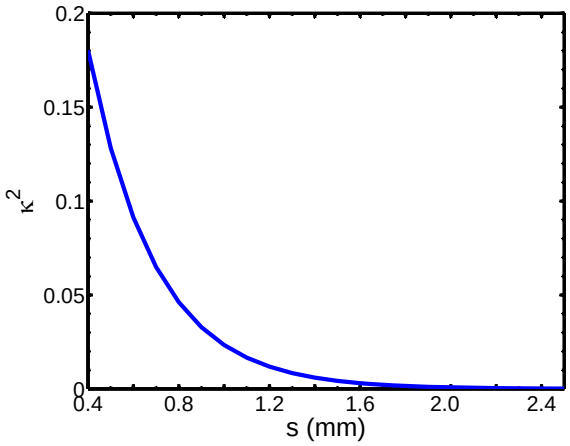

Figure 5.5: Calculated κ^2 for a structure with $w = 1.0$ mm, $t = 2.0$ mm, $\epsilon_r = 9.8$ for DIW, and $a = 5.0$ mm, $b = 1.0$ mm, $\varepsilon_{rd} = 14.80$ for the resonator.

coupling condition demonstrates a dominant response with relatively high Q-factor compared to the others in a given frequency band. In our structure, the dominant mode is selected by adjusting the coupling between DR and DIW. In practice, the coupling adjustment can be easily achieved through changing the distance s as shown in Fig. 5.5.

In sensing applications this feature is appealing as it enables one to select and dominate the mode which has resonance frequency close to the frequency at which the sample, e.g. biological specimen, has absorption signature. This way when the DR is loaded by the sample, the change in Q-factor of the selected mode gives rise to high sensitivity sensing due to its relatively high Q-factor.

Under critical coupling condition provided for a resonance mode, the whole input power is coupled to the DR and trapped inside the resonator. In this case, no power is transmitted through the output end or reflected back from the input end of the waveguide. Fig. 5.6 illustrates the field distribution for a resonance mode under near critical coupling condition obtained from full-wave numerical simulation using HFSS. In the simulation the dielectric waveguide was defined as alumina with $\epsilon_r = 9.8$, $w = 1$ mm and $t = 2.1$ mm. DR was defined as silicon with $\epsilon_r = 11.2$, $a = 4.75$ mm and $b = 1$ mm, and distance s was selected to be 0.9 mm to obtain near critical coupling at 31.53 GHz.

As seen in Fig. 5.6, the input power coming from the left hand side is coupled to DR. A traveling-wave WGM is excited which propagates around the resonator in the counter clockwise direction and as expected very small amount of power transmits to the second port on the right hand side.

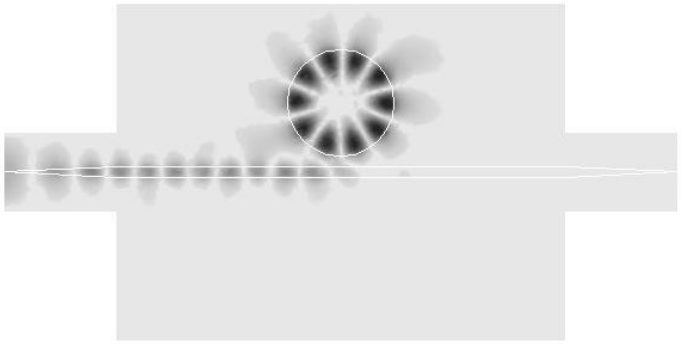

Figure 5.6: Field distribution obtained from full-wave numerical simulation at near critical coupling condition. The frequency is 31.53 GHz.

Fig. 5.7 illustrates the simulated transmission and reflection response of the structure shown in Fig. 5.6. Four resonances are observed in 26-36 GHz frequency range. The mode with resonance frequency of 31.53 GHz has a deeper and narrower response compared to the other modes suggesting that near critical coupling condition has been provided for this mode. It is noted that the reflection at the resonance frequencies is better than 10 dB.

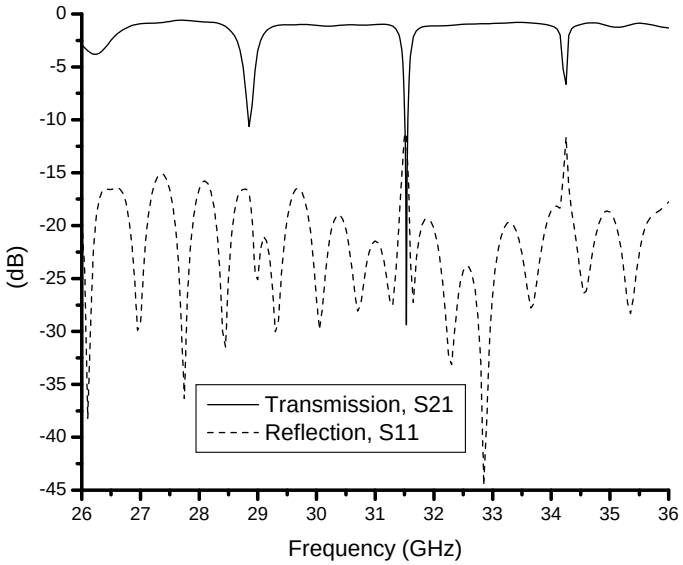

Figure 5.7: Simulated transmission and reflection response for the structure shown in Fig. 5.6. The mode with resonance frequency of 31.53 GHz is in near critical coupling condition by setting $s = 0.9$ mm.

In practice, it is possible to provide near critical coupling for any of the modes appearing in a given frequency band to have a pronounced response [143]. This can be achieved by changing the distance between the DR and dielectric image

waveguide.

Fig. 5.8 shows the measured frequency response of the device in Fig. 5.3. The design parameters were similar to those used in the previous simulation. As predicted by simulation, four resonances are observed at 26.00 GHz, 28.81 GHz, 31.66 GHz, and 34.63 GHz. In this experiment, by adjusting the distance s, near critical coupling condition is demonstrated for the second mode in Fig. 5.8a, third mode in Fig. 5.8b, and fourth mode in Fig. 5.8c. It is noted that in each graph Q-factor of the critically coupled mode is the highest.

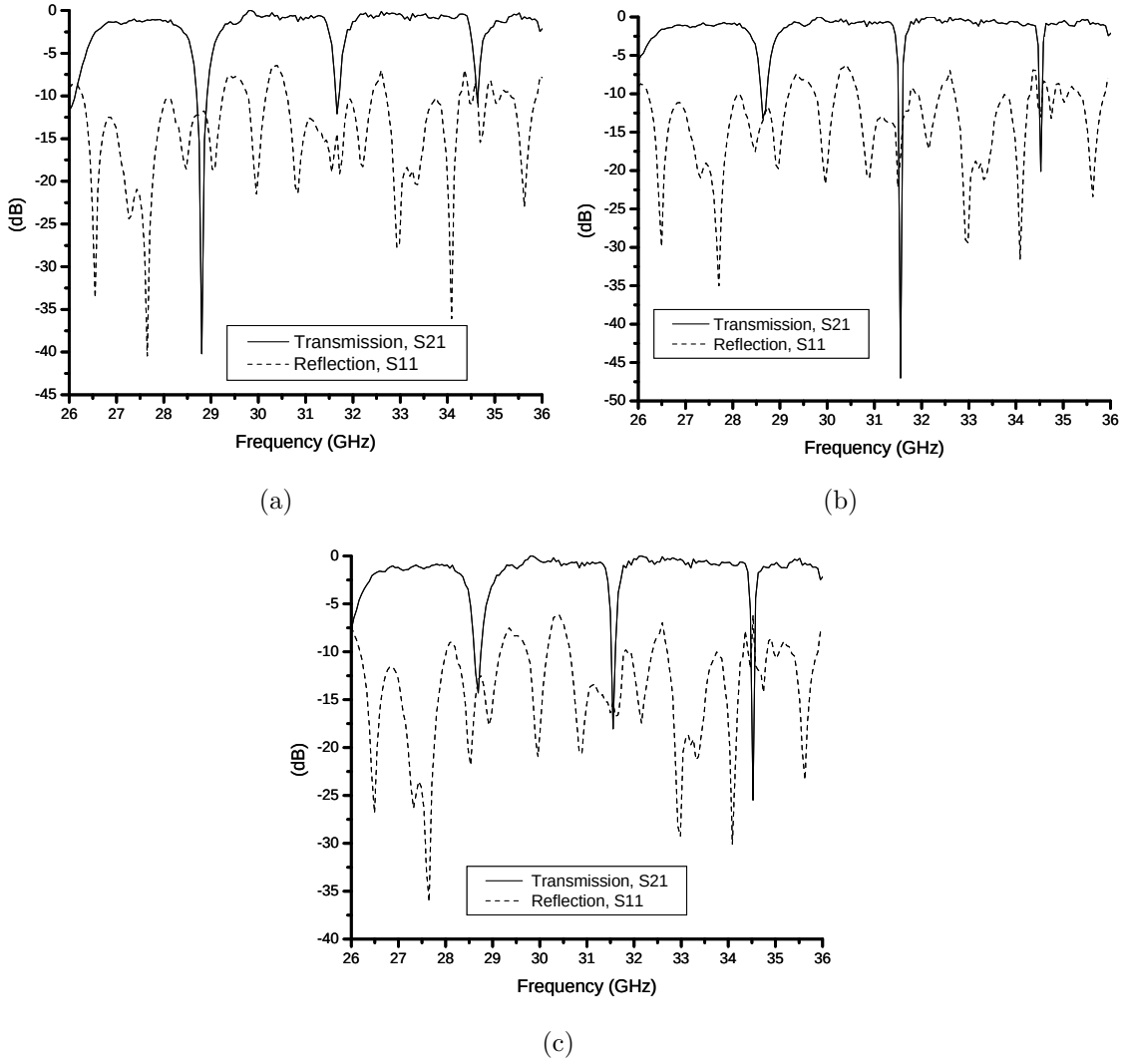

Figure 5.8: Measured frequency response of the device shown in Fig. 5.3. Adjusting the distance between the DR and DIW provides near critical coupling for the (a) second mode (b) third mode and (c) fourth mode in the frequency band.

5.4 Conclusion

In this Chapter, the theoretical foundation of using disk- and ring-shaped whispering gallery resonators as dielectric sensors was laid down. The disk-shaped configuration is best suited for sensing solid thin film samples when placed on top of a WGM disk resonator whereas the WGM ring resonator is suitable specially for liquid samples filling inside the ring.

A practical way of exciting WGM resonator through dielectric waveguide was investigated. It was shown that any order of resonance modes, in a given frequency range, is enhanced when the DR is critically coupled to the waveguide. This capability greatly increases the sensitivity as discussed in the next Chapter.

The analytical modeling, developed and experimentally tested in this Chapter for millimetre-wave range, can be readily used in terahertz range by scaling the geometrical dimensions. It is worth noting that dielectric waveguides and dielectric resonators are particularly advantageous in terahertz range compared to their metallic counterparts as they provide higher performance in terms of electromagnetic loss and Q-factor.

Chapter 6

A High Sensitivity Sensor Based on Millimeter-Wave Whispering Gallery Resonator

6.1 Introduction

Whispering gallery modes have attracted much interest in sensing applications due to high Q-factor that they exhibit as non-radiating modes. The open structure of a whispering gallery resonator, unlike the metallic cavity, also provides convenient ways of placing and removing samples interacting with the resonator.

Resonance perturbation method is applied on a whispering gallery mode by placing a sample under test in the evanescent field of the resonator. The sample perturbs the resonance mode, and causes a change in the resonance frequency and Q-factor. Variation in the resonance characteristics is calibrated to represent the sensing parameter of interest.

In the literature, much attention has focused on WGM for sensing in optical range [50, 144] whereas less effort has been dedicated to utilize them in the millimetre-wave and terahertz range. Although the proposed sensors working in optical range are highly sensitive and selective, their fabrication, sample preparation, and test are sophisticated and expensive. To expand the sensing applications of WGMs in the millimetre-wave and terahertz range, in this Chapter, a sensor device based on WGM resonant perturbation method is proposed for analysis of (bio)chemicals in liquid or solid form. A sensitivity analysis is discussed followed by

demonstration of sensing and characterization measurement results on solid samples and liquid droplets.

6.2 Sensitivity Analysis

In this section, sensitivity of the WGM technique to the complex permittivity of the sample is investigated for two sample placement configurations. It is assumed that the sample under study is in a disk type shape with the complex relative permittivity of $\varepsilon_{rs} = \varepsilon'_{rs} - j\varepsilon''_{rs}$. The sample can be placed on top of a cylindrical dielectric resonator as in Fig. 5.1(a) or inside a dielectric ring resonator as in Fig. 5.2(a). In either case, the sample interacts with the evanescent field of the main resonator. The permittivity of the resonator is represented by $\varepsilon_{rd} = \varepsilon'_{rd} - j\varepsilon''_{rd}$. The combined sample and resonator is placed near a DIW for excitation. The measured transmission coefficient of the coupled structure, then, is taken as a measure of the sensing parameter of interest. The transmission coefficient in logarithmic scale is given by

$$\mathfrak{T} = 10\log T \tag{6.1}$$

where T represents the power transmission coefficient given in (5.10). We define the sensitivity of the transmission coefficient at resonance with respect to the real and imaginary part of the sample dielectric constant as

$$S_r = \frac{\partial \mathfrak{T}}{\partial \varepsilon'_{rs}} \tag{6.2}$$

$$S_i = \frac{\partial \mathfrak{T}}{\partial \varepsilon''_{rs}} \tag{6.3}$$

Assuming the real and imaginary part of the sample permittivity mainly affect the phase shift per rotation inside the resonator, θ, and the resonator loss factor, η, respectivly, the sensitivities can be rewritten as

$$S_r = \frac{\partial \mathfrak{T}}{\partial \theta} . \frac{\partial \theta}{\partial \varepsilon'_{rs}} \tag{6.4}$$

$$S_i = \frac{\partial \mathfrak{T}}{\partial \eta} . \frac{\partial \eta}{\partial \varepsilon''_{rs}} \tag{6.5}$$

$\frac{\partial \mathfrak{T}}{\partial \theta}$ and $\frac{\partial \mathfrak{T}}{\partial \eta}$ terms are determined from the coupling model given in (5.10). These terms have their maximum value when critical coupling condition is provided. To

illustrate this fact, Fig. 6.1(a) shows the transmission coefficient with respect to the resonator loss factor at the resonance and with a fixed value of coupling coefficient ($\kappa = 0.2$). As shown, the maximum slope of the graph happens when the critical coupling condition is satisfied, i.e. $\eta = \sqrt{1-\kappa^2}$. Fig. 6.1(b) shows the transmission coefficient with respect to the phase shift per rotation inside the resonator for the same value of coupling coefficient and for three different loss factor. Again when the critical coupling condition is provided the graph has its maximum slope near the resonance ($\theta = 0$).

In calculation of $\frac{\partial\theta}{\partial\varepsilon'_{rs}}$ and $\frac{\partial\eta}{\partial\varepsilon''_{rs}}$ terms in (6.4) and (6.5), it is more convenient to relate θ and η to the resonance frequency, f_r, and Q-factor of the resonator structure, respectively. For the weak axial propagation constant ($k_z << \sqrt{\varepsilon'_{rd}}k_0$) [145] the term $\frac{\partial\theta}{\partial\varepsilon'_{rs}}$ near the resonance can be approximated by

$$\frac{\partial\theta}{\partial\varepsilon'_{rs}} = (2\pi)^2 r \frac{\sqrt{\varepsilon'_{rd}}}{c_0}\frac{\partial f_r}{\partial\varepsilon'_{rs}} \tag{6.6}$$

where $r = a(r_2)$ for disk(ring) configuration, and $\frac{\partial f_r}{\partial\varepsilon'_{rs}}$ is the sensitivity of the resonance frequency with respect to real part of the sample permittivity. This sensitivity can be calculated from the modeling discussed in Section 5.2. Fig. 6.2(a) shows WGH_{m00} resonance frequency shift due to the change of the real part of the sample permittivity for an axially layered DR with $a = 5.0$mm, $h = 4.0$mm, $\varepsilon'_{rd} = 14.8$ and two values for the resonator thickness, b. The azimuthal mode number is chosen to be $m = 10$. The slope of the graphs determine the sensitivity which is -0.260 and -0.083 GHz/(unit change in ε'_{rs}) for $b = 1.0$mm and $b = 1.5$mm, respectively. As shown in Fig. 6.2(a), the resonance frequency sensitivity is lower when the resonator is thicker. This is due to the fact that the field tends to concentrate axially more on the bottom surface of the main disk resonator near the ground plane. Therefore, the thicker the disk, the weaker the field would be on the top surface of the disk where the sample is placed. This results in a less interaction with the sample.

Fig. 6.2(b) shows WGH_{m00} resonance frequency shift due to the change of the real part of the sample permittivity for a radially layered DR with $r_1 = 4.0$mm, $b = 3.0$mm, $\varepsilon'_{rd} = 14.8$ and two values of outer radius r_2. The mode number is chosen to be m=10. The slope of the graphs determine the sensitivity which is -0.089 and -0.030 GHz/(unit change in ε'_{rs}) for $r_2 = 5.0$mm and $r_2 = 5.5$mm, respectively. As shown in Fig. 6.2(b), the resonance frequency sensitivity is lower when the outer radius of the ring resonator is bigger. This is due to the fact that the

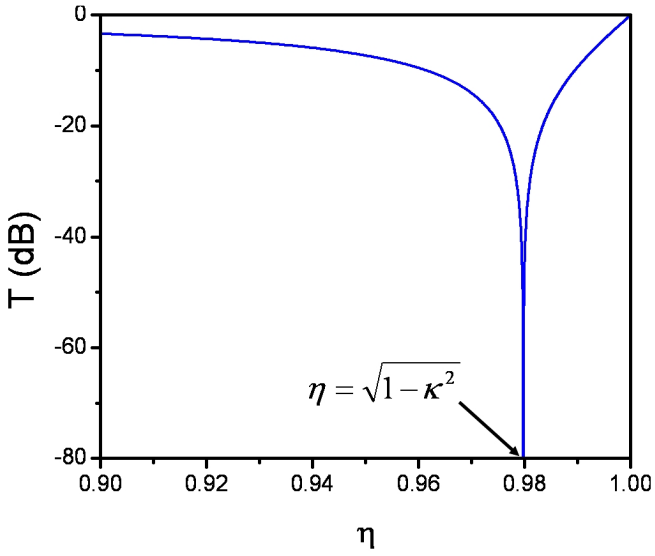

(a)

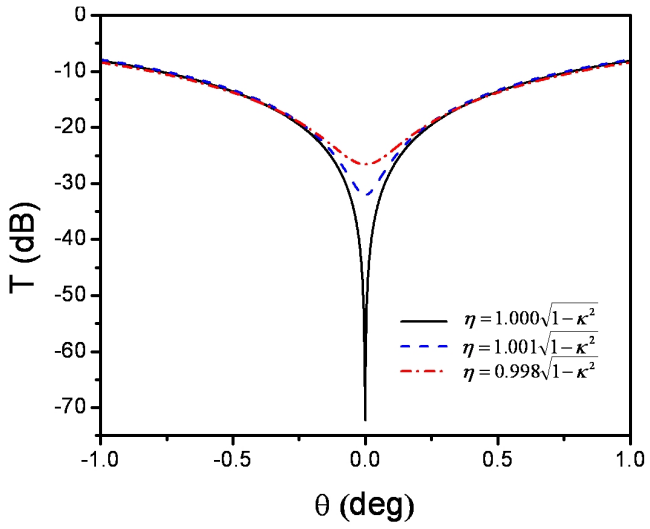

(b)

Figure 6.1: Transmission coefficient with respect to the (a) resonator loss factor at the resonance and with the fixed value of coupling coefficient ($\kappa = 0.2$). (b) phase shift per rotation inside the resonator for the same value of coupling coefficient and for three different loss factors.

field tends to concentrate radially more on the outer rim of the ring. Therefore, the larger the outer radius, the weaker the field would be near the inner rim of the ring where the sample is placed which results in a less interaction with the sample. It is noted that Fig. 6.2 can also be used as a calibration graph to estimate the real part of the sample permittivity by measuring the corresponding resonance frequency shift.

The resonator loss factor is the normalized wave amplitude after a single turn along a circular path with radius r. Near the resonance, the loss factor can be approximated by [145]

$$\eta = \exp(-\pi r k_0 \sqrt{\varepsilon'_{rd}} \frac{1}{Q_u}) \tag{6.7}$$

where Q_u is the unloaded Q-factor of the layered resonator structure. Taking derivative of (6.7) yields

$$\frac{\partial \eta}{\partial \varepsilon''_{rs}} = -\eta \ln(\eta) \frac{1}{Q_u} \frac{\partial Q_u}{\partial \varepsilon''_{rs}} \tag{6.8}$$

where $\frac{\partial Q_u}{\partial \varepsilon''_{rs}}$ is the sensitivity of the Q-factor with respect to imaginary part of the sample permittivity. This sensitivity can be calculated from (5.8), and expressed as

$$\frac{\partial \eta}{\partial \varepsilon''_{rs}} = Q_u \eta_0 \ln(\eta_0) \frac{\gamma_s}{\varepsilon'_{rs}} \tag{6.9}$$

where η_0 is the resonator loss factor corresponding to the lowest measurable transmission coefficient with a certain signal-to-noise ratio or dynamic range (see Fig. 6.1(a)). It is noted that the sensitivity with respect to ε''_{rs} is proportional to the Q-factor of the resonator implying that larger Q-factor leads to higher sensitivity.

The minimum detectable variation in real, ε'_{rs}, and imaginary, ε''_{rs}, part of the sample dielectric constant depends upon the S_r and S_i sensitivities defined in (6.4) and (6.5), respectively, and also the specification of the measurement instrument. Assuming that the measurement instrument has a typical specification of 40 dB dynamic range and 0.5 dB resolution in transmission coefficient measurement, by using (5.10), (6.4) and (6.6), a variation of 8.4×10^{-5} and 2.3×10^{-4} in the ε'_{rs} can be detected in the discussed disk and ring resonator configurations, respectively, described in Fig. 6.2. Using (5.8), (5.10), (6.5) and (6.9), a minimum variation of 4.7×10^{-4} can be detected in ε''_{rs} for the configuration described in Table 5.3 with $Q_u = 230$.

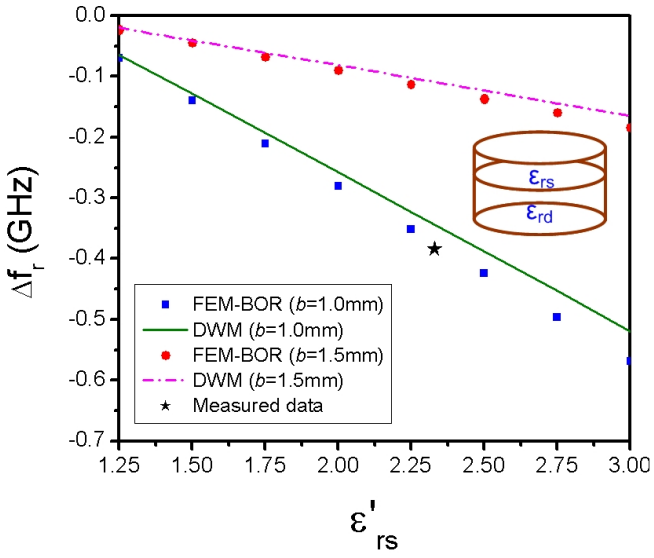

(a)

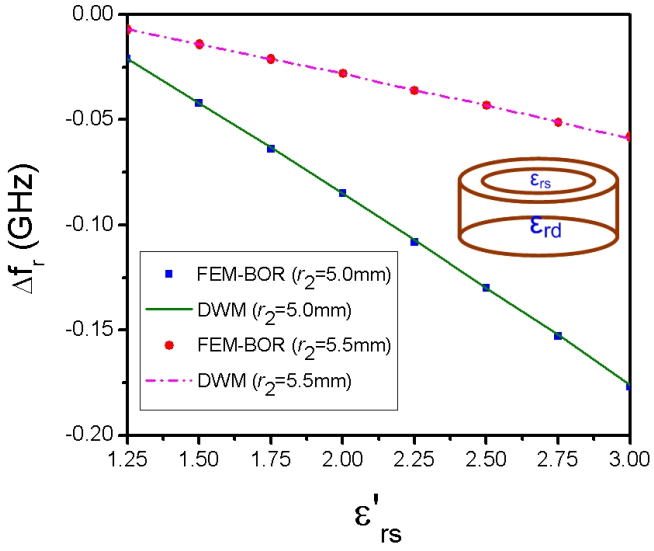

(b)

Figure 6.2: WGH_{m00} resonance frequency shift due to the change of the real part of the sample permittivity for (a) axially layered DR with $a = 5.0$mm, $h = 4.0$mm, $\varepsilon'_{rd} = 14.8$. $\star$ point shows a measured resonance frequency shift for a sample with $\varepsilon'_{rs} = 2.33$ (b) radially layered DR with $r_1 = 4.0$mm, $b = 3.0$mm, $\varepsilon'_{rd} = 14.8$. The mode number is chosen to be m=10.

6.3 Sensing and Characterization Measurement Results

6.3.1 Drug Tablet

We propose, for the first time, the application of whispering gallery mode perturbation technique in dielectric analysis of disk shape pharmaceutical tablets [146]. Fig. 6.3 shows our fabricated prototype of the WGM sensor module used for testing drug tablets. A foam sheet covers the dielectric resonator and the dielectric image waveguide such that the top of the DR is accessible through an opening hole providing a fixed holding compartment for the tablet. A network analyser was deployed to measure the transmission response of the device in the frequency range of interest. The measured results showed that the covering foam does not affect the response noticeably due to its low loss characteristic and relative dielectric constant that is close to one. The tablet is fitted into the holding compartment such that it touches the top surface of the DR and is surrounded by the foam sheet in its circumference. This way the sample sits in the exact same place each time it is tested, hence, the measurements will be repeatable. We noticed that the resonance response is not sensitive to the tablet thickness since the evanescent field decays exponentially inside the tablet. However, to ensure repeatable results the tablet diameter should be slightly larger than that of the disk resonator such that it completely covers the whole top surface of the DR. In our experiments, we tested several types of over-the-counter drug tablets, however, in the following we report the results for Acetaminophen, 325mg. The test results for other types and dosages not reported were qualitatively similar to those reported here.

It is known that moisture affects the stability of some drug substances by causing decomposition [147], therefore, monitoring of the moisture uptake by the tablet over time is of great importance in pharmaceutical industry. Since the absorbed moisture will change the dielectric properties, we conducted a series of experiments to study the performance of the proposed sensor on sensing moisture absorbed by the drug tablets, . Fig. 6.4 compares the measured transmission response of the sensor for moisture sensing; In case I, a tablet was tested immediately after it was taken out of its sealed pillbox. This measurement can be used as a reference test for other cases. In case II, the tablet was exposed to moisture by placing it near a glass of water for 45 minutes at room temperature before it was tested. As shown, the transmission response has been increased by around 14.4 dB at the resonance which represents a decrease in the Q-factor. This is due to the fact that water is lossy in

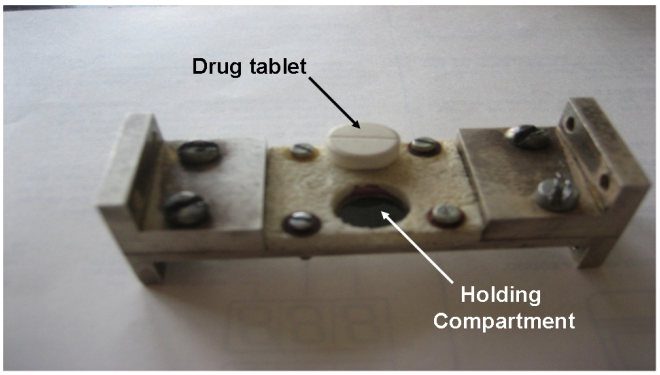

Figure 6.3: Fabricated prototype of the WGM sensor module for testing drug tablets. The tablet is placed inside the holding compartment above the disk resonator.

mm-wave range, and the absorbed water in the tablet increases the total dielectric loss of the resonance structure. In case III, the tablet was exposed to moisture for 4.5 hours with the same condition as in case II before it was tested. As shown, the Q-factor is even smaller as more moisture has been absorbed by the tablet, and also a resonance frequency shift of around 100 MHz is observed. In case IV, the tablet was kept outside the pillbox at normal room environmental condition for 18.5 hours before test. A larger Q-factor is observed in this case implying that the absorbed moisture by the tablet is lower than that of case II and III as the tablet was not exposed to additional moisture source other than the room humidity. In this case, the resonance frequency shifted down by around 50 MHz, and the transmission response increased by 6.4 dB at the resonance.

In tablet formulation, different excipient materials with nonmedicinal effect are mixed with the active ingredient, which acts as a medicinal agent, in order to give the tablet the desired properties such as hardness, disintegration, dissolution, friability, uniformity, and sufficient size for easy handling [148]. The choice of excipients varies among different manufacturer and in many cases is considered as a trade secret. Therefore, the dielectric constant of a tablet composition is unique to each manufacturer, and can be used as a signature for identification.

Fig. 6.5 illustrates the measured transmission response of the sensor before and after tablet placement. In this experiment, drug tablets were from the same type, and with similar size and shape, but manufactured by three different pharmaceutical companies. A distinct resonance behavior is seen for each manufacturer in Fig. 6.5. The estimated relative permittivity of the drug tablets from the resonance frequency shift of $\mathrm{WGH}_{10,0,0}$ mode (see Fig. 6.2(a)) was around $\varepsilon'_{rs} \simeq 3$.

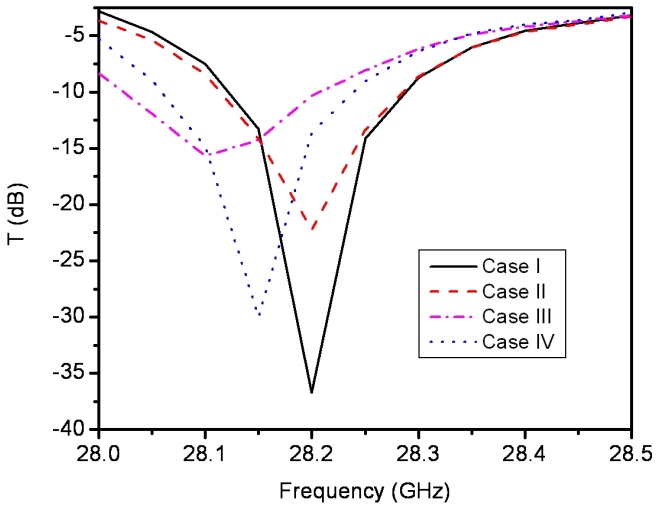

Figure 6.4: Measured transmission response showing the moisture uptake by the tested tablet. Test conditions for each case is explained in the text.

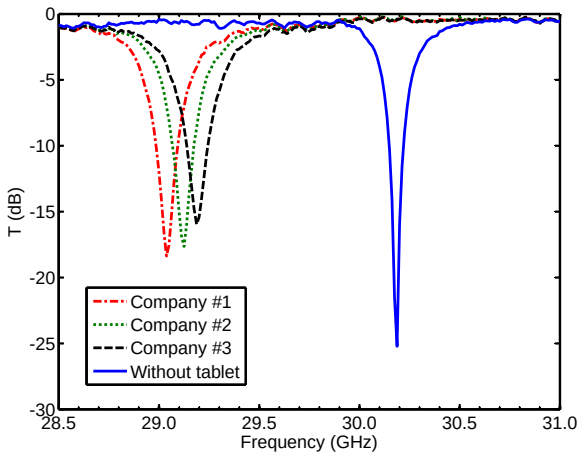

Figure 6.5: Measured transmission response of WGH_{700} mode before (solid) and after tablet placement. Drug tablets are from the same type, and with similar size and shape, but manufactured by three different pharmaceutical companies.

To include the effect of the fabrication tolerances, we conducted a statistical experiment on a large number of tablets for each company. Fig. 6.6 illustrates the statistical data for mean and standard deviation of the resonance frequency measured for the drug tablet from the previous three different pharmaceutical companies. Although the tested tablets from the selected manufacturers all have the same active ingredients and dosage, a slight difference in their dielectric constant was detected as shown in Fig. 6.6 by the distinct ranges of resonance frequency. A similar result was obtained for the resonance line width (not shown). This experiment suggests that the proposed sensor is suitable for screening purpose in the production line to ensure that the overall mixture ratio of the tablet composition is within the acceptable range. Moreover, this technique can be used to distinguish a counterfeit tablet from the authentic one from the existing difference in their dielectric properties.

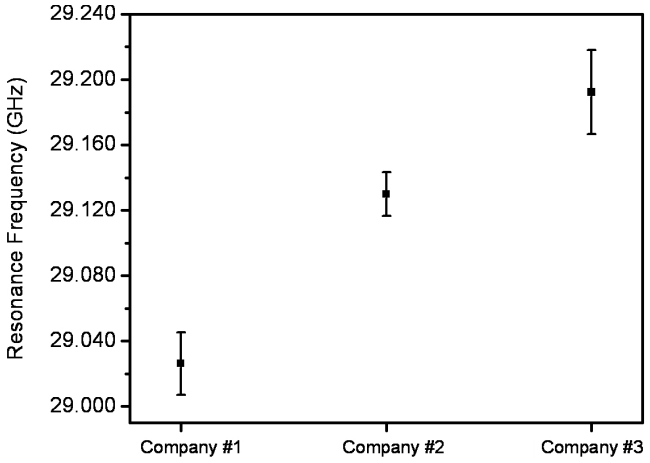

Figure 6.6: Measured statistical data for mean (square) and standard deviation (bar) of the resonance frequency for one type of drug tablet manufactured by three different pharmaceutical companies.

In tablet manufacturing process, there is always a chance of product contamination with unwanted particles. The contamination can occur during the powder preparation stage or during compacting e.g. when small metal particles are formed as chips from the hardened press tool [149]. Therefore, careful screening of the finished tablet is required to ensure a high quality product. Fig. 6.7 shows the variation of the resonance frequency measured for tablet samples selected from three categories, i.e. tablets without contamination (Group A), contaminated by steel particles (Group B), and iron particles (Group C). Metal particles had irregular shapes with the size of tenth of a millimeter. The particles were found in a few

number mainly bellow the surface of the tablet and in some cases visible to the eye. As shown in Fig. 6.7, the interval range of the resonance frequency for both kind of contaminated tablets are located above that of the normal tablets. Moreover, the standard deviation is larger for Group B and C due to the randomness of the contaminating particles.

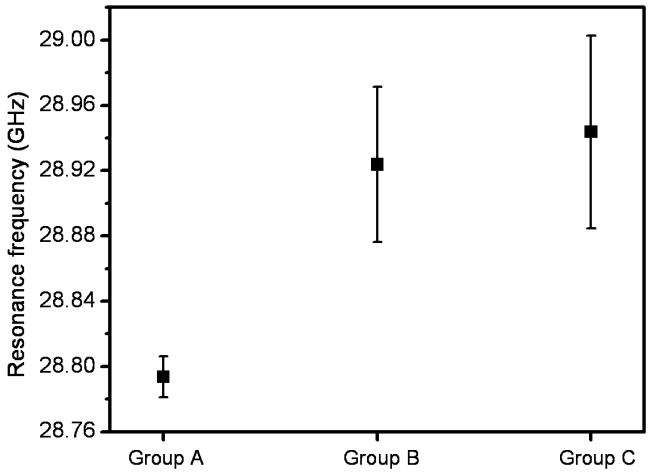

Figure 6.7: Variation of the resonance frequency measured for tablet samples selected from three categories of tablets without contamination (Group A), contaminated by steel particles (Group B), and by iron particles (Group C). Bars show the standard deviation.

6.3.2 Liquid Droplet

In liquid droplet sensing, top surface of the disk resonator in Fig. 5.3 was used as the active area for holding and sensing a droplet of liquid samples. Under critical coupling condition, as discussed in Section 6.2, the transmission response is extremely sensitive to any external perturbation occurred in the value of η, κ, or θ resulting from the injection of a minute droplet of a sample into the sensitive area of the disk surface. This fact is illustrated in Fig. 6.8 which shows the transmission response according to (5.10) for a resonance at the critical coupling condition, and two of its variations obtained by 0.01% and 0.05% perturbation in η, and 0.036° increase in θ. The resonance line width and the frequency shift for the perturbed mode are attributed to the dielectric loss and dielectric constant of the sample, respectively. This model predicts that a sample with higher dielectric loss produces wider line width and shallower dip in the resonance, as seen in Fig. 6.8. Also, higher dielectric constant for the sample results in a larger frequency shift.

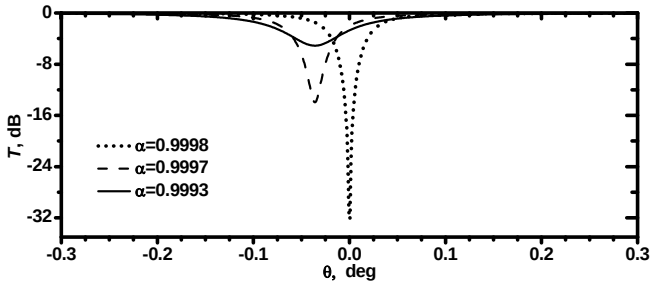

Figure 6.8: Power transmission response for a resonance under critical coupling with $\eta = 0.9998$ and $\kappa = 0.02$ (dotted curve), and two perturbed resonances with $\theta = 0.036°$, $\eta = 0.9997$ (dashed curve) and $\eta = 0.9993$ (solid curve).

Although this simple model may not give the absolute value of the dielectric parameters for the sample, however, in majority of sensing applications obtaining the absolute values is not important, rather determining the relative value of these parameters with respect to a reference material or other samples is more of interest [38, 39].

In designing the proposed sensor, since the spot size occupied by the droplet is much smaller than the disk surface in top, it is important to make sure that the coupling between the DR and DIW is highly directional; otherwise, a standing wave will be produced inside the DR which makes the transmission response dependent on the position of the droplet with respect to the mode pattern, e.g. if the drop is located on an antinode, it has the most interaction with the field whereas the least interaction occurs at the nodes. Fig. 6.9 shows the simulated transmission response of a designed traveling-wave WGM sensor with the following design parameters; $a = 5.0$mm, $b = 1.0$mm, $\epsilon_r = 14$, and $\tan\delta = 1 \times 10^{-4}$ for the disk, and $w = 1.0$mm, $t = 2.1$mm, $L = 35$mm, $\epsilon_r = 9.8$, and $\tan\delta = 1 \times 10^{-4}$ for the dielectric image waveguide. To perform the simulation, HFSS was utilized. The insets in Fig. 6.9 illustrate two snapshots of the traveling-wave field distribution of WGH_{600} mode at different times for the first resonance mode at 29.6GHz. The field shown in the left inset has 72° phase lead. Comparing the field patterns in the insets reveals the movement of the peaks and nulls of the traveling field over time (phase). As seen in Fig. 6.9, the field is mainly confined near the circumference of the disk where the most sensitive sensing area is formed. In Fig. 6.9, the first resonance mode is under near critical coupling condition, and as seen in the insets, minimal power is coupled to the exit port. As discussed in Section 5.3.1, the critical coupling condition can be achieved for any of the resonances occurs in the frequency range of interest by adjusting the distance between DR and DIW. This capability enables one to easily

choose any desired resonance mode to perform high sensitivity sensing.

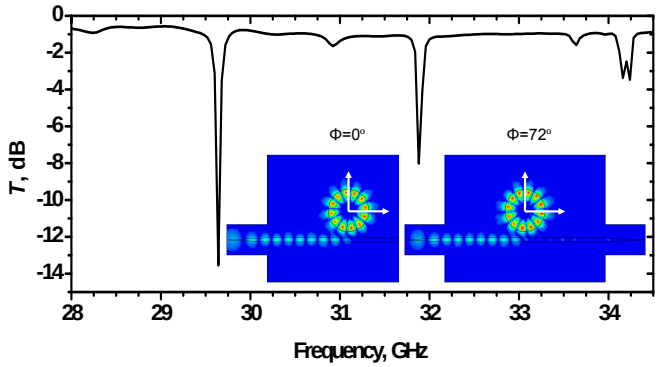

Figure 6.9: Simulated transmission response of a dielectric disk resonator coupled to a dielectric image. The insets illustrate two snapshots of the traveling-wave field distribution of WGH_{600} mode at different times for the first resonance mode at 29.6GHz. The field shown in the left inset has 72° phase lead.

For experiments, a network analyzer was deployed to measure the transmission response of the device in the frequency range of interest. To ensure the repeatability of the measured response, a micro-injector installed on a customized translation stage was used to give full control over the drop volume and the location where the drop is dispensed. The smallest volume that can be dispensed by the available injector is 0.5 μl. The average diameter of the spot occupied by the 1.0 μl and 0.5 μl drop of water on the disk surface is around 2 mm and 1 mm, respectively. The ratio of the drop spot area to the resonator surface area with the confined electromagnetic field is calculated as 1.2 percent for the 0.5 μl drop.

In Fig. 6.10(a), the measured transmission response when a 1-μl water droplet falls near the border of the disk is compared with the case where its center area was used for sensing. As expected from the field distribution in Fig. 6.9, the border shows higher sensitivity compared to the center area due to higher field-sample interaction. During experiments, it was realized that when the location of the drop moves around the circumference of the DR, the transmission response does not change noticeably unless the drop becomes close to the coupling region near the dielectric image waveguide. This also confirms that in practice the excited mode is travelling-wave and not standing-wave. In Fig. 6.10(b), sensor response to different liquids is shown. In this measurement, the relative resonance line width and the frequency shift are in consistent with relative values of the dielectric loss and the dielectric constant of the corresponding liquid, e.g. water has the highest value for the dielectric loss and the dielectric constant among the tested liquids and, as seen,

it produces the widest line width and the largest frequency shift.

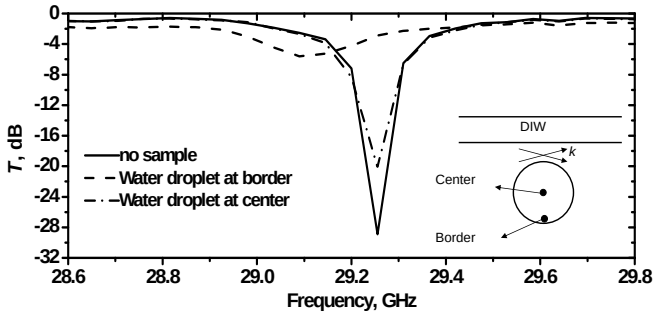

(a)

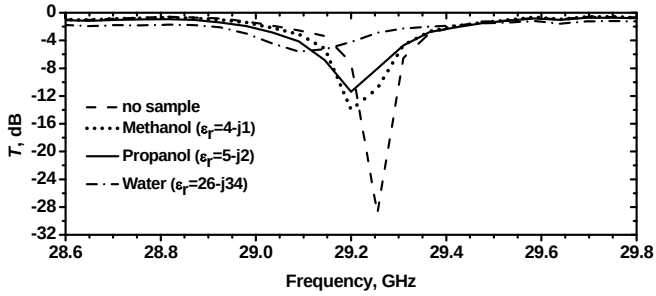

(b)

Figure 6.10: Comparing the measured sensor response when (a) 1-μl droplet of water is injected at the center and the border of the disk, (b) 1-μl droplets of different liquids are injected at the border.

Fig. 6.11 shows the sensor response to a 0.5-μl droplet of binary mixture of ethanol-water with different ratios. As seen, the concentration difference as small as 2% can be easily resolved using this method. One important aspect of the performed experiments was the repeatability of the measured responses which ensures the robustness of the sensing method.

Supported by the theoretical modeling, these experiments confirm that under critical coupling condition a small perturbation in the resonance mode manifests itself in a significant change in the transmission response. This change depends on the size and the location of the sample, as well as its dielectric properties.

6.4 Conclusion

The theoretical and experimental results presented in this Chapter indicate that the proposed WGM technique potentially provides a highly sensitive platform for

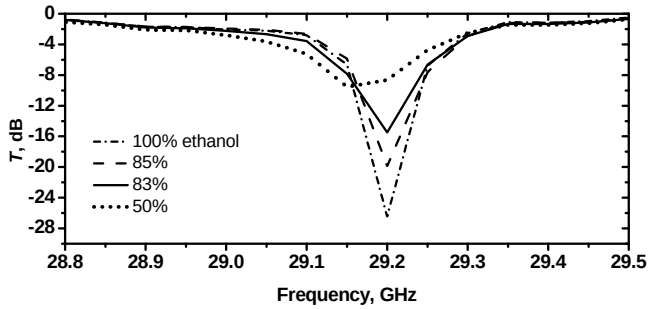

Figure 6.11: Measured sensor response to a 0.5-μl droplet of binary mixture of ethanol-water with different ratios.

dielectric analysis of (bio)chemical samples. It was shown that at near critical coupling condition the highest sensitivity is obtained. For the given structure, a comprehensive sensitivity analysis was performed to reveal that a variation in the order of 10^{-4} in real or imaginary part of the sample dielectric constant can be detected.

The application of whispering gallery mode perturbation technique in dielectric analysis of disk shape pharmaceutical tablets was reported for the first time. The results of various experiments carried out on drug tablets demonstrate the potential multifunctional capabilities of the sensor in moisture sensing, counterfeit drug detection, and contamination screening.

Furthermore, simple high sensitivity sensor device for liquid sensing in mm-wave range was demonstrated. This technique can be used to classify a large number of small sized (bio)chemical samples in liquid or solution form based on the differences in type, concentration or any other property which is related to dielectric constant and/or dielectric loss of the sample in the mm-wave range. The measurement and simulation results obtained in mm-wave hold promise for WGM to be used for sensing biological solutions in THz range with very high sensitivity.

Chapter 7

Concluding Remarks

7.1 Summary and Contributions

In this thesis, terahertz and mm-wave resonance based biosensors were explored from engineering point of view. The theoretical foundation for analysis and design of two proposed biosensors based on planar resonator and WGM resonator was laid down, and their performance in terms of sensitivity and selectivity was investigated in details.

In Chapter 3, a rigorous and global analysis and design tool for CW traveling-wave terahertz photomixers as the core component of a THz chip was developed. A systematic method was proposed for the optical waveguide design. The optical fill factor of the photoabsorbing region was introduced as the main design parameter from which the absorption length and the optimum length of the active region is determined. Moreover, in the formulation, the basic drift-diffusion partial differential equations were added by the trap charge dynamic equation to increase the accuracy and to prevent from non-physical net charge creation. Additionally, two methods were proposed for calculating the coupled THz signal into the CPS structure. The semi-analytical method is summarized in three main steps; in the first step, the incident field produced by the impressed photocurrent is found in the absence of the guiding structure. In the next step, the distributed source term in the transmission line representation is calculated from the incident field, and in the final step, the distributed-source transmission line equations are solved by using one-dimensional Green's functions. In the second method, by representing the total field in terms of the guided and radiated modes, the coupled terahertz signal into any desired guided mode is calculated rigorously. The importance of phase velocity match was

studied numerically. The proposed global analysis approach can be used for optimization of both material and geometry in terahertz photoconductive sources to increase optical-to-terahertz power conversion.

In Chapter 4, using the developed THz photomixer source, a resonance-based biochip structure was proposed and its operation principle was explained. A planar metallic resonator acting as a sample holder and transducer was designed, and its performance in terms of sensitivity and selectivity was studied through simulations. The concept of surface impedance for modeling of DNA self assembled monolayer on top of a gold surface was proposed for the first time and its effectiveness was discussed based on the available data in the literature. By applying the concept of reactive surface impedance for modeling of functionalized metallic surfaces by DNA monolayer, an analytical tool for evaluating the sensitivity and selectivity was developed. The proposed integrated CW THz biosensor has several advantages over the previously proposed THz biochips working based on time-resolved THz pulse emission; the frequency response of the resonator, which possesses the sensing information, is simply obtained directly by tuning one of the lasers. Moreover, in CW regime, the frequency resolution is much better compared to time domain methods, therefore, the finest features in the frequency response is resolved. Additionally, coherent detection is not necessary as required in THz pulse detection which results in a simpler hardware setup. Finally, the generated THz power is higher compared to non-distributed THz photomixers leading to an improved signal-to-noise ratio. By making an array of resonators, several unknown targets are detected simultaneously which increases the sensing throughput. The Main benefit of the THz biochip compared to its commercially available optical counterpart is the property of being label-free, namely, no additional label molecules are needed to be attached to the target molecules for recognition. Labeling schemes not only impose additional costly and time-consuming preparatory steps, but also they may introduce modifications in the target molecule structure, e.g. DNA strand conformation, and lower the precision of the recognition.

In chapter 5, whispering gallery mode resonances with high Q factor were studied as an alternative to metallic resonators, to address the loss challenge. The main disadvantage of the metallic planar resonators is that they are lossy at THz range and therefore can not provide high Q factor. This results in a low sensitivity for any sensor using such resonators. Theoretical modeling for axially and radially layered dielectric resonators acting on WGM were presented and the analytical results were compared to the measured data. Excitation of WGM through dielectric waveguide was proposed and the critical coupling condition was explained through analytical

formulation. The possibility of selecting one resonance among many for sensing application was also studied both theoretically and experimentally. The analytical modeling, which was developed and experimentally tested for millimeter-wave range in this Chapter, can be readily used in terahertz range by scaling the geometrical dimensions. It is worth noting that dielectric waveguides and dielectric resonators are particularly advantageous in terahertz range compared to their metallic counterparts as they provide higher performance in terms of electromagnetic loss and Q-factor.

In Chapter 6, a high sensitivity sensor based on WGM resonance in mm-wave was proposed and its sensitivity was studied in details. The performance of the proposed sensor was examined for sensing drug tablets and also liquid droplets through various measurements in mm-wave range. A comprehensive sensitivity analysis was performed to show that a change in the order of 10^{-4} in the sample permittivity can be detected by the proposed sensor. The application of whispering gallery mode perturbation technique in dielectric analysis of disk shape pharmaceutical tablets was reported for the first time. The results of various experiments carried out on drug tablets demonstrate the potential multifunctional capabilities of the sensor in moisture sensing, counterfeit drug detection, and contamination screening. A simple high sensitivity sensor device for liquid sensing in mm-wave range was demonstrated. This technique can be used to classify a large number of small sized (bio)chemical samples in liquid or solution form based on the differences in type, concentration or any other property which is related to dielectric constant and/or dielectric loss of the sample in the mm-wave range. The measurement and simulation results obtained in mm-wave hold promise for WGM to be used for sensing biological solutions in THz range with very high sensitivity.

7.2 Future Work

Followings are suggested as some possible directions for the further research work:

- **Study the thermal effects in the operation of travelling-wave photomixer sources**
  In Chapter 3, a global simulation tool was developed for analysis of travelling-wave terahertz photomixers. In the formulation, all the major phenomena in photonics, semiconductor physics and electromagnetic were included except for thermal generation and distribution. Thermal effects may not have

considerable impact for low and medium range of incident optical powers. Nevertheless, it should be considered for high optical powers.

- **Replacing the Poisson equation with the wave equation in the basic drift-diffusion model**
  In the drift-diffusion formulation discussed in Chapter 3, using Poisson equasion, to find the electric field, implies a quasi-static approximation. This approximation is acceptable as long as the cross sectional dimensions are much smaller than the wavelength. Otherwise, the transverse wave effects and transverse propagation transit time comes into the picture, which can be taken care of by including wave equation.

- **Experimental verification of the electromagnetic modeling of DNA self-assembled monolayer**
  In Chapter 4, applying surface impedance for electromagnetic modeling of thin-film DNA was proposed. This modeling can be further verified through additional experiments and, if necessary, higher order impedance boundary conditions can be used to improve the accuracy.

- **Dielectric constant measurement using whispering gallery mode resonance**
  The results of the theoretical modeling developed in Chapter 5 have been used for sensitivity analysis. These models may also be used for extracting real and imaginary part of the permittivity of the sample through an inverse method.

- **Fabrication and test of whispering gallery sensor in sub-millimeter range**
  In chapter 6, various experimental results were demonstrated for the WGM sensor in millimeter-wave range. By down-scaling the size, the sensor can be designed for sub-millimeter range as well. The sub-millimeter range is particularly suitable for sensing (bio)chemicals in aqueous solutions. This is because the dielectric constant of water decreases in sub-millimeter range. Hence, the spread of the electromagnetic field inside the solution reduces, and the loss due to the water becomes tolerable.

APPENDICES

Appendix A

Analysis of one-dimensional multilayer optical waveguides based on wave-transfer model

In a multilayer optical waveguide consisting of N thin layers, shown in Fig. A.1, the electromagnetic field in each layer can be expressed as the sum of two plane waves propagating in counter-direction (forward and backward) along the z axis. For a guided mode, the fields decay exponentially away from the topmost and bottommost interfaces.

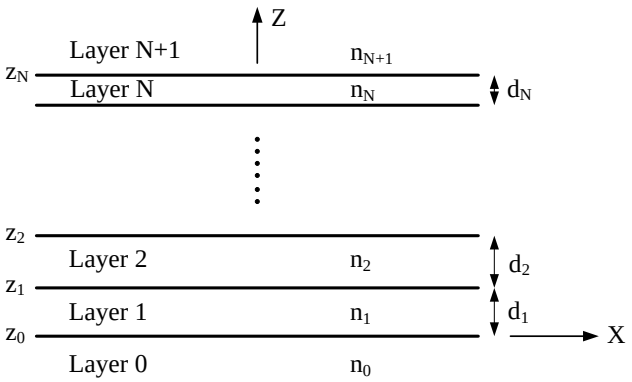

Figure A.1: A multilayer optical waveguide.

In wave-transfer model [150], the wave reflection and transmission at each planar interface are described by a wave-transfer matrix, relating the forward and backward fields on one side of the interface to those on the other side. Moreover, the phase change of the fields propagating inside the layers is represented by a

propagation matrix. Cascading wave-transfer and propagation matrices provides a convenient way of modelling a multilayer waveguide with an arbitrary number of layers.

Two types of guided modes are supported in a multilayer optical waveguide, i.e. transverse electric, TE, and transverse magnetic, TM. Referring to Fig. A.1, TE modes have E_x, H_y and H_z field components whereas TM modes have H_x, E_y and E_z. The continuity of tangential fields at an interface located at $z = z_j$ $(0 \leq j \leq N)$ for TE and TM modes can be represented in the matrix form as follow

$$\begin{bmatrix} E_{j+1}^{+}(z_j) \\ \\ E_{j+1}^{-}(z_j) \end{bmatrix} = \begin{bmatrix} \dfrac{Z_j^{TE} + Z_{j+1}^{TE}}{2Z_j^{TE}} & \dfrac{Z_j^{TE} - Z_{j+1}^{TE}}{2Z_j^{TE}} \\ \\ \dfrac{Z_j^{TE} - Z_{j+1}^{TE}}{2Z_j^{TE}} & \dfrac{Z_j^{TE} + Z_{j+1}^{TE}}{2Z_j^{TE}} \end{bmatrix} \begin{bmatrix} E_j^{+}(z_j) \\ \\ E_j^{-}(z_j) \end{bmatrix} \tag{A.1a}$$

$$\begin{bmatrix} H_{j+1}^{+}(z_j) \\ \\ H_{j+1}^{-}(z_j) \end{bmatrix} = \begin{bmatrix} \dfrac{Z_{j+1}^{TM} + Z_j^{TM}}{2Z_{j+1}^{TM}} & \dfrac{Z_{j+1}^{TM} - Z_j^{TM}}{2Z_{j+1}^{TM}} \\ \\ \dfrac{Z_{j+1}^{TM} - Z_j^{TM}}{2Z_{j+1}^{TM}} & \dfrac{Z_{j+1}^{TM} + Z_j^{TM}}{2Z_{j+1}^{TM}} \end{bmatrix} \begin{bmatrix} H_j^{+}(z_j) \\ \\ H_j^{-}(z_j) \end{bmatrix} \tag{A.1b}$$

where $E_j^{+}(.)$ and $E_j^{-}(.)$ (subscript j refers to layer j in Fig. A.1) denote the complex amplitude of the electric field propagating in $+z$ and $-z$ directions, respectively, $H_j^{+}(.)$ and $H_j^{-}(.)$ represent the complex amplitude of the magnetic field propagating in $+z$ and $-z$ directions, respectively, and Z_j^{TE} and Z_j^{TM} are the characteristic impedances for TE and TM modes, respectively, and are given by

$$Z_j^{TE} = \frac{\omega\mu_0}{k_{zj}} \tag{A.2a}$$

$$Z_j^{TM} = \frac{k_{zj}}{\omega\epsilon_0\epsilon_{rj}} \tag{A.2b}$$

$$k_{zj} = \begin{cases} \sqrt{k_j^2 - \beta^2} & : \beta \leq k_j \\ -j\sqrt{\beta^2 - k_j^2} & : \beta > k_j \end{cases} \tag{A.2c}$$

In (A.2), ω is the angular frequency, μ_0 and ϵ_0 are permeability and permittivity of free-space, respectively, ϵ_{rj} is the relative permittivity of the j^{th} layer, k_j is the wave number in the same layer, and β is the propagation of the guided mode.

In fact, the 2×2 matrices in (A.1) are defined as wave-transfer matrices, $\mathbf{M}_j$, at the interface $z = z_j$ for TE and TM modes. The propagation matrix in layer j $(1 \leq j \leq N)$ is given by

$$\mathbf{P}_j = \begin{bmatrix} e^{-jk_{zj}h_j} & 0 \\ 0 & e^{+jk_{zj}h_j} \end{bmatrix} \tag{A.3}$$

where h_j is the hight of layer j. It is noted that the propagation matrix has the same form for TE and TM modes.

To solve for the propagation constant, or effective index, of a guided mode in the multilayer waveguide, the appropriate wave-transfer and propagation matrices need to be cascaded. With reference to Fig. A.1, the complete matrix equation enforcing all of the boundary conditions is given by

$$\begin{bmatrix} E_{N+1}^{+}(z_N) \\ 0 \end{bmatrix} = \mathbf{M}_N\mathbf{P}_N...\mathbf{M}_1\mathbf{P}_1\mathbf{M}_0 \begin{bmatrix} 0 \\ E_0^{-}(z_0) \end{bmatrix} \tag{A.4}$$

In (A.4), the incoming waves in half space regions, i.e. E_{N+1}^{-} and E_0^{+}, are identically set to zero for a guided mode. Assuming the field amplitudes are normalized such that $E_0^{-}(z_0) = 1$, then the matrix equation simplifies to

$$\begin{bmatrix} E_{N+1}^{+}(z_N) \\ 0 \end{bmatrix} = \begin{bmatrix} MP_{11}(\beta) & MP_{12}(\beta) \\ MP_{21}(\beta) & MP_{22}(\beta) \end{bmatrix} \begin{bmatrix} 0 \\ 1 \end{bmatrix} \tag{A.5}$$

From (A.5), the characteristic equation from which the propagation constant, β, and consequently the effective, n_{eff}, are obtained is given by

$$MP_{22}(\beta) = 0 \tag{A.6}$$

$$n_{eff} = \frac{\beta}{k_0} \tag{A.7}$$

where $k_0 = \frac{\omega}{c_0}$ is the wave number in free space. After determining the effective index of the mode, the field profile can be calculated using the now known wave-transfer and propagation matrices.

A.1 Fill Factor

The fill factor of the mode in any layer is defined as the fraction of the total power in that layer, and can be calculated as

$$FF = \frac{P_j}{P_{tot}} = \begin{cases} \dfrac{\int_{z_{j-1}}^{z_j} |E_x|^2 \mathrm{d}z}{\int_{-\infty}^{+\infty} |E_x|^2 \mathrm{d}z} & : \text{TE mode} \\ \dfrac{\int_{z_{j-1}}^{z_j} \frac{1}{\epsilon_{ab}} |H_x|^2 \mathrm{d}z}{\int_{-\infty}^{+\infty} \frac{1}{\epsilon_j} |H_x|^2 \mathrm{d}z} & : \text{TM mode} \end{cases} \tag{A.8}$$

where P_{tot} and P_j are the total optical power and the power confined in layer j, respectively.

A.2 Effective Absorption Coefficient

Assuming one of the layers in Fig. A.1 is made of a photoabsorbing material, e.g. LTG GaAs, the effective index becomes a complex number whose imaginary part relates to the field attenuation constant. The power absorption coefficient is obtained by doubling the field attenuation constant. To find the complex effective index, a more rigorous approach is to use a complex dielectric permittivity for the photoabsorbing layer, and solve the effective index problem with complex numbers. Here, a second approach which is much simpler with reasonable accuracy is discussed. For illustration, consider a mode propagating in the y direction. The mode is partly in the absorbing region. Assuming the absorption is small such that the mode does not change substantially by propagating a short incremental distance δy, and $P_{tot}(y)$ denotes the total power at point y, the total power at point $y + \delta y$ is given by

$$P_{tot}(y + \delta y) = FF.P_{tot}(y)e^{-\alpha \delta y} + (1 - FF)P_{tot}(y) \tag{A.9}$$

where FF is the photoabsorber fill factor, and α is the bulk power absorption coefficient of the photoabsorbing material. Dividing both sides of (A.9) by δy, rearranging the terms and letting $\delta y \to 0$ yields a first-order ordinary differential equation for $P_{tot}(y)$ as

$$\frac{\mathrm{d}P_{tot}(y)}{\mathrm{d}y} = -\alpha.FF.P_{tot}(y) \tag{A.10}$$

Knowing the total optical power at $y = 0$, the total power at any other point along the propagation path is readily obtained from

$$P_{tot}(y) = P_{tot}(0)e^{-\alpha_e y} \tag{A.11a}$$

$$\alpha_e = FF.\alpha \tag{A.11b}$$

From (A.11), when a mode is partially confined in a photoabsorbing region, the effective absorption coefficient, α_e, can be determined by multiplying the bulk absorption coefficient of the photoabsorbing material, α, by the mode's fill factor in the photoabsorber, FF. From effective absorption coefficient one can define the absorption length, l_{ab}, as a length after which the optical power drops off by a factor of e^{-1}.

$$l_{ab} = \frac{1}{\alpha_e} = \frac{1}{FF.\alpha} \tag{A.12}$$

Appendix B

Dispersion Relation for a Radially Inhomogeneous Dielectric Cylinder

The dispersion relation for a radially inhomogeneous dielectric cylinder is obtained by setting the determinant of a 4×4 matrix equal to zero [138]

$$\det \begin{bmatrix} c_1(r_1) & 0 & -M_{11} & -M_{13} \\ 0 & d_1(r_1) & -M_{21} & -M_{23} \\ e_1(r_1) & f_1(r_1) & -M_{31} & -M_{33} \\ g_1(r_1) & h_1(r_1) & -M_{41} & -M_{43} \end{bmatrix} = 0 \tag{B.1}$$

where

$$M = M_2(r_1) M_2^{-1}(r_2) M_3(r_2)$$

$$M_2(r) = \begin{bmatrix} c_2(r) & c_2'(r) & 0 & 0 \\ 0 & 0 & d_2(r) & d_2'(r) \\ e_2(r) & e_2'(r) & f_2(r) & f_2'(r) \\ g_2(r) & g_2'(r) & h_2(r) & h_2'(r) \end{bmatrix}$$

$$M_3(r) = \begin{bmatrix} s(r) & 0 & 0 & 0 \\ 0 & 0 & \tau(r) & 0 \\ u(r) & 0 & v(r) & 0 \\ w(r) & 0 & \chi(r) & 0 \end{bmatrix}$$

$$
\begin{array}{llll}
c_i(r) = & J_m(k_{\rho i}r) & d_i(r) = & \eta J_m(k_{\rho i}r) \\
e_i(r) = & \frac{k_z m}{k_{\rho i}^2 r} J_m(k_{\rho i}r) & f_i(r) = & \frac{jk_0\eta}{k_{\rho i}} J'_m(k_{\rho i}r) \\
g_i(r) = & -\frac{jk_0\varepsilon_{ri}}{k_{\rho i}} J'_m(k_{\rho i}r) & h_i(r) = & \frac{\eta k_z m}{k_{\rho i}^2 r} J_m(k_{\rho i}r) \\
s\,(r) = & K_m(\alpha_\rho r) & \tau\,(r) = & \eta K_m(\alpha_\rho r) \\
u\,(r) = & -\frac{k_z m}{\alpha_\rho^2 r} K_m(\alpha_\rho r) & v\,(r) = & -\frac{jk_0\eta}{\alpha_\rho} K'_m(\alpha_\rho r) \\
w\,(r) = & \frac{jk_0}{\alpha_\rho} K'_m(\alpha_\rho r) & \chi\,(r) = & -\frac{\eta k_z m}{\alpha_\rho^2 r} K_m(\alpha_\rho r) \\
k_{\rho i} = & \sqrt{k_0^2\varepsilon_{ri} - k_z^2} & \alpha_\rho = & \sqrt{k_z^2 - k_0^2}
\end{array}
$$

where i=1 and 2 refers to the regions identified by ε_{rs} and ε_{rd} in Fig. 5.2(c), respectively, and $\eta = \sqrt{\frac{\mu_0}{\varepsilon_0}}$ is the free space impedance. The expressions for $c'_i - h'_i$ is the same as the unprimed $c_i - h_i$ expressions except that the Bessel function of the first kind, $J_m(.)$, is replaced by the Bessel function of the second kind, $Y_m(.)$. It is notable that when $r_2 = r_1$, the dispersion equation (B.1) is reduced to (5.3).

References

[1] M. Nagel, M. Först and H. Kurz, "THz biosensing devices: fundamentals and technology," *Journal of Physics: Condensed Matter*, vol. 18, pp. 601–618, April 2006. 1, 65

[2] P. H. Siegel, "Terahertz Technology in Biology and Medicine," *IEEE Trans. Microwave Theory Tech.*, vol. 52, no. 10, pp. 2438–2447, 2004.

[3] T. W. Crowe, T. Globus, D. L. Woolard, and J. L. Hesler, "Terahertz sources and detectors and their application to biological sensing," *Phil. Trans. R. Soc. A*, vol. 362, no. 1815, pp. 365–377, 2004.

[4] T. Globus, D. Woolard, M. Bykhovskaia, B. Gelmont, L. Werbos, and A. Samuels, "THz-frequency spectroscopic sensing of DNA and related biological materials," *International Journal of High Speed Electronics and Systems*, vol. 13, no. 4, pp. 903–936, 2003.

[5] M. R. Scarfi, M. Romano, R. Dipietro, O. Zeni, A. Doria, G. P. Gallerano, E. Giovenale, G. Messina, A. Lai, G. Campurra, D. Coniglio, and M. D'Arienzo, "THz Exposure of Whole Blood for the Study of Biological Effects on Human Lymphocytes," *J. Biol. Phys.*, vol. 29, pp. 171–175, 2003.

[6] S. W. Smye, J. M. Chamberlain, A. J. Fitzgerald, and E. Berry, "The interaction between terahertz radiation and biological tissue," *Phys. Med. Biol.*, vol. 46, pp. R101–R112, 2001. 1

[7] S. M. Kim, F. Hatami, and J. S. Harris, "Biomedical terahertz imaging with a quantum cascade laser," *Appl. Phys. Lett.*, vol. 88, 153903, April 2006. 1, 65

[8] P. F. Taday, "Applications of terahertz spectroscopy to pharmaceutical sciences," *Phil. Trans. R. Soc. A*, vol. 362, no. 1815, pp. 351–364, 2004. 1, 5, 65

[9] V. P. Wallace, P. F. Taday, A. J. Fitzgerald, R. M. Woodward, J. Cluff, R. J. Pye, and D. D. Arnone, "Terahertz pulsed imaging and spectroscopy for biomedical and pharmaceutical applications ," *Faraday Discuss.*, vol. 126, pp. 255–263, 2004. 1

[10] N. Karpowicz, H. Zhong, C. Zhang, K.-I. Lin, J.-S. Hwang, J. Xu, and X.-C. Zhang, "Compact continuous-wave subterahertz system for inspection applications," *Appl. Phys. Lett.*, vol. 86, no. 5, pp. 54 105–3, 2005. 1

[11] M. K. Choi, A. Bettermann, and D. W. Van Der Weide, "Potential for detection of explosive and biological hazards with electronic terahertz systems," *Phil. Trans. R. Soc. A*, vol. 362, no. 1815, pp. 337–349, 2004.

[12] M. C. Kemp, P. F. Taday, B. E. Cole, J. A. Cluff, A. J. Fitzgerald, and W. R. Tribe, "Security applications of terahertz technology," in *The Proceedings of SPIE Conference*, vol. 5070, August 2003, pp. 44–52.

[13] D. Woolard, R. Kaul, R. Suenram, A. Hight Walker, T. Globus, and A. Samuels, "Terahertz Electronics for Chemical and Biological Warfare Agent Detection," in *IEEE MTT-S Int. Microwave Symp. Dig.*, 1999, pp. 925–928. 1

[14] R. Piesiewicz, J. Jemaia, M. Kochb, T. Krnera, "THz channel characterization for future wireless gigabit indoor communication systems," in *The Proceedings of SPIE Conference*, vol. 5727, March 2005, pp. 166–176. 1, 2

[15] T. Nagatsuma, "Millimeter-Wave Photonic Technologies for Communications and Sensor Applications," *in New Photonics Technologies for the Information Age: The Dream of Ubiquitous Services*, pp. 193–212, ed. by S. Sudo and K. Okamoto (Artech House, 2004).

[16] C. M. Mann, "Towards Terahertz Communications Systems," *in Terahertz Sources and Systems*, pp. 261–267, ed. by R. E. Miles, P. Harrison, and D. Lippens (Kluwer Academic Publisher, Printed in the Netherlands, 2001).

[17] A. Hirata, H. Ishii, and T. Nagatsuma, "Design and characterization of a 120-GHz millimeter-wave antenna for integrated photonic transmitters," *The Proceedings of International Topical Meeting on Microwave/Photonics*, pp. 229–232, 2000.

[18] D. Steer, G. Dolman, and P. Row, "Radio system design for broadband residential access," in *IEEE Radio and Wireless Conference*, Aug. 1999, pp. 31–34. 1

[19] A. Rudolph, J. Simpson, M. Haas, E. Erickson, and M. Fich, "Far-infrared abundance measurements in the outer galaxy," *Astrophysical Journal*, vol. 489, pp. 94–101, November 1997. 1

[20] M. Wiedner, et al., "First observations with CONDOR, a 1.5 thz heterodyne receiver," *Astronomy & Astrophysics*, vol. 454, pp. L33–L36, May 2006. 1

[21] B. M. Fischer, M. Walther, and P. Uhd Jepsen, "Far-infrared vibrational modes of DNA components studied by terahertz time-domain spectroscopy," *Phys. Med. Biol.*, vol. 47, pp. 3807–3814, October 2002. 1, 5, 65, 74

[22] X. Song, and B. I. Swanson, "Direct, Ultrasensitive, and Selective Optical Detection of Protein Toxins Using Multivalent Interactions," *Anal. Chem.*, vol. 71, pp. 2097–2107, June 1999. 4

[23] J. G. Guan, Y. Q. Miao, and Q. J. Zhang, "Impedimetric Biosensors," *Journal of Bioscience and Bioengineering*, vol. 97, no. 4, pp. 219–226, 2004. 4

[24] D. Woolard, W. Loerop, and M. Shur, Ed., *"Terahertz Sensing Technology: Emerging Scientific Applications and Novel Device Concepts"*. World Scientific Publishing Co., 2003, vol. 2. 4

[25] B. Fischer et al., "Terahertz time-domain spectroscopy and imaging of artificial rna," *Opt. Express*, vol. 13, no. 14, pp. 5205–5215, July 2005. 5

[26] M. He, A. Azad, S. Ye, and W. Zhang, "Far-infrared signature of animal tissues characterized by terahertz time-domain spectroscopy," *Optics Communications*, vol. 259, pp. 389–392, August 2006. 5

[27] N. Nagai, R. Kumazawa, and R. Fukasawa, "Direct evidence of intermolecular vibrations by THz spectroscopy," *Chem. Phys. Lett.*, vol. 413, pp. 495–500, August 2005. 5

[28] R. M. Woodward, V. P. Wallace, R. J. Pye, B. E. Cole, D. D. Arnone, E. H. Linfield, and M. Pepper, "Terahertz Pulse Imaging of ex vivo Basal Cell Carcinoma," *The Journal of Investigative Dermatology*, vol. 120, no. 1, pp. 72–78, January 2003. 5

[29] H. Hirori, K. Yamashita, M. Nagai, and K. Tanaka, "Attenuated total reflection spectroscopy in time domain using terahertz coherent pulses," *Jpn J. Appl. Phys.*, vol. 43, no. 10A, pp. L1287–L1289, September 2004. 6

[30] M. Nagel, P. Haring Bolivar, M. Brucherseifer, H. Kurz, A. Bosserhoff, and R. Büttner, "Integrated THz technology for label-free genetic diagnostics," *Appl. Phys. Lett.*, vol. 80, no. 1, pp. 154–156, January 2002. 6, 8, 66

[31] J. Baker-Jarvis, E. Vanzura, and W. Kissick, "Improved technique for determining complex permittivity with the transmission/reflection method," *IEEE Trans. Microwave Theory Tech.*, vol. 38, no. 8, pp. 1096–1103, August 1990. 6

[32] A.-H. Boughriet, C. Legrand, and A. Chapoton, "Noniterative stable transmission/reflection method for low-loss material complex permittivity determination," *IEEE Trans. Microwave Theory Tech.*, vol. 45, no. 1, pp. 52–57, January 1997. 6

[33] T. Ohkubo, M. Onuma, J. Kitagawa, and Y. Kadoyab, "Micro-strip-line-based sensing chips for characterization of polar liquids in terahertz regime," *Appl. Phys. Lett.*, vol. 88, 212511, May 2006. 7

[34] C. Rau, G. Torosyan, R. Beigang, and Kh. Nerkararyan, "Prism coupled terahertz waveguide sensor," *Appl. Phys. Lett.*, vol. 86, 211119, May 2005. 7

[35] H. Kurta and D. S. Citrinb, "Photonic crystals for biochemical sensing in the terahertz region," *Appl. Phys. Lett.*, vol. 87, 041108, July 2005. 7, 66

[36] M. Neshat, H. Chen, S. Gigoyan, D. Saeedkia, and S. Safavi-Naeini, "Dielectric measurement of small volume liquid samples using dielectric image guide in mm-wave range," in *33rd International Conference on Infrared, Millimeter and Terahertz Waves*, September 2008. 7

[37] L. Chen, C. Ong, C. Neo, V. V. Varadan, and V. K. Varadan, *Microwave Electronics: Measurement and Material Characterization.* John Wiley and Sons, 2004. 8, 82

[38] M. P. Abegaonkar, R. N. Karekar, and R. C. Aiyer, "A microwave microstrip ring resonator as a moisture sensor for biomaterials: application to wheat grains," *Meas. Sci. Technol.*, vol. 10, pp. 195–200, December 1999. 8, 107

[39] M. Nagel, F. Richter, P. Haring Bolivar, and H. Kurz, "A functionalized THz sensor for marker-free DNA analysis," *Phys. Med. Biol.*, vol. 48, pp. 3625–3636, October 2003. 8, 75, 107

[40] F. Stewing, T. Kleine-Ostmann, and M. Koch, "A new class of improved-efficiency THz filters for on-chip detection of biomaterials," *Microw. Opt. Technol. Lett.*, vol. 41, no. 2, pp. 79–82, April 2004. 8, 66

[41] S. Harsha, N. Laman, and D. Grischkowsky, "High-Q terahertz Bragg resonances within a metal parallel plate waveguide," *Appl. Phys. Lett.*, vol. 94, 091118, March 2009. 8

[42] C. Debusa and P. Bolivar, "Frequency selective surfaces for high sensitivity terahertz sensing," *Appl. Phys. Lett.*, vol. 91, 184102, 2007. 8

[43] A. Arbabi, A. Rohani, D. Saeedkia, S. Safavi-Naeini, "A terahertz plasmonic metamaterial structure for near-field sensing applications," in *33rd International Conference on Infrared, Millimeter and Terahertz Waves*, September 2008. 8

[44] F. Vollmer and S. Arnold, "Whispering-gallery-mode biosensing: label-free detection down to single molecules," *Nature Methods*, vol. 5, no. 7, pp. 591–596, July 2008. 8

[45] J. Krupka, D. Mouneyrac, J. G. Hartnett, and M. E. Tobar, "Use of Whispering-Gallery Modes and Quasi-TE0np Modes for Broadband Characterization of Bulk Gallium Arsenide and Gallium Phosphide Samples," *IEEE Trans. Microwave Theory Tech.*, vol. 56, no. 5, pp. 1201–1206, May 2008. 9

[46] G. Annino, D. Bertolini, M. Cassettari, M. Fittipaldi, I. Longo, and M. Martinelli, "Dielectric properties of materials using whispering gallery dielectric resonators: Experiments and perspectives of ultra-wideband characterization," *J. Chem. Phys.*, vol. 112, no. 5, pp. 2308–2314, February 2000. 9

[47] Y. Kogami, H. Tamura, and K. Matsumura, "Characterization of Low Loss Dielectric Materials in Millimeter Wave Region Using a Whispering Gallery Mode Resonator," in 13^{th} *Int. Conference on Microwave, Radar and Wireless Comunications*, May 2000, pp. 340–343. 9

[48] S. Arnold, R. Ramjit, D. Keng, V. Kolchenko, and I. Teraoka, "MicroParticle photophysics illuminates viral bio-sensing," *Faraday Discuss.*, vol. 137, no. 4, pp. 1–19, April 2007. 9

[49] J. Yang and L. J. Guo, "Optical Sensors Based on Active Microcavities," *IEEE J. Sel. Top. Quantum Electron.*, vol. 12, no. 1, pp. 143–147, January/February 2006. 9

[50] R. W. Boyd and J. E. Heebner, "Sensitive disk resonator photonic biosensor," *Applied Optics*, vol. 40, no. 31, pp. 5742–5747, November 2001. 9, 96

[51] M. C. Teich, "Field-Theoretical Treatment of Photomixing," *Appl. Phys. Lett.*, vol. 14, no. 6, pp. 201–203, 1969. 10

[52] I. S. Gregory, C. Baker, W. R. Tribe, I. V. Bradley, M. J. Evans, E. H. Linfield, A. G. Davies, and M. Missous, "Optimization of Photomixers and Antennas for Continuous-Wave Terahertz Emission," *IEEE J. Quantum Elec.*, vol. 41, no. 5, pp. 717–728, 2005. 10

[53] D. Saeedkia and S. Safavi-Naeini, "A Comprehensive Model for Photomixing in Ultrafast Photoconductors," *IEEE Photonics Technol. Lett.*, vol. 18, no. 13, pp. 1457–1459, July 2006. 10

[54] D. Saeedkia, R. R. Mansour, and S. Safavi-Naeini, "Modeling and Analysis of High-Temperature Superconductor Terahertz Photomixers," *IEEE Trans. Appl. Superconduct.*, vol. 15, no. 3, September 2005. 10

[55] S. Verghese, K. A. McIntosh, S. Calawa, W. F. Dinatale, E. K. Duerr, and K. A. Molvar, "Generation and detection of coherent terahertz waves using two photomixers," *Appl. Phys. Lett.*, vol. 73, no. 26, pp. 3824–3826, December 1998. 10

[56] E. A. Michael, "Travelling-wave photonic mixers for increased continuous-wave power beyond 1 THz," *Semicond. Sci. Technol.*, vol. 20, pp. 164–177, June 2005. 10

[57] D. Saeedkia, S. Safavi-Naeini, and R. R. Mansour, "The intraction of laser and photoconductor in a continuous-wave terahertz photomixer," *IEEE J. Quantum Elec.*, vol. 41, no. 9, pp. 1188–1196, September 2005. 10, 12, 45

[58] S. Verghese, K. A. McIntosh and E. R. Brown, "Optical and terahertz power limits in the low-temperature-grown GaAs photomixers," *Appl. Phys. Lett.*, vol. 71, no. 19, pp. 2743–2745, 1997. 11

[59] M. Y. Frankel, S. Gupta, J. A. Valdmanis, and G. A. Mourou, "Terahertz Attenuation and Dispersion Characteristics of Coplanar Transmission Lines,"

IEEE Trans. Microwave Theory Tech., vol. 39, no. 6, pp. 910–916, June 1991. 11

[60] T. Mandviwala, B. Lail, and G. Boreman, "Coplanar striplines for THz frequencies: Design, fabrication and measurements," in *IEEE Antennas and Propagation Society International Symposium*, vol. 1A, 2005, pp. 284–287. 11

[61] D. Pasqualini, A. Neto, and R. A. Wyss, "Distributed sources on coplanar waveguides: application to photomixers for THz local oscillators," *Microw. Opt. Technol. Lett.*, vol. 33, no. 6, pp. 430–435, 2002. 12, 45, 55

[62] E. R. Brown, "A photoconductive model for superior GaAs THz photomixer," *Appl. Phys. Lett.*, vol. 75, no. 6, pp. 769–771, 1999. 12, 16

[63] D. Saeedkia and S. Safavi-Naeini, "Modeling and Analysis of a Multilayer Dielectric Slab Waveguide with Applications in Edge-Coupled Terahertz Photomixer Sources," *Journal of Lightwave Technology*, vol. 25, no. 1, pp. 432–439, January 2007. xi, 13, 14, 15, 26, 46, 67

[64] Y. Kokubo and I. Ohta, "Refractive index as a function of photon energy for algaas between 1.2 and 1.8 ev," *J. Appl. Phys.*, vol. 81, no. 4, pp. 2042–2043, February 1997. 14

[65] T. Tamir, Ed., *Guided-Wave Optoelectronics*, 2nd ed. Springer-Verlag, 1990, page 321. 14

[66] R. M. Knox and P. P. Toulios, "Integrated circuits for the millimeter through optical frequency range," in *Proc. Symp. Submillimeter Waves (Polytechnic Press, Brooklyn)*, 1970, pp. 497–516. 16

[67] R. Scarmozzino, A. Gopinath, R. Pregla, and S. Helfert, "Numerical techniques for modeling guided-wave photonic devices," *IEEE J. Sel. Top. Quantum Electron.*, vol. 6, no. 1, pp. 150–162, January/February 2000. 20

[68] BeamPROP. Rsoft Design Group. [Online]. Available: http://www.rsoftdesign.com/ 20, 21

[69] A. Reklaitis, "Monte carlo analysis of terahertz oscillations of photoexcited carriers in GaAs p-i-n structures," *Phys. Rev. B*, vol. 74, pp. 165 305–1–9, October 2006. 22

[70] A. W. Smith and K. F. Brennan, "Hydrodynamic simulation of semiconductor devices," *Prog. Quant. Electr.*, vol. 21, no. 4, pp. 293–360, 1998. 22

[71] D. Pasalic and R. Vahldieck, "A hybrid drift-diffusion-TLM analysis of traveling-wave photodetectors," *IEEE Trans. Microwave Theory Tech.*, vol. 53, no. 9, pp. 2700–2706, September 2005. 22

[72] S. Selberherr, *Analysis and Simulation of Semiconductor Devices.* Wien, Austria: Springer-Verlag, 1984. 23, 24, 25, 26, 28

[73] M. R. Melloeh, J. M. Woodall, E. S. Harmon, N. Otsuka, F. H. Pollak, D. D. Nolte, R. M. Feenstra, and M. A. Lutz, "Low-temperature grown III-V materials," *Annu. Rev. Mater. Sci.*, vol. 25, pp. 547–600, 1995. 24

[74] E. Brown, *Terahertz Sensing Technology: Electronic Devices and Advanced Systems Technology.* World Scientific Publishing Co., 2003, vol. 1, ch. Terahertz Generation by Photomixing in Ultrafast Photoconductors. 29

[75] D. Saeedkia, "Modeling and design of photoconductive and superconductive terahertz photomixer sources," Ph.D. dissertation, University of Waterloo, 2005. 29, 30

[76] Taurus Medici. Synopsys. [Online]. Available: http://www.synopsys.com 30

[77] N. Zamdmer, Q. Hu, K. A. McIntosh, and S. Verghese, "Increase in response time of low-temperature-grown GaAs photoconductive switches at high voltage bias," *Appl. Phys. Lett.*, vol. 75, no. 15, pp. 2313–2315, 1999. 30, 32

[78] T. Rozzi and M. Mongiardo, *Open electromagnetic waveguides*, ser. IEE Electromagnetic Waves Series 43. The Institution of Electrical Engineers, 1997. 33, 57

[79] Y. D. Lin, J. W. Sheen, and C. Y . Chang, "Surface-wave leakage properties of coplanar strips," in *IEEE Microwave Theory Tech. Symp. Dig.*, vol. 1, May 1995, pp. 229–232. 33

[80] H. Shigesawa, M. Tsuji and A. A. Oliner, "Dominant mode power leakage from printed-circuit waveguides," *Radio Science*, vol. 26, no. 2, pp. 559–564, March-April 1991. 33

[81] S. A. Shah, A. Zeng, M. K. Jackson, L. Pouliot, A. Lecours and J. F. Currie, "Guided surface waves in photoconductive excitation," *IEEE Microwave and Guided Wave Letters*, vol. 6, no. 9, pp. 309–311, September 1996. 33

[82] J. Nees, S. Williamson, and G. Mourou, "100 GHz travelling-wave electro-optic phase modulator," *Appl. Phys. Lett.*, vol. 54, pp. 1962–1964, May 1989. 34

[83] U. D. Keil, D. R. Dykaar, A. F. J. Levi, R. F. Kopf, L. N. Pfeiffer, S. B. Darack, K. W. West, "High-speed coplanar transmission lines," *IEEE J. of Quantum Electron.*, vol. 28, no. 10, pp. 2333–2342, October 1992. 34

[84] H. Cheng, J. F. Whitaker, T. M. Weller, and L. P. B. Katehi, "Terahertz-bandwidth pulse propagation on a coplanar stripline fabricated on a thin membrane," *IEEE Microwave and Guided Wave Letters*, vol. 4, no. 3, pp. 89–91, March 1994. 34

[85] T. Itoh, Ed., *Numerical Techniques for Microwave and Millimeter-wave Passive Structure*. John Wiley & Sons, 1989, ch. Transverse resonance technique. 34

[86] K. A. Michalski and J. R. Mosig, "Multilayered media greens functions in integral equation formulations," *IEEE Trans. Antennas Propagat.*, vol. 45, no. 3, pp. 508–519, March 1997. 34

[87] Jianming Jin, *The Finite Element Method in Electromagnetics*, 2nd ed. John Wiley and Sons, 2002. 39, 40

[88] T. B. A. Senior and J. L. Volakis, *Approximate boundary conditions in electromagnetics*. IEE press, 1995. 40, 73

[89] A. Taflove and M. E. Brodwin, "Numerical solution of steady-state electromagnetic scattering problems using the time-dependant maxwells equations," *IEEE Trans. Microwave Theory Tech.*, vol. 23, no. 8, pp. 623–630, August 1975. 41

[90] R. Holland, "THREDE: A free-field EMP coupling and scattering code," *IEEE Trans. Nucl. Sci.*, vol. 24, pp. 2416–2421, 1977. 41

[91] J. P. Berenger, *Perfectly Matched Layer (PML) for Computational Electromagnetics*. Morgan & Claypool, 2007. 41

[92] O. M. Ramahi, "Complementary operators: A method to annihilate artificial reflections arising from the truncation of the computational domain in the solution of partial differential equations," *IEEE Trans. Antennas Propagat.*, vol. 43, no. 7, pp. 697–704, July 1995. 41

[93] W. P. Huang, C. L. Xu, W. Lui, K. Yokoyama, "The perfectly matched layer boundary condition for modal analysis of optical waveguides: leaky mode calculations," *IEEE Photonics Technology Letters*, vol. 8, no. 5, pp. 652–654, May 1996. 41

[94] S. Selleri, L. Vincetti, M. Zoboli, "Truncation of finite-element mesh for modal analysis of dielectric waveguides," *Microw. Opt. Technol. Lett.*, vol. 32, no. 3, pp. 178 –182, December 2001.

[95] H. E. Hernandez-Figueroa, F. A. Fernandez, J. B. Davies, "Finite element approach for the modal analysis of open-boundary waveguides," *Electronics Letters*, vol. 30, no. 24, pp. 2031–2032, November 1994. 41

[96] HFSS 10.1. Ansoft Corporation. [Online]. Available: http://www.ansoft.com 41

[97] COMSOL 3.5a. COMSOL AB. [Online]. Available: http://www.comsol.com 41

[98] M. Ordal, L. Long, R. Bell, S. Bell, R. Bell, R. Alexander, and C. Ward, "Optical properties of the metals Al, Co, Cu, Au, Fe, Pb, Ni, Pd, Pt, Ag, Ti, and W in the infrared and far infrared," *Applied Optics*, vol. 22, no. 7, pp. 1099–1120, April 1983. 43

[99] S. Ichikawa, "Analysis of transmission lines with distributed sources," *Electron. Commun. Jpn.*, vol. 69 (Part I: Commun.), no. 2, pp. 57–65, 1986. 45

[100] F. Mesa, C. Di Nallo, and D. R. Jackson, "The theory of surface-wave and space-wave leaky mode excitation on microstrip lines," *IEEE Trans. Microwave Theory Tech.*, vol. 47, no. 2, pp. 207–215, February 1999. 45

[101] M. Neshat, D. Saeedkia, and S. Safavi-Naeini, "Semi-analytical calculation of terahertz signal generated from photocurrent radiation in traveling-wave photonic mixers," *Int. J. Infrared Milli. Waves*, vol. 29, no. 9, pp. 809–822, September 2008. 45

[102] P. Bernardi and R. Cicchetti, "Response of a planar microstrip line excited by an external electromagnetic field," *IEEE Trans. Electromag. Compat.*, vol. 32, no. 2, pp. 98–105, May 1990. 46

[103] L. B. Felsen and N. Marcuvitz, *Radiation and Scattering of Waves.* IEEE Press, 1994. 47, 49

[104] M. I. Aksun and R. Mittra, "Derivation of Closed-Form Greens Functions for a General Microstrip Geometry," *IEEE Trans. Microwave Theory Tech.*, vol. 40, no. 11, pp. 2055–2062, November 1992. 47, 48

[105] N. Hojjat, S. Safavi-Naeini and Y. L. Chow, "Numerical computation of complex image Greens functions for multilayer dielectric media: near-field zone and the interface region," *IEE Proc.-Microw. Antennas Propag.*, vol. 145, no. 6, pp. 449–454, December 1998. 47, 48

[106] W. C. Chew, *Waves and Fields in Inhomogeneous Media*. Van Nostrand Reinhold, New York, 1990. 48

[107] R. E. Collin, *Field Theory of Guided Waves*, 2nd ed. IEEE Press, 1990. 51, 55, 57, 58, 68

[108] S. Matsuura, G. A. Blake, R. A. Wyss, J. C. Pearson, C. Kadow, A. W. Jackson, and A. C. Gossard, "A traveling-wave THz photomixer based on angle-tuned phase matching," *Appl. Phys. Lett.*, vol. 74, no. 19, pp. 2872–2874, 1999. 55

[109] T. Rozzi and G. Cerri, "Radiation modes of open microstrip with applications," *IEEE Trans. Microwave Theory Tech.*, vol. 43, no. 6, pp. 1364–1370, June 1995. 55, 57

[110] E. Bottcher and D. Bimberg, "Millimeter wave distributed metal-semiconductor-metal photodetectors," *Appl. Phys. Lett.*, vol. 66, no. 26, pp. 3648–3650, June 1995. 60

[111] E. A. Michael, B. Vowinkel, R. Schieder, M. Mikulics, M. Marso, and P. Kordos, "Large-area traveling-wave photonic mixers for increased continuous terahertz power," *Appl. Phys. Lett.*, vol. 86, no. 11, pp. 111 120–3, 2005. 62

[112] M. Tonouchi, "Cutting-edge terahertz technology," *Nature Photonics*, vol. 1, pp. 97–105, February 2007. 65

[113] N. Doi, H. Takashima, M. Kinjo, K. Sakata, Y. Kawahashi, Y. Oishi, R. Oyama, E. Miyamoto-Sato, T. Sawasaki, Y. Endo, and H. Yanagawa1, "Novel Fluorescence Labeling and High-Throughput Assay Technologies for In Vitro Analysis of Protein Interactions," *Journal of Genome Research*, vol. 12, no. 3, pp. 487–492, March 2002. 65

[114] M. Nagel and H. Kurz, "Corrugated waveguide based genomic biochip for marker-free THz read-out," *Int. J. Infrared Millim. Waves*, vol. 27, no. 4, pp. 517–529, April 2006. xiii, 66, 71, 72, 73

[115] T. Baras, T. Kleine-Ostmann, and M. Koch, "On-chip THz detection of biomaterials: A numerical study," *Journal of Biological Physics*, vol. 29, no. 2-3, pp. 187–194, June 2003. 66

[116] E. Kato, H. Yoshida, S. Hayashi, Y. Ogawa, and K. Kawase, "Thz sensing method based on thin metallic mesh and an application for biomolecular sensing," in *the Joint 31st International Conference on Infrared and Millimeter Waves and 14th International Conference on Terahertz Electronics*. IEEE, September 2006, p. 185. 66

[117] R. Parthasarathy, T. Globus, T. Khromova, N. Swami, and D. Woolard, "Dielectric properties of biological molecules in the terahertz gap," *Appl. Phys. Lett.*, vol. 87, 113901, September 2005. 66, 69

[118] C. Wood, J. Cunnungham, C. K. Tiang, M. Byrne, I. C. Hunter, E. H. Linfield, and A. G. Davies, "Measurement and simulation of the sensitivity of terahertz frequency range passive filter elements to overlaid dielectrics," in *the Joint 31st International Conference on Infrared and Millimeter Waves and 14th International Conference on Terahertz Electronics*. IEEE, September 2006, p. 423.

[119] M. Onuma, T. Ohkubo, J. Kitagawa, and Y. Kadoya, "Thz spectroscopic performance comparison between micro-strip-line based sensing methods and attenuated total reflection," in *the Joint 31st International Conference on Infrared and Millimeter Waves and 14th International Conference on Terahertz Electronics*. IEEE, 2006, p. 466.

[120] M. Neshat, D. Saeedkia, R. Sabry, and S. Safavi-Naeini, "An integrated continuous-wave terahertz biosensor," in *Proc. of SPIE*, vol. 6549, May 2007. 66

[121] P. H. Bolívar, M. Nagel, F. Richter, M. Brucherseifer, H. Kurz, A. Bosserhoff, and R. Büttner, "Label-free THz sensing of genetic sequences: towards 'THz biochips'," *Phil. Trans. R. Soc. A*, vol. 362, pp. 323–335, December 2003. 68

[122] G. Ramsay, "DNA chips: State-of-the art," *Nature Biotechnology*, vol. 16, pp. 40–44, January 1998. 68

[123] M. Neshat, D. Saeedkia, and S. Safavi-Naeini, "A THz transducer for on-chip label-free DNA sensing," in *Proc. of OSA Optical Terahertz Science and Technology Topical Meeting*, March 2007. 69

[124] Y. H. Suh and K. Chang, "Coplanar stripline resonators modeling and applications to filters," *IEEE Trans. Microwave Theory Tech.*, vol. 50, no. 5, pp. 1289–1296, May 2002. 69

[125] C. Hornick and G. Weill, "Eleclrooptical study of the electric polarizability of rodlike fragments of DNA," *Biopolymers*, vol. 10, no. 11, pp. 2345–2358, April 1971. 74

[126] G. Hartwich, D. J. Caruana, T. de Lumley-Woodyear, Y. Wu, C. N. Campbell, and A. Heller, "Electrochemical study of electron transport through thin DNA films," *J. Am. Chem. Soc.*, vol. 121, no. 46, pp. 10 803–10 812, November 1991. 74

[127] C. Wittmann, Ed., *Immobilisation of DNA on chips*. Springer-Verlag, 2005. 75

[128] D. Cros and P. Guillon, "Whispering gallery dielectric resonator modes for w-band devices," *IEEE Trans. Microwave Theory Tech.*, vol. 38, no. 11, pp. 1667–1674, November 1990. 82

[129] D. Kajfez and P. Guillon, Eds., *Dielectric Resonators*, 2nd ed. Nobel Publishing Corporation, 1998. 82

[130] H. Peng, "Study of whispering gallery modes in double disk sapphire resonators," *IEEE Trans. Microwave Theory Tech.*, vol. 44, no. 6, pp. 848–853, June 1996. 82

[131] G. Annino, M. Cassettari, I. Longo, and M. Martinelli, "Analysis of 'stacked' whispering gallery dielectric resonators for submillimeter ESR spectroscopy," *Chemical Physics Letters*, vol. 281, pp. 306–311, December 1997. 82

[132] T. Itoh and R.S. Rudokas, "New method for computing the resonant frequencies of dielectric resonators," *IEEE Trans. Microwave Theory Tech.*, vol. 25, no. 1, pp. 52–54, January 1977. 83

[133] E. A. J. Marcatili, "Dielectric rectangular waveguide and directional coupler for integrated optics," *Bell Syst. Tech. J.*, vol. 48, pp. 2071–2102, 1969. 83

[134] S. K. Koul, *Millimeter Wave and Optical Dielectric Integrated Guides and Circuits*. John Wiley and Sons, 1997. 84, 86

[135] H. Auda and D. Kajfez, *Dielectric Resonators*, 2nd ed. Noble Publishing Corporation, 1998, ch. Dielectric Rod Waveguides, pp. 65–111. 84

[136] J. F. Lee, G. M. Wilkins, and Raj Mittra, "Finite-Element Analysis of Axisymmetric Cavity Resonator Using a Hybrid Edge Element Technique," *IEEE Trans. Microwave Theory Tech.*, vol. 41, no. 11, pp. 1981–1987, November 1993. 85

[137] S. Qi, K. Wu, and Z. Ou, "Hybrid integrated HEMT oscillator with a multiplering nonradiative dielectric (NRD) resonator feedback circuit," *IEEE Trans. Microwave Theory Tech.*, vol. 46, no. 10, pp. 1552–1558, October 1998. 85

[138] C. Yeh and F. I. Shimabukuro, *The Essence of Dielectric Waveguides*. Springer, 2008. 86, 87, 121

[139] B. E. Little, J.-P. Laine, and H. A. Haus, "Analytic theory of coupling from tapered fibers and half-blocks into microsphere resonators," *Journal of Lightwave Technology*, vol. 17, no. 4, pp. 704–715, April 1999. 88, 89, 91

[140] M. E. Tobar, E. N. Ivanov, P. Blondy, D. Cros, and P. Guillon, "High-Q Whispering Gallery Traveling Wave Resonators for Oscillator Frequency Stabilization," *IEEE Trans. on Ultrasonic, Ferroelectric and Frequency Control*, vol. 47, no. 2, pp. 421–426, March 2000. 90

[141] D. R. Rowland and J. D. Love, "Evanescent wave coupling of whispering gallery modes of a dielectric cylinder," *IEE Proceedings Optoelectronics*, vol. 140, no. 3, pp. 177–188, June 1993. 90

[142] A. Yariv, "Universal relations for coupling of optical power between microresonators and dielectric waveguides," *Electronics Letters*, vol. 36, no. 4, pp. 321–322, February 2000. 91

[143] M. Neshat, D. Saeedkia, S. Gigoyan, and S. Safavi-Naeini, "Mode-selective dielectric resonator coupled to dielectric image waveguide for sensing applications," in *The Joint* 32^{nd} *Int. Conference on Infrared and Millimeter Waves and* 15^{th} *Int. Conference on Terahertz Electronics*, September 2007, pp. 764–765. 93

[144] E. Krioukov, D. Klunder, A. Driessen, J. Greve, and C. Otto, "Sensor based on an integrated optical microcavity," *Opt. Lett.*, vol. 27, no. 7, pp. 512–514, April 2002. 96

[145] G. Annino, M. Cassettari, and M. Martinelli1, "Study on Planar Whispering Gallery Dielectric Resonators: I. General Properties," *International Journal of Infrared and Millimeter Waves*, vol. 23, no. 4, pp. 597–615, April 2002. 98, 100

[146] M. Neshat, H. Chen, S. Gigoyan, D. Saeedkia, and S. Safavi-Naeini, "Whispering-gallery-mode resonance sensor for dielectric sensing of drug tablets," *Meas. Sci. Technol.*, vol. 21, 015202, no. 1, November 2009. 102

[147] J. T. Carstensen, "Effect of Moisture on the Stability of Solid Dosage Forms," *Drug Dev. Ind. Pharm.*, vol. 14, no. 14, pp. 1927–1969, September 1988. 102

[148] S. C. Gad, Ed., *Pharmaceutical Manufacturing Handbook: Production and Processes.* John Wiley and Sons, 2008. 103

[149] V. D. Viktorov, V. K. Zuev, G. S. Orlov, Yu. A. Poddubnyi, N. A. Filipin, and F. S. Khunafin, "Instrument for automatic observation of metallic inclusions in medicinal preparations," *Pharmaceut. Chem. J.*, vol. 8, no. 7, pp. 447–451, July 1974. 105

[150] B. Saleh and M. Teich, *Fundamentals of Photonics*, 2nd ed. John Wiley and Sons, 2007. 116